Ion Beam Surface Nanostructuring of Metallic Thin Films on Dielectric Substrate and Their Optical Properties

Dissertation Submitted to Hokkaido University for Doctoral Degree in Engineering

By

MENG Xuan

Division of Quantum Science and Engineering,

Graduate School of Engineering,

Hokkaido University

August 2013

Abstract

Noble metal nanoparticles strongly adhered on the dielectric matrices have been extensively studied because of their pronounced applications in optical devices based on tunable localized surface plasmon resonance (LSPR) absorption band. To develop optical devices by using LSPR, it is important to establish a method to disperse noble metal nanoparticles homogeneously on dielectric substrates and to tune the wavelength of LSPR. Compared with chemical synthesis methods, the noble metal nanoparticles formed by ion irradiation on the dielectric substrate draw significant interest in recent years because of the distinct optical properties due to homogeneous single layer dispersion of noble metal nanoparticles and no interlayer deposition on dielectric substrates. However, the detailed investigation of noble metal nanoparticles' microstructure in the dielectric substrate and their relationship with the optical property have been rarely conducted. Therefore, a detailed investigation of ion irradiation induced surface nanostructuring of gold thin films on amorphous SiO_2 substrate is conducted by scanning electron microscopy (SEM) and transmission electron microscopy (TEM). In addition, the dependence of optical property on surface microstructure was studied. Also, 100 keV Ar^+-ion irradiation of Ag-Au bimetallic films on amorphous SiO_2 and single crystal Al_2O_3 have been conducted, in order to investigate the dependence of optical property tuning behavior on the gold concentration and also on substrate structure.

The main objectives of this research are highlighted in chapter 1; (a) to investigate the nanoparticles microstructure dependence on ion irradiation parameters; and (b) to investigate the optical properties dependence on the nanoparticles morphology. Chapter 2 gives a description of experimental procedures. The specimen preparation, ion irradiation condition, and the characterization methods including spectrophotometry, atomic force microscopy (AFM), SEM and TEM are described.

In chapter 3, ion-beam induced suface nanostructuring and the burrowing of the nanostructures by the Ar^+-ion irradiation are described. 100 keV Ar^+-ions were irradiated to SiO_2 substrate with 30 nm gold film on the surface with various fluences. The surface morphologies were investigated by AFM and SEM. Dewetting of Au thin films due to radiation-enhanced diffusion were observed. At the same time, the burrowing of the nanostructures into dielectric matrix was observed. The burrowing of these nanostructures was verified by cross sectional microstructure observation by TEM. Finally, a single layer of spherical Au nanoparticles which formed a single layer structure deeply embedded in the SiO_2 substrate was obtained. The LSPR absorption band due to the localized surface plasmon excitation of these Au nanoparticles was also confirmed by photo absorption spectra. In addition, the dependence of the optical response on ion beam energy was studied and a shift of the LSPR absorption band towards the longer wavelength (red shift) with the increase of ion beam energy was obtained.

In chapter 4, the control of various parameters sensitive to the LSPR absorption band (including particle size and shape) by irradiation fluence was described. Experimentally, 100 keV Ar^{+}-ion irradiation of 30 nm $Au_{(50\%)}$-$Ag_{(50\%)}$ films deposited on the SiO_2 glass substrate was conducted. By increasing the irradiation fluence, the mean size of the nanospheroids decreased, the aspect ratio approached unity and the satellite nanoparticles were formed. It resulted in a shift of the LSPR absorption band towards the shorter wavelength up to an irradiation fluence of 1.0×10^{17} cm^{-2}. The peak was then shifted towards longer wavelength because of the multi-sphere scattering effects due to the satellite nanoclusters. Further control of LSPR absorption band over a wider range has been achieved by synthesizing bimetallic nanoparticles fabricated in the form of alloys of two metals. Experimentally, 100 keV Ar^{+}-ion irradiation of 30 nm pure silver, pure gold, and three different bimetallic Ag-Au films on SiO_2 glass substrate have been conducted, and a single layer photosensitive Ag-Au bimetallic nanoparticles embedded in a SiO_2 substrate was obtained. A remarkable LSPR peaks shifted towards the longer wavelength with the increase of the Au concentration was obtained. Gans theory has been used to model the optical response of these metallic nanoparticles embedded in SiO_2 substrates. This theory accounts for the main effects associated with the major behaviors of the localized surface plasmon excitation.

In chapter 5, substrate dependence was investigated by use single crystal Al_2O_3 substrate. The process of ion irradiation induced surface nanostructuring of 30nm Au-Ag bimetallic films on single crystal Al_2O_3 substrate was different from that on the amorphous SiO_2 substrates due to the substrate structure difference. In case of single crystal Al_2O_3 substrate, higher fluence of 3.8×10^{16} cm^{-2} (in this study) was required to make the near surface amorphous. Therefore, ion irradiation can sufficiently increase the ion-induced viscous flow to burrow Au-Ag bimetallic nanoparticles into single crystal Al_2O_3 substrate. This further supported the present mechanism for the ion induced burrowing of rigid nanoparticles into viscous media. In addition, dependence of the LSPR absorption band on the chemical concentration for the Au-Ag bimetallic nanostructures was also observed; however, the tendency is diverted away from the tendency on the amorphous SiO_2 substrate.

Chapter 6 summarized the conclusions of all these studies. Based on the aforementioned results, ion irradiation is an effective approach in surface nanostructuring and in controlling the LSPR properties of the metallic films on dielectric substrates.

Abbreviations:

UV: ultraviolet;
AFM: atomic force microscope;
TEM: transmission electron microscope;
SEM: scanning electron microscope;
EDS: energy–dispersive spectrometry;
LSPR: localized surface plasmon resonance;
FCC: face–centered cubic;
SERS: Surface enhanced Roman spectroscopy;
TERS: Tip–enhanced Roman spectroscopy;
QSA: Quasi–static approximation;
ADDL: amyloid-beta-derived diffusible ligand;
SUS: stainless steel;
SADP: selected area diffraction pattern;
LFIEF: Local Field Intensity Enhancement Factor.

1 Introduction

1.1 The Importance of Localized Surface Plasmon Excitation

Physical and chemical properties of low–dimensional solid–state systems have attracted considerable attention because of their technological significance. A striking feature of modern technology is the important role of the surface and near-surface regions of materials [1, 2]. Modern communications, complex data storage, electronic thin-film displays, biochips are products of innovative research employing surfaces and thin films in new and creative ways [3–6]. In the past decade, metallic nanoparticles either sustained on the surfaces or dispersed in dielectric matrices have been extensively studied experimentally as well as theoretically because of their pronounced optical and electrical properties (Fig. 1.1). The best–known optical property of metal nanoparticles embedded in glass is the localized surface–plasmon resonance (LSPR), and the formal explanation of this remarkable phenomenon was given by Gustav Mie [4, 7].

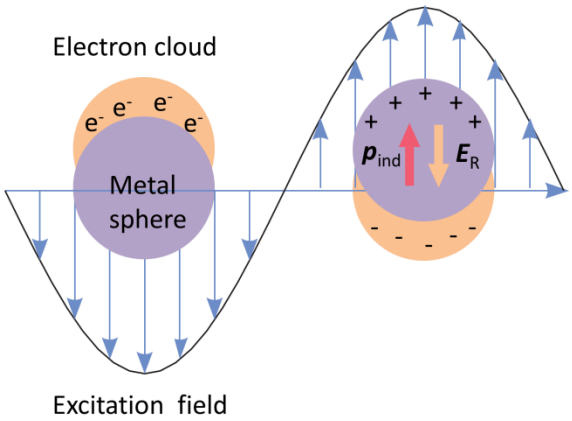

Fig. 1.1: Sketch of homogeneous metallic spheres placed in an oscillating EM field. The conduction electrons are displaced as a whole, polarizing the sphere ($\boldsymbol{p}_{ind}$), while the surface of the particles

exerts a restoring force $\boldsymbol{E}_R$, so that resonance conditions can be established, leading to EM field amplification inside and in proximity of the particle.

Metallic nanostructures with sub-micrometer dimensions exhibit very different optical responses with respect to their bulk counterparts [7]. An external EM field can penetrate inside the volume of the particles, shifting the free electrons gas with respect to the ions lattice; consequently, charges of opposite sign accumulate on the opposite surfaces of the particles, polarizing the metal and establishing restoring local fields ($\boldsymbol{E}_\mathrm{R}$ in Fig. 1.1). Therefore, in formal analogy with the Lorentz model, the particles can be viewed as oscillators, whose behaviour is determined by the free electrons effective mass, charge and density, but most importantly by the geometry of the particles. Under resonance conditions, the free electrons gas is coherently dragged by the external excitation, so the electric dipoles induced inside each particle become extremely large. Correspondingly, the local fields in proximity of the particles are order of magnitudes enhanced with respect to the incident fields, the scattering cross section is enormously amplified, and very strong absorption peaks are observed. Such collective excitations are commonly known as localized surface plasmons (LSPs); for common metals they are usually observed in the visible range (Cu, Ag and Au [8–10]).

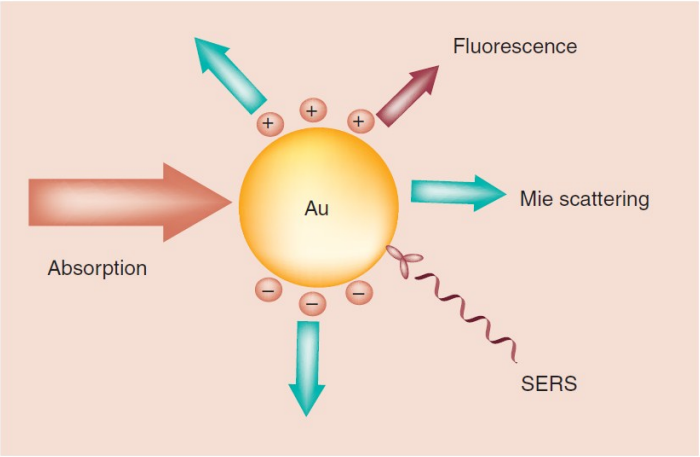

Fig. 1.2: Important optical processes resulting from the interaction of light with a gold nanoparticle, viz. light absorption, Mie scattering, surface–enhanced luminescence and surface–enhanced Raman scattering from absorbed molecules. (Adapted from Ref. [14])

Noble metallic nanoparticles have been extensively studied both experimentally and theoretically because of their appreciable applications in plasmonics (Fig. 1.2). There are many interests in synthesizing silica glass based metal–silica nanocomposites for their considerable applications in nano–optical devices, which have been widely used in ultra–fast optical nonlinear device [5], plasmonic applications in surface enhanced Raman spectroscopy (SERS) and recent development in tip enhanced Raman spectroscopy (TERS) [11–13], LSPR–based biosensor and biomedicine [14, 15], LSPR-based chemical sensors such as molecular, gas, and pH sensors [16, 17], catalysis [1, 2], solar energy utilization [6], and so on.

1.2 Localized Surface Plasmon Excitation Based Applications

1.2.1 Surface enhanced raman scattering

A Raman scattering event in a molecule is an instantaneous optical scattering process in which an incoming photon from the laser at ω_L excites a molecular vibration (with frequency ω_v) while emitting a scattered photon at $\omega_S = (\omega_L - \omega_v)$. The incident photon does not need to be absorbed and induce electronic transitions in the molecule, and it can be considered as an interaction with a 'virtual state' as depicted in Figure 1.3. The scattering is instantaneous for both photons and they are directly connected through the scattering process.

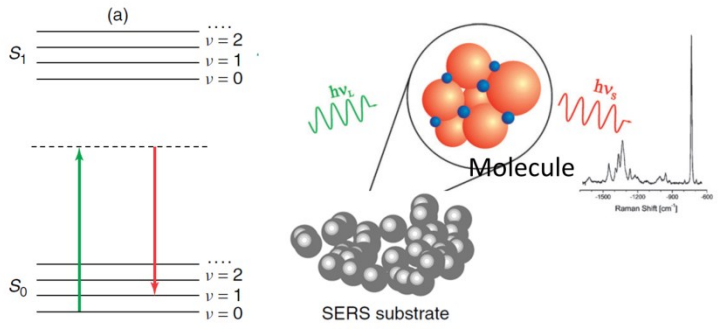

Fig. 1.3 A Raman scattering process is an instantaneous process in which the scattered photon is directly linked to the incoming one. Both photons are simultaneous and benefit from the enhancement provided by the SERS substrate. (Adapted from Ref. [11])

Local Field Enhancements

A important aspect of metallic nanoparticle is the *Local Field Intensity Enhancement Factor* ($LFIEF$) at their surface (i.e. by how much the intensity of the electromagnetic field is changed with respect to the intensity we would have had at the place without the metal). The local field intensity at a specific point is proportional to the square of the

electric field amplitude at that point: $|E(r)|^2$. The $LFIEF$ at a specific point is then the normalized value of $|E(r)|^2$ with respect to the intensity of the incoming field at that point: $|E_0(r)|^2$. Explicitly,

$$LFIEF(r) = \frac{|E(r)|^2}{|E_0(r)|^2}, \tag{1.1}$$

The $LFIEF$ expresses the change in local intensity at a specific point produced by the presence of nanoparticles. Any optical technique that depends on the intensity of the light at a specific point will hence be linked to the $LFIEF$ and depending on whether the optical process involved will be enhanced or quenched ($LFIEF$ is >1 or <1).

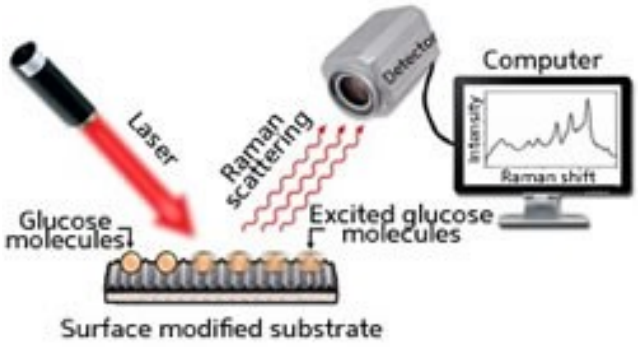

Fig. 1.4 Schematic illustration of surface enhanced Raman spectroscopy. (Adapted from Ref. [12])

The $|E|^4$ Factors Approximation to SERS Enhancement Factors

If we have an isolated molecule in which Raman processes are occurring, and we are detecting that as a Raman signal in the far field, and if we put the molecule in an environment where the laser field is enhanced by a certain amount through an $LFIEF$. We will produce more Raman processes since an increase in the $LFIEF$ at ω_L is equivalent to increasing the laser power. We will therefore observe more scattered photons at ω_S. On the other hand, if we put the molecule in a place that enhances the

emitted field at ω_S (Figure 1.3). This will increase the Raman intensity too.

Hence, the Raman process benefits from both the emission and excitation enhancements, that is, the $LFIEF$ at both ω_L and ω_S, and this leads to an EF for SERS of the form.

$$EF = LFIEF(\omega_L) \times LFIEF(\omega_S) \tag{1.2}$$

The difference between the $LFIEF$ at ω_L and that at ω_S can sometimes be ignored in many cases. This is due to the fact that $\omega_L - \omega_S$ (Raman shift) is sometimes small compared to the typical frequency ranges where the $LFIEF$ shows substantial changes. Taking into account that the $LFIEF$ at a given point is given by Equation (1.2), the SERS *EF* at r with all the above approximations included reads

$$\mathrm{EF} \sim LEIEF^2(\omega_L) = \frac{|E(r)|^4}{|E_0(r)|^4}, \tag{1.3}$$

This is the so-called $|E|^4$ approximation for the SERS enhancement. Despite its many approximations and simplifications, it provides a very useful estimate for the actual experimental SERS enhancements in a single molecule located at r. A schematic illustration of a typical surface enhanced Raman spectroscopy is show in Figure 1.4.

Tip-Enhanced Raman Scattering (TERS)

A major breakthrough in SERS in the last few years has been the introduction of the related technique tip-enhanced Raman scattering (TERS) [11, 13]. Coupled plasmon resonances are not limited to gaps between objects with the same geometries, but rather exist for any pair of metallic interacting objects. An important case of coupled plasmon resonances happens between a flat metallic surface and a tip, as displayed schematically in Fig. 1.5, under which configuration a tip-enhanced Raman scattering works. If we set

the external field direction along the axis of the tip, in which case the plasmon resonance resulting from the interaction between the surface and the tip couples most efficiently. Figure 1.5 shows a $LFIEF$ map at 620 nm where the clear presence of a hot spot in between the tip and the surface can be seen. This is the position that a deposited molecule on the substrate would be occupying under the tip.

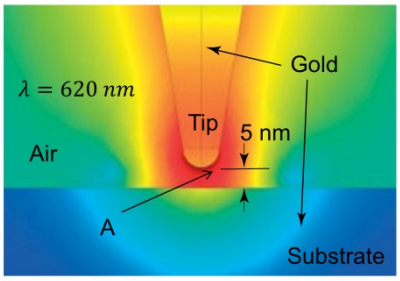

Fig. 1.5 A typical TERS geometry: a flat substrate and a tip (both made of gold in this case) are brought together with a gap of a few nanometers in between. (Adopted from Ref. [11]).

1.2.2 Surface plasmon resonance based colour filter

Daisuke Inoue *et. al.* [18] have demonstrated an aluminum red-green-blue (RGB) color filter. The RGB color filters made from Al films containing various arrays of shaped sub-wavelength holes, created using electron beam lithography.

Figure 1.6 shows optical microscope images of various shapes of holes in Al films. The color bars are due to hole arrays with different periods and shapes. The numbers beside the photographs give the periods of the hole arrays corresponding to the color bars. The side-lengths of the squares and triangles, and the diameters of the circle are half as large as the period. The microscope images at the top are the corresponding SEM images.

Figure 1.7 shows an optical microscope image of an Al color filter. This filter has equilateral triangular shaped holes, periodically arranged on an Al film. The side lengths of the holes are 210 nm, 170 nm and 150 nm, and the lattice constants are 420 nm, 340 nm and 300 nm, for the red, green, and blue colors, respectively.

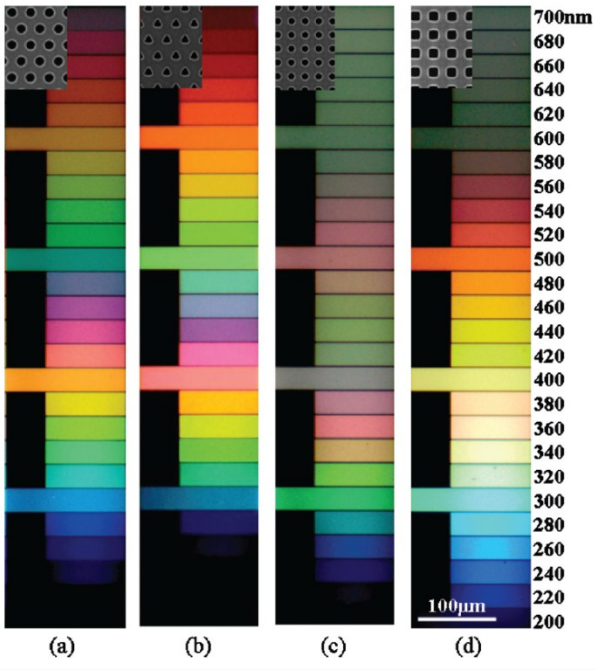

Fig. 1.6 Optical microscope images of aluminum color filters with (a) circular holes arranged on a hexagonal lattice, (b) triangular shaped holes, (c) circular holes arranged on a square lattice, and (d) square holes. The numbers beside the photographs give the period of the arrays in nanometer. (Adapted from Ref. [18])

Fig. 1.7 Optical microscope image of aluminum color filter with triangular shaped holes. (Adapted from Ref. [18])

1.2.3 Localized surface plasmon resonance based bio-sensing

Metal nanoparticles LSPR absorption found large applications for chemical and biological sensing, due to sensitive spectral response to local surface environment and ease of monitoring the light signal due to the strong light scattering and absorption [8, 9, 14]. Even the slightest change in the dielectric surrounding leads to a detectable shift of the resonance energy. That is the reason why metallic nanoparticles are very suitable for sensing applications. The spectral sensitivity, defined as the relatice shift in resonance wavelength with respect to the refractive index change of surrounding materials, is dependent on the SPR absorption position and width, which in turn depend on metal type and on particle shape. As decribed in the previous sections, silver is more sensible than gold to surface environment and nanorods are better than spheres in reason of a plasmon absorption band more sharp and intense.

Localized Surface Plasmon Resonance Wavelength-Shift Sensing

The most common method for LSPR sensing is the wavelength–shift measurement, in which the change in the maximum of the LSPR extinction curve is monitored as a function of changes in the local dielectric environment caused by analyte adsorption. This relationship is described in Eq. 1.4 [14], and has been demonstrated for a number of systems in which either the bulk-solvent refractive index or the length of a molecular adsorbate (i.e., a linear alkane chain) is changed.

$$\Delta\lambda_{\max} = m\Delta n\left[1 - exp\left(\frac{-2d}{l_d}\right)\right], \tag{1.4}$$

here m is the bulk refractive–index of the nanoparticles; Δn is the change in refractive-index of the adsorbate; is d the effective adsorbate layer thickness; and l_d

is the characteristic EM–field–decay length.

This sensitivity to local environment can be expanded to sensing biological molecules such as proteins and antibodies [15, 16]. Initial demonstrations of this principle measured the shift in λ_{max} on binding of either streptavidin or antibiotin to biotinfunctionalized nanoparticle arrays (Fig. 1.8). Perhaps the most biomedically relevant demonstration of LSPR sensing has been the work in which a biomarker for Alzheimer's disease, amyloid–beta–derived diffusible ligand (ADDL), has been sensed using LSPR spectroscopy [15].

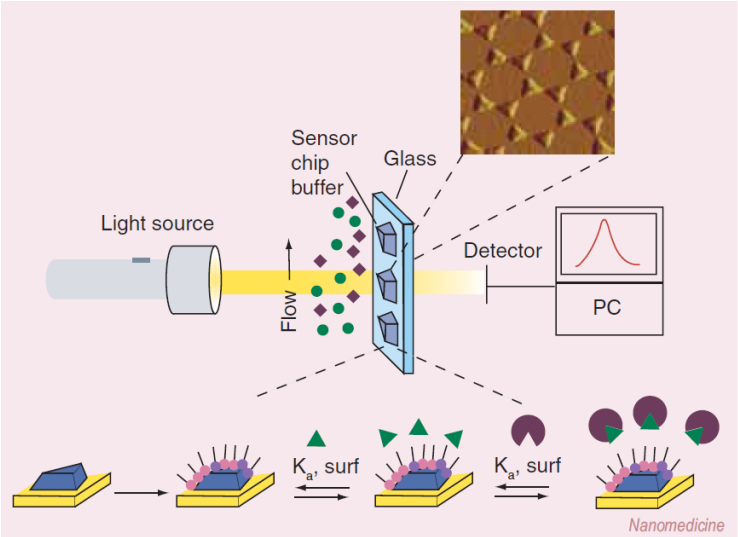

Fig. 1.8 Representive experimental set-up and procedure for localized surface plasmon resonance (LSPR) sensing. Transmission UV-visible spectroscopy is used to monitor the optical absorption of Ag nanoparticles. (Adapted from Ref. [14])

1.3 Overview of the Various Methods for Surface Nanostructuring

There have been impressive developments in the field of nanotechnology in recent years, with chemical and lithographical methodologies being developed to synthesize NPs of particular size and shape. Purely chemical synthetic routes like innovative colloidal self–assembly [19–22], lithography methods like nanosphere lithography [23, 24], laser irradiation [25], electron irradiation [26], and ion irradiation [36–38] have been developed for manufacturing high efficiency platforms for the LSPR–based sensors.

1.3.1 Colloid chemical methods.

Nowadays, colloidal chemistry can produce a myriad of metal NPs in solutions with a variety of morphologies from sphere to complex core–shell, with very good control of the size distribution [19–22]; this control over the size, composition, and morphology of the NPs in a system can produce dramatically different absorption features in the visible or near–infrared spectrum (Fig. 1.9) [19]. However, the synthesis of these structures, in particular within a matrix, is a significant challenge.

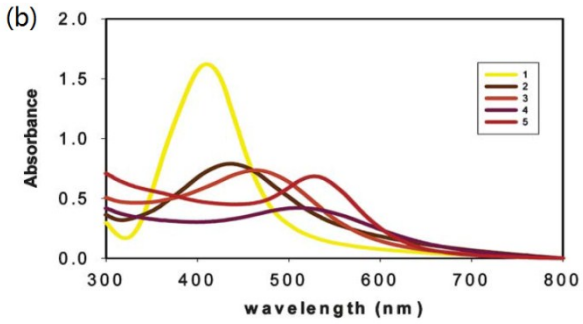

Fig. 1.9 (a) Photograph of the aqueous dispersions of starch stabilized Au, Ag and the various Au-Ag alloy compositons. The Au-Ag mole ratios are: (1) 0.0:1.0; (2) 0.25:0.75; (3) 0.5:0.5; (4) 0.75:0.25; (5) 1.0:0.0. (b) The corresponding surface-plasmon absorption bands for these five samples. (Adapted from Ref. [19])

The silanized glass coverslips were subsequently immersed in a colloidal gold solution to form a self-assembled monolayer of the gold colloids on both sides of the glass coverslip (Fig. 1.10) [20]. The immobilized colloids were used in the applications of SERS and LSPR based biosensors.

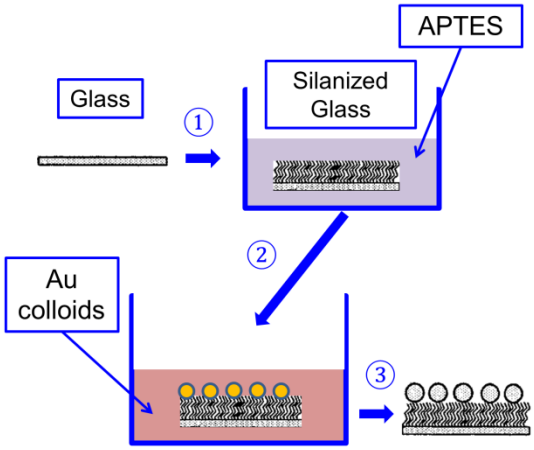

Fig. 1.10 Schematic of the steps involved in the fabrication of the immobilized colloidal gold sensor chip on glass. Glass substrate was functionalized with APTES to provide an amine-terminated surface for formation of a monolayer of gold nanoparticles (AuCM).

1.3.2 Nonosphere lithography

Nanosphere lithography is an inexpensive and simple method to fabricate large arrays of nanoparticles with well controlled size and shape. Nanosphere lithography fabrication begins with the self-assembly of size-monodisperse polystyrene nanospheres to form a deposition mask (Fig. 1.11). Then, metal is deposited through the nanosphere masks using thermal or electron beam evaporation. After the removal of polysryrene nanospheres, well ordered 2D triangular nanoparticle arrays remain on the substrates. By changing the nanosphere diameter and the deposited metal thickness, nanoparticles with different inplane width, out-of-plane height and interparticle spacing can be produced [23, 24].

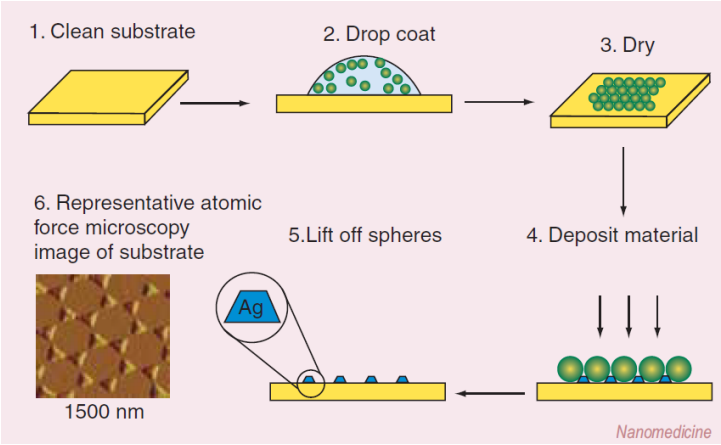

Fig. 1.11 Schematic illustration of Ag nanoparticle fabrication procedure using nanosphere lithography. (Adapted from Ref. [14])

Uauaslly, a Cr adhesion layer is deposited between Ag nanoparticles and a glass substrate, for the purpose of improving the adhesion of Ag nanoparticles to glass, was observed to cause an abnormal peak shift of extinction spectra in nonspecific reactions. Also, the undesired peak shift misleads molecule detection in non-specific reactions.

1.3.3 Quatum beam irradiation

(a) Laser beam irradiation

Cobalt films ranging in thickness from 1 and 8 nm were deposited by e-beam evaporation onto optically smooth SiO_2 surfaces in vacuum [25]. The morphology following double-beam laser irradiation is shown in Figs. 1.12a–c. The typical pattern evolution for films with $h_0 > 2\,nm$ begins with spatially periodic film rupture at length scales equal to the interference spacing at the early stages. Longer irradiation yielded the formation of long, cylindrical-like "nanowires" and continued irradiation resulted in the breakup of these nanowires into particles. The final particle state is characterized as a quasi-2D array, comprised of the longer range order due to periodic laser intensity and the shoter range order resulting from the breakup of the nanowires.

Experimental measurements of the trends in neareast neighber particle spacing λ_{NN2} and the corresponding particle radius $r_{p2}$with film thickness h_0 are shown by open squares in Figs. 1.12 d and e, respectively. Both quantities increased as $h_0^{1/2}$. These results are in contrast with what was observed from single-beam uniform laser irradiation. In Fig. 1.12 d(closed circles), the scaling behavior of the spatial correlation in the final stable nanoparticle state is shown for varying initial film thicknesses. The observed trend with h_0 was in agreement with classical linear TFH dewetting theory.

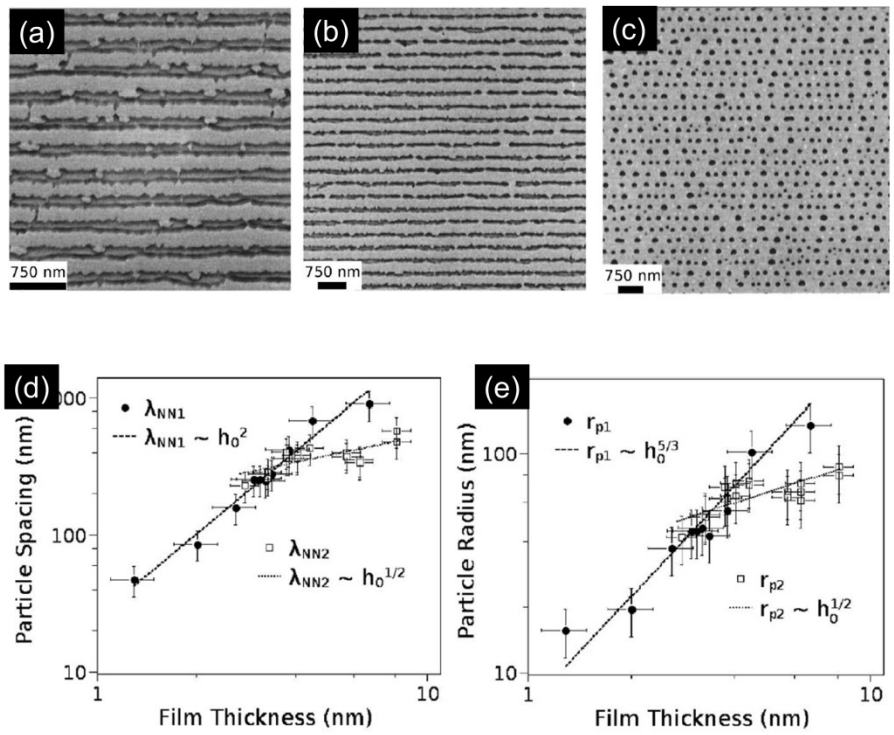

Fig. 1.12: SEM images depicting the stages of pattern formation for double-beam interference irradiation of an ~6 nm film as a function of increasing number of laser pulses n: (a) periodic rupture,(b) nanowires, and (c) final nanoparticle state which exhibits both LRO and SRO. Co rich and SiO_2 rich regions correspond to bright and dark contrasts, respectively. Self-organized length scales vs initial film thickness: (a) $h_0^{1/2}$ dependency for the particle radius from double-beam interference irradiation(open squares) and $h_0^{5/3}$ dependency from single-beam irradiation (closed circle). (b) $h_0^{1/2}$ dependency for the particle spacing from double-beam irradiation (open squares) and h_0^2 dependency from single beam irradiation (closed circle). The dashed lines are trends with the indicated exponents of h_0. (Adapted from Ref. [25])

(b) Electron beam irradiation

Electron-beam-induced nanoparticle formation from thin (5–30 nm) Au film on smooth SiO_2/Si substrates was obtained. Au nanoparticles were formed by dewetting of the melted Au on the SiO_2/Si surface [26]. The generated nanoparticles had positional correlation and a dominant wavelength, which varied linearly with the initial film thickness.

Figure 1.13 shows SEM images of the surface morphologies of Au, which originally existed as thin films of different thicknesses on smooth SiO_2/Si substrates, after irradiation with an electron beam. In this case, the electron-beam diameter was 14.2 μm, the beam current was 82 μA, and the irradiated area was 346 μm × 346 μm. After irradiation with the electron beam, the Au films broke up into nanoparticles. Au nanoparticle formation was obtained for the film thickness of 5–30 nm. Also, the positional correlations and average diameters of the generated nanoparticles were plotted as a function of film thickness (Figure 1.13e and f). It is seen from the figure that the dominant wavelength and also the average diameter vary linearly with the initial film thickness.

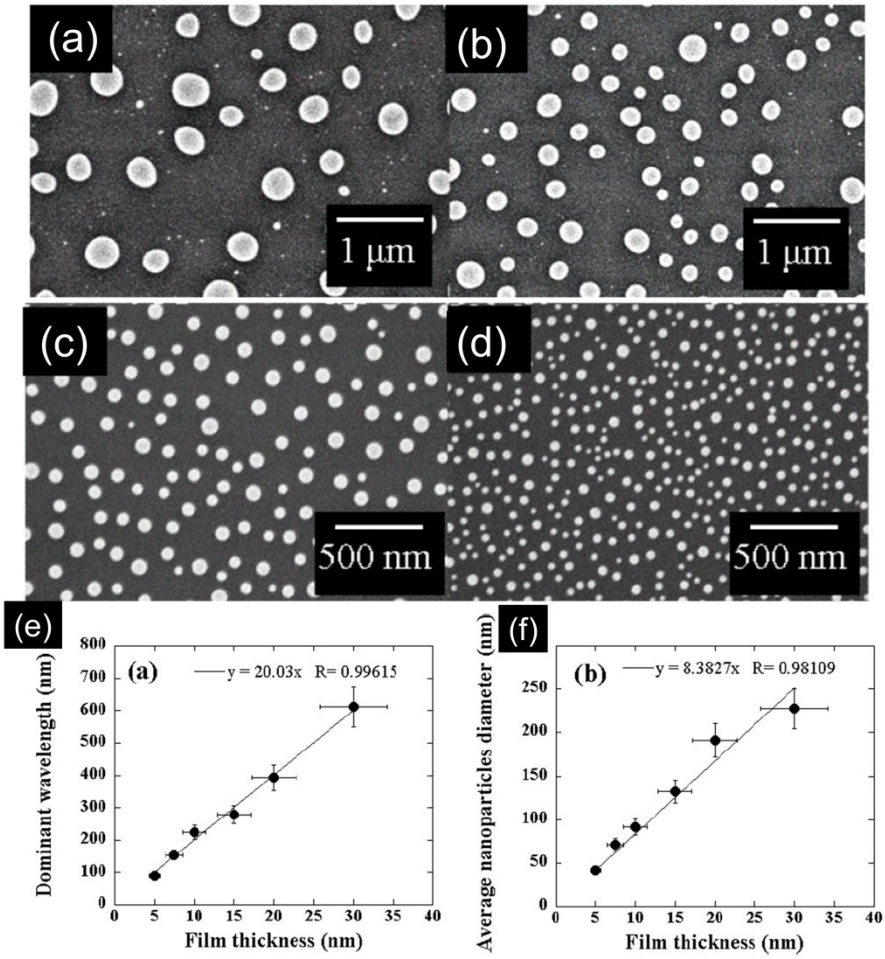

Fig. 1.13 SEM images of Au films with different thicknesses after electron-beam irradiation. The Au films had thicknesses of (a) 30 nm, (b) 20 nm, (c) 7.5 nm, (d) 5 nm. (e) Positional correlation and (f) average diameter of Au nanoparticles as a function of initial film thickness. (Adapted from Ref. [26])

1.4 Overview of the Ion Irradiation Surface Nanostructuring

Ion-beam processing of materials greatly enriches the materials science and provides new opportunities for synthesizing materials with unique microstructures and properties [27, 28]. In the following, we will develop the theoretical framework to understand these materials problems involving irradiation.

In the case of low-dose irradiation, the Ar ions implanted, after stopping and thermalization, are dispersed through out the volume of the dielectrics and are well separated from each other. The energy of the implant is transferred to the matrix via electron shell excitation (ionization) and nuclear collisions. This causes radiation-induced defects, which, in turn, may reversibly or irreversibly modify the material structure. Various types of crystal structure damage have been observed in practice: extended and point defects, cascade collsions, surface crosion, amorphization, precipitation of a new phase made up of host atoms or implanted ions, etc. As show in the Fig. 1.14, there are about 2.4 atoms (including oxygen and silicon atoms) sputtered away for one 100 keV Ar ion bombard the SiO_2 surface. In addition, there are about 1400 vacacies and 1400 interstitials produced along the path in the slow down process for the Ar ion, even though most of the vacancies and interstitials will annihilate afterwards [29]. The blue region illustrates the interstitials and vacancies distribution in the SiO_2 and the red region illustrates the implanted argon ions distribution. As they both had a nonuniform distribution in the substrate, they will diffusion due to the concentration gradient, which will result in the radiation enhanced diffusion and mass transfer. Furthermore, a brief description of the ions slow down process in solid material is introduced in the following:

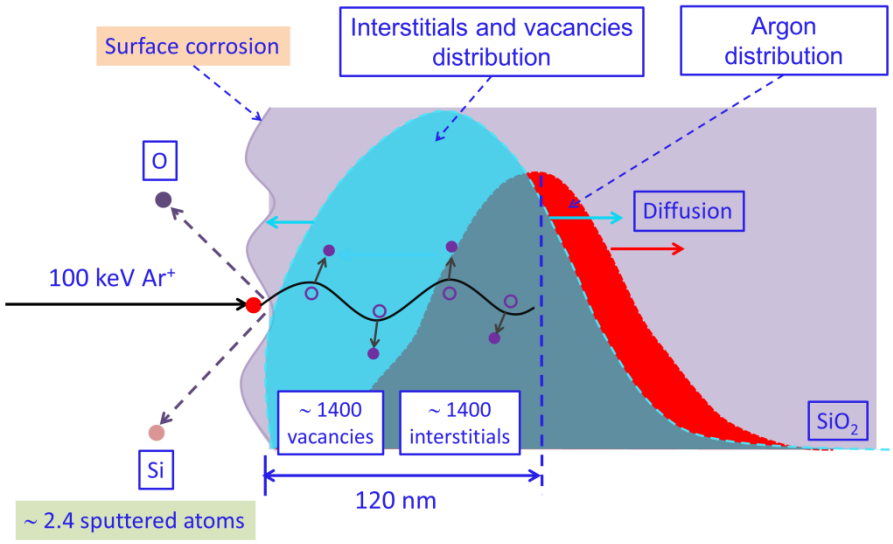

Fig. 1.14 Schematic illustration of a 100 keV Ar ion slow down in SiO_2 substrate.

Electronic Excitation

As an ion impinges on a solid it begins a series of collision with both the electrons and the ion cores of target atoms. The collisions with electrons are more numerous owing to their larger number and cross section, but since their mass is small they do not much alter the trajectory of the incoming ion, nor do they usually result in atomic displacements. In most materials, therefore, these inelastic collisions can be treated simply by assuming that the electrons form a viscous background that extracts energy from the fast–moving ions and slows them down. The energy loss of ions due to these inelastic excitations is characterized by the electronic stopping power $S_e(E)$.

Defect Production

Ions are also slowed down in a solid by the elastic collisions between the projectiles and target atoms; this slowing can also be characterized by a stopping power $S_n(E)$. These collisions, however, can lead to displacement damage, whereby a knocked-on atom

recoils away from its initial lattice site. Typically, an atom must receive ≈25 eV of energy to create a stable interstitial–vacancy (Frenkel) pair. Many recoil atoms receive much higher energies, as discussed below, and these recoils can undergo a series of secondary recoils with target atoms displacing them as well, and indeed, many of these secondary recoil atoms can create yet additional displacements in tertiary recoils, and so on. In this way, a displacement cascade evolves. When the energies of recoil atoms fall below 25 eV, the atoms continue to be displaced from their lattice sites, however, the separation between the interstitial–vacancy pair is too small to avoid spontaneous recombination owing to the strong elastic interaction between the two defects.

Sputtering

In the process of ion irradiation, the incident ions penetrate into target and transfer their kinetic energy to the target atom by creating cascade of collisions among the substrate atoms or through other processes such as electronic excitations. Most of these atoms will come back to their original locations but some of them, especially those atoms located in the first layer or two of the surface that receive recoil energies greater than the sublimation energy (≈5 eV) with momentum directed away from the surface can be sputtered into the vacuum [30]. As a consequence, the surface continually erodes during irradiation. The amount of erosion is measured by the sputtering yield, Y, which is defined as the mean number of atoms removed from the surface of a solid per incident particle:

$$Y = \frac{average\ number\ of\ atoms\ removed}{incident\ particle}, \tag{1.5}$$

For amorphous and polycrystalline targets, Sigmund revealed that the sputtering yield is proportional to the energy accumulated by ions. More importantly, Sigmund proved that sputtering yield is larger for troughs than for crest [30]. Many surface features induced by ion bombardment, including ripple and nanodot formation are based on this theory.

Preferential Sputtering

Generally, the composition of the target, the parameters of the incident ion beam, and experimental geometry contribute to the sputtering yield. It is common that partial sputtering take place in alloys. In general, partial sputtering yields are different, and this leads to surface compositions that differ from the bulk composition. Once sufficient material has been removed and steady state achieved, the alloy compositions are constant in time, albeit inhomogeneous just below the surface. In steady state, the alloy components must sputter at rates proportional to their bulk compositions (not their surface compositions).

Thermal Spikes

The displacement cascade just described evolves in time over a period of a few tens of ps. Beyond this period the atomic energies fall below 5 eV and the collisions can no longer be considered as two-body events, but rather many-bodied. Indeed, as a molecular dynamics simulation of a 10-keV collision event in the ordered B_2 phase of NiAl shows in Fig. 1.15, all of the atoms localized in a small volume are set into motion. Further analysis indicate the local temperature can rise significantly above the melting temperature for several ps, giving rise to liquid-like diffusion and defect clustering on subsequent cooling [31]. Notice in Fig. 1.15 the rather well defined solid–liquid phase

boundary. At the end of the recoil event shown in Fig. 1.15, only 25 Frenkel pairs are created (ξ(10keV) = 0.27) while ≈2000 atoms relocate from their initial lattice sites.

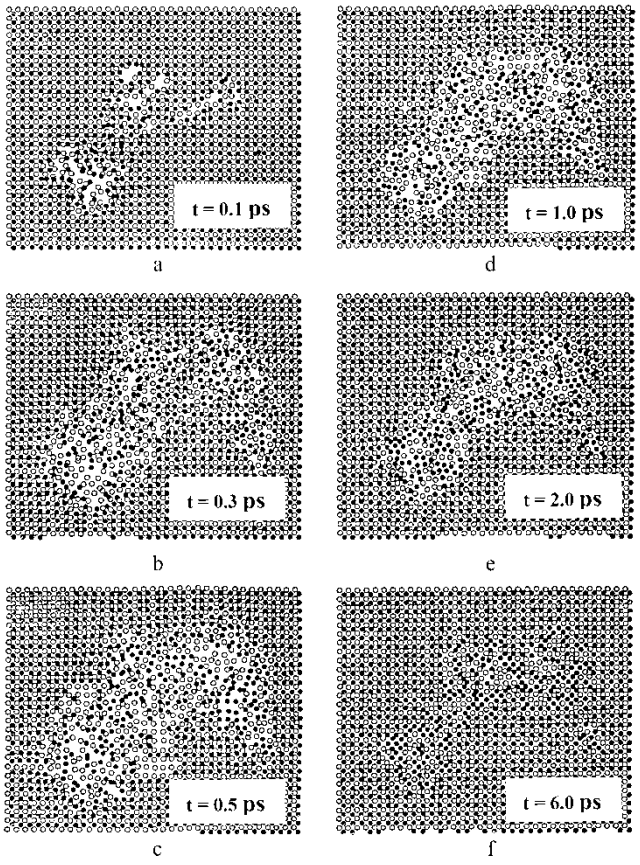

Fig. 1.15 Position of atoms in a cross-sectional slice, one lattice parameter thick, during a 10-keV event in β-NiAl. (Adapted from Ref. [31])

Ion-Beam Mixing

Materials under ion irradiation undergo significant atomic rearrangement and this process effectively introduces surface nanostructuring on the dielectric surface [27]. The most obvious phenomenon is the atomic intermixing that occurs at the interface separating two materials during ion irradiation (schematically shown in Fig. 1.16). As an energetic ion (100 keV Ar^+ ion in this case) penetrates a solid, it slows down by deposition energy both to the atoms and to the electrons of the solid. During the nuclear

collision, target atoms are displaced from their lattice sites. When the high energy collisions occurs near the interface (the interface of Au and SiO_2), the target atoms recoiled forward and resulted in the transport of atoms, which is known as recoil mixing. In addition to recoil mixing, multiple displacements of target atoms resulting from a collision cascade surrounding the ion track happens, producing secondary recoil atom displacements, and this process is commonly referred as cascade mixing. As the irradiation fluence increases, a continuous mixed layer is formed at the interface, as indicated in red circle in Fig. 1. 16. Therefore, ion beam mixing attracts much attention for their ability to produce ion modified materials with higher solute concentrations at lower irradiation fluences than can be achieved with conventional high–fluence implantation techniques.

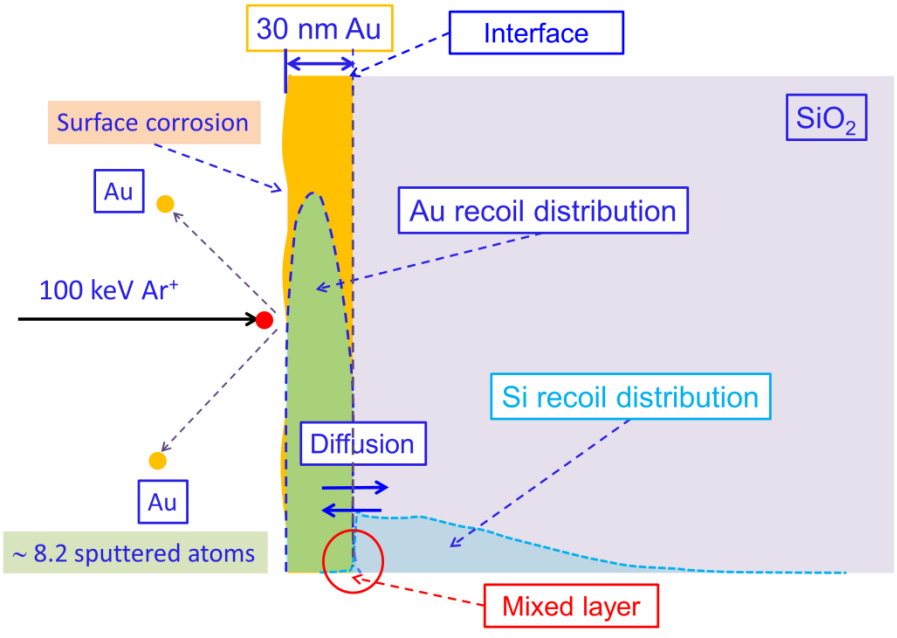

Fig. 1.16 Schematic illustration of ion irradiation induced interface mixing.

Ion Induced Amorphization

Many irradiated materials have been shown to undergo a crystalline to amorphous transition during irradiation at temperatures sufficiently far below the crystallization temperature of the amorphous phase. Covalently bonded systems are particularly conducive to amorphization, with even pure elements Si and Ge undergoing amorphization during irradiation [32]. In the thesis, we concern ourselves only with how this phase transition depends on the conditions of the irradiation, and therefore we will simply assume that the accumulation of defects and disorder eventually leads to amorphization.

Radiation-Enhanced Dffusion

At elevated temperatures the high concentrations of defects produced in the cascade can migrate throughout the material and begin to restore equilibrium. Radiation-enhanced diffusion is typically treated within a mean-field theory approach using chemical rate equations. During irradiation at elevated temperature, the defect concentrations typically reach their steady states long before the phase transformations take place, and spatial variations in the steady-state concentrations often remain small, so that the defect concentrations are easily obtained. Genarally, at low temperature, the migration of defects is negligible and the diffusion is controlled by ion-beam mixing [33, 34]. As the temperature is increased, defect diffusivities increase. The concentration of point defects in this regime is controlled by the production rate and recombination, giving rise to a temperature-dependent diffusion coefficient. At still higher temperatures, the point defects migrate to sinks, rather than recombining. This behavior is very different from that arising from thermal diffusion. The thermodynamic reason for the dewetting of the

metal film is the high interfacial energy and hence the continuous film is unstable on the substrate. Kinetically, the occurrence of this process requires the mass transportation of the metal atoms, indicating that mobility of the metal atoms is significantly enhanced by ion irradiation.

Irradiation-Induced Viscous Flow

Irradiation of materials under an applied stress at elevated temperature can lead to enhanced creep rates and stress relaxation owing to the increased concentrations of point defects. Therefore, unusual plastic deformation has also been observed during irradiation at temperatures where defects are immobile [35].

Figure 1.17 shows snapshots obtained from a MD simulation of 10-keV self-ion bombardment of Au at different instants of time [35]. As the cascade event evolves, the local volume heats above the melting temperature and pressures of ≈1–10 GPa develop in the core. The pressure associated with the thermal expansion and the solid–liquid transformation causes mass to flow onto the surface. With time, the pressure relaxes and a small volume of liquid is left in the surface region. When the liquid cools and resolidifies, however, atomic mobility becomes negligible and many atoms are left frozen on the surface. As a consequence, there is a net flux of mass onto the surface, leaving many vacancies below the surface, which condense into dislocation loops. It is also observed that a mound forms on the surface around each impact, owing to the excess material. In some cases craters are also formed, surrounded by a rim. These features add roughness to an irradiated surface and generally they contribute far more roughness to a film than simple sputtering.

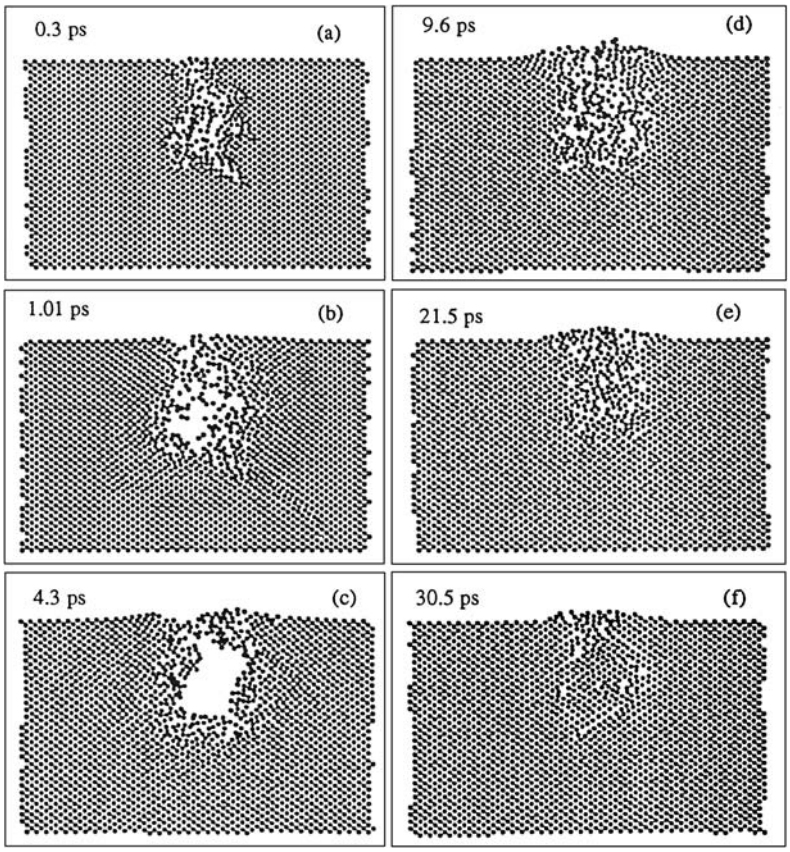

Fig.1.17 Evolution of a 10-keV cascade in Au. This event is initiated by a Au impinging on the surface at 0 K. Atoms located within a cross-sectional slab 0.4 nm thick are shown. (Adapted from Ref. [35])

In conclusion, ion-beam technology provides a unique and exciting way of modifying the near-surface region of a solid; controlling its surface properties, adding beneficial impurities in the near-surface region, modifying the crystallinity, and providing a control and specificity that exceeds almost all other methods of surface modification. In metals and insulators, as well as in the more familiar case of semiconductor physics, new approaches that control atomic displacements, defect creation and evolution often pose interesting physics problems and lead to specific applications. Ion-beam science and engineering have already made extraordinary impacts in current silicon technology for communications, surface hardening for structural improvements and materials modification to create solids with new properties. Over the last decades, ion beams have been increasingly used to synthesize and explore properties of metallic or semiconductor alloys and compounds outside of equilibrium phase diagrams depending on the combination of thermodynamical and ion-beam energy deposition parameters, and the outcome may be either a known or a novel phase, ordering or disordering.

Previous works of ion induced nanostructuring of metallic films on SiO_2 substrate

Ion induced Pt films rupture on SiO_2 substrate have been reported by 800 keV Kr^{++} ion irradiation [36, 37], and they ascribed this rupture behavior to be ion irradiation induced dewetting. In addition, the mechanism of the irradiation induced dewetting was ascribed to be the radiation enhanced diffusion. Figure 1.18 shows the SEM images of 3 nm Pt films on SiO_2 substrates irradiated by 800 keV Kr^{+} at several doses. Pt films dewet from the substrates and form nanoscale patterns at 2×10^{14} cm^{-2}. The patterns coarsen with continuing irradiation up to a dose of 6×10^{15} cm^{-2}. At higher dose, 2×10^{16} cm^{-2}, the patterned structure disappears, leaving Pt nanoparticles with the size of 10−20 nm. The exposed surface fraction of the substrate in each image is plotted as a function of dose in Fig. 1.19a. The lateral correlation lengths of the Pt nanopatterns are obtained by taking the autocorrelation of the images; these are shown in Fig. 1.19b. The increase of exposed surface fraction and lateral correlation length with irradiation dose is evident in these figures, increasing from ~16% and 15 nm at 2×10^{13} cm^{-2} to ~92% and 50 nm at 2×10^{16} cm^{-2}.

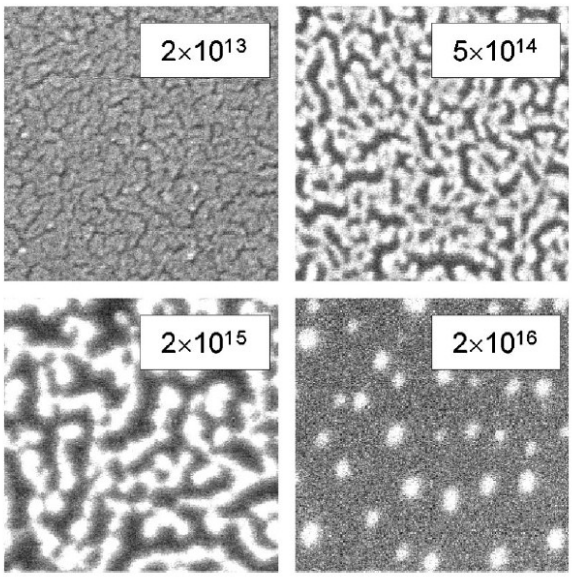

Fig. 1.18 SEM images of 3 nm Pt/SiO_2 irradiated by 800 keV Kr^+ at room temperature. Bright areas correspond to Pt. The doses are shown on the upper right corner of each image in the unit of ions cm^{-2}. The image sizes are all 300×300 nm^2. (Adapted from Ref. [36])

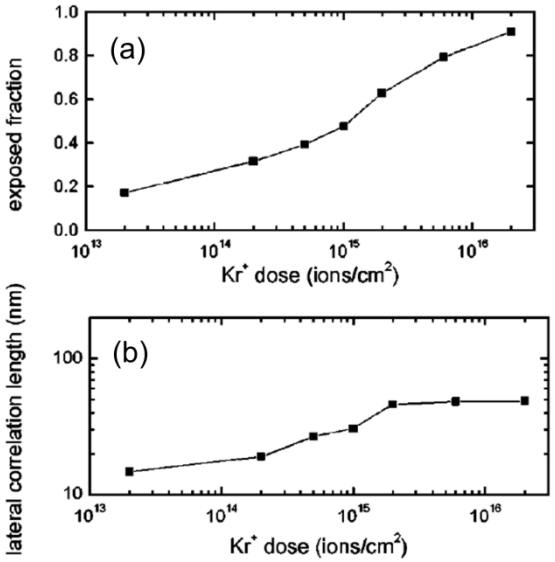

Fig. 1.19 Evolution of exposed surface fraction (a) and lateral correlation length (b) with ion irradiation dose, extracted from SEM images of 3 nm Pt/SiO_2 irradiated by 800 keV Kr^+ at room temperature. (Adapted from Ref. [36])

Using the technique of ion-beam sputtering on gold (Au) metal films, metal nanocluster nanostructure materials are synthesized on silica glass substrates by 100 keV Ar ion irradiation [38]. Optical absorption spectroscopy results reveal the formation of metal nanoclusters on the glass substrates. Red shift of the surface-plasmon resonance position due to the sputtering induced size reduction of Au nanoclusters on the silica substrates has been explained. Size reduction in this case is further corroborated with the scanning electron microscopy results.

Electron scanning microscopy shows the surface morphology of the Au films as a

function of Ar^+ ion doses. A continuous and smooth film of Au initially turned to be a discontinuous film and finally resulted in Au nanoclusters (Fig. 1.20c) with gradual increase of the ion doses. Average cluster size of Au atoms is measured to be around 50 nm in the high dose (7×10^{16} ions/cm^2) irradiated samples. The characteristic optical absorption peak of Au nanoclusters have developed with the increase of ion irradiation doses. The optical response peak around 550 nm is attributed to the surface-plasmon resonance absorption in Au nanoclusters. Interestingly, there is a red shift of resonance peak position with the increase of ion doses in the case of Au samples (Fig. 1.21). The shift in the resonance absorption peak by about 20 nm towards longer wavelength has been observed for the highest dose irradiated samples (1×10^{17} ions/cm^2) with respect to the samples irradiated with 5×10^{16} ions/cm^2. This may be explained as a result of decreasing the average size of Au nanoclusters with the increase of Ar^+ ion irradiation doses.

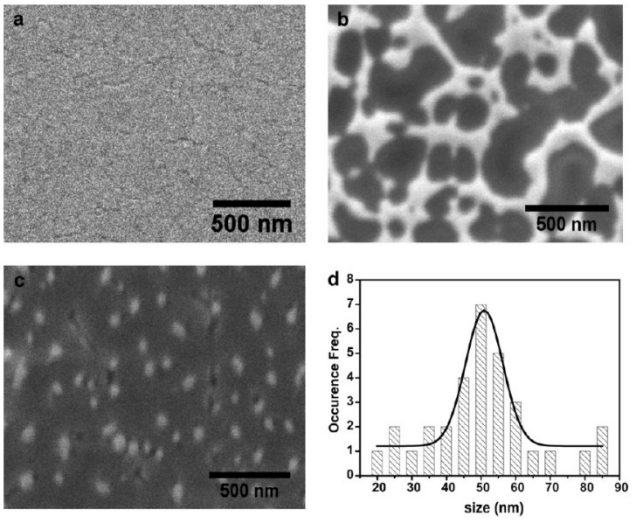

Fig. 1.20 SEM micrographs of (a) as-deposited Au film on silica, Ar^+ irradiated Au films with ion doses (b)1×10^{16}, (c)7×10^{16} ions/cm2, and (d) histogram plot of Au nanoclusters obtained from the image(c). (Adapted from Ref. [38])

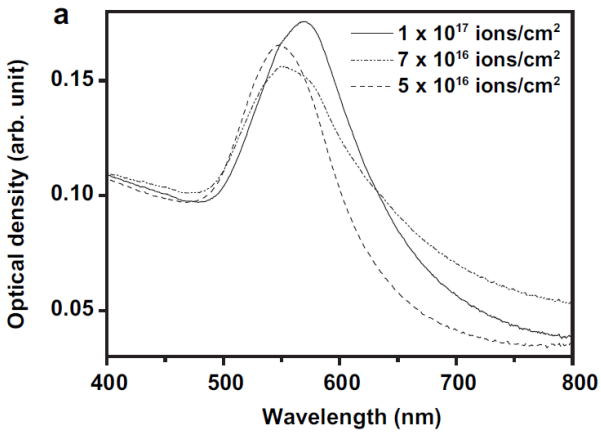

Fig. 1.21 Optical absorption spectra of Au nanoclusters formed during the ion-beam sputtering of metallic films with various Ar^+ ion doses. (Adapted from Ref. [38])

1.5 Objectives of The Thesis

Since the begining of ion beam mixing technique by Tsaur and Mayer in 1981 [39], a variety of experiments have been performed on the surface nanostructuring of metallic films deposited on dielectric substrate [32-38]. The investigation of ion induced sputtering [30], the ion induced dewetting due to radiation enhanced diffusion [33, 34], and ion induced burrowing mechanism was first proposed in 2002 and it is presently considered to be caused by radiation enhanced viscous flow [40-42]. However, the studies of optical properties of these nanostructures fabricated by ion irradiation are still limited. In addition, the behaviors of the surface plamon exication of these nanoparticles on fabrication parameters are still unclear.

P. Gangopadhyay *et. al.* [38] used 100 keV Ar ion irraidation of 40 nm Au thin films deposited on silica glass. Au nanoclusters were synthesized and optical absorption spectroscopy results reveal the localized surface plasmon resonance excitation of metal nanoclusters on the glass substrates. The shift of the surface-plasmon resonance position towards longer wavelength (red shift) is ascribed to be the sputtering induced size reduction of Au nanoclusters on the silica substrates. However, there is a discrepancy between Mie's predictions of the dependence of surface-plasmon resonance position shift on nanoparticles size. Under Mie's prediction, the surface-plasmon resonance position shift towards short wavelength as decrease the nanoparticle [43]. Therefore, I suppose there are some other effects such as nanoclusters shape, chemical component change and also the effect of the substrate will have contributions to the red shift of the the surface-plasmon resonance position. The detailed discussions of these effects on surface-plasmon excitation behavior are given in the following:

(A) Sputtering modifies the nanoclusters shape and size

The most important effect is the ion induced dewetting of metallic films on the non-wetable dielectric substrate under energetic ions irradiation. The island films shape is strongly related to the dewetting behavior under ion irradiaiton, which is different from the electron and laser beam irradiation [25, 26]. After the dewetting process, the sputtering will modify the shape of the nanostructures as the sputtering yield is depends on the surface morphology (Sigmund's prediction). Therefore, this will cause a shift of the surface plasmon absorption position according to Gan's prediction. However, this is not verified by experiment yet.

The nanoparticles sizes are also strongly related to the irradiation parameters (beam energy and irradiation fluence) and also the metallic films' thickness. This is a stainght forward result: the retained Au films decreased as increase the ion irradiation fluence. Therefore, the nanostructures size will inevitably decrease as increase the irradiation fluence. In addition, the sputtering yields are enhanced for the nanoclusters on the dielectric substrate [42]. Therefore, this will cause a shift of the surface plasmon absorption position to the shorter wavelength according to Mie's prediction. However, in the Gangopadhyay's pioneer work pulished in 2010, a shift of the surface plasmon absorption position to the longer wavelength as increase the irradiation fluence was observed, and the underlying mechanism is not clarified yet.

(B) Ion beam irradiation induced embedment and satellite nanoparticle formation

The substrate effects should be taken into consideration. Xu *et. al* [41] conducted the cross sectional observation of the metallic films behavior on SiO_2/Si substrate under 800 keV Kr ion irradiation, and they discovered the burrowing effects of nanoparticles

into SiO_2 substrate under ion irradiation. The burrowing of the nanoparticle in the dielectric substrate increases the surrounding dielectric function, which leading to the red shift of the LSPR peak position. The detailed study of nanoparticles' burrowing effect was studied in detail by Klimmer *et. al.* in 2009 [42], and they concluded the single crystal sapphire has such low viscoucity that the burrowing effect is neglected. Therefore, the optical response of nanostructures on sapphire substrate needs to be clarified.

In addition, satellite nanoparticles formed around the main nanoparticles for the higher fluence irradiation, as already observed by Xu *et. al*. [41]. Latter, G. Pellegrini *et. al*. have studied ion irradiation effect on satellite nanoparticle formation around the core nanoparticle [44, 45]. In addition, they have a detailed study of the strong coupling effects of satellite nanoparticles with core nanoparticle on the optical response (multi-sphere scattering effects), in which generalized multi-scattering Mie theory is applied to model the surface plasmon absorption position shift behavior. They confirmed the shift of surface plasmon absorption position towards the longer wavelength due to this strong coupling. However, this effect is not studied experimentally in the optical response of nanoparticles fabricated by ion irradition technique.

(C) Ion mixing induced chemical concentration change

Interface mixing is a well know phenomenon in ion beam irradiation technique. The poinnered work on ion induced interface mixing of metallic films on dielectric substrate (glass and sapphire) was dated back to 1980's, in which they used ion mixing to increase the adhesive of metallic film to the non-reactive dielectrix substrate [33, 34].

Therefore, some Si atoms will recoil into the metallic island films and metal-silicon alloys formed in the nanostructures [39]. Therefore, this will have a contribution to the shift of surface plasmon absorption position. Unfortunately, there is no sufficient experiment result to clarify this issue. In addition, the local refractive index was increased because of the metal atoms dispersed in the dielectric matrix due to the irradiation induced forward recoiling, which is assumed to have a contribution on the red shift of the SPR absorption band. This also is not clarified experimentally until now.

(D) The optical response dependence on chemical component of the deposited metallic films

In general, the dielectric function of the bimetallic nanoparticles is different from the pure metallic nanoparticles. Therefore, the resulting surface plasmon excitation frequency lies in between that of the pure components, and depends on the relative amounts of the two components. However, there is no sufficient experimental study based on ion irradiation technique.

My Proposals

In summary, there are many studies on ion irradiation induced surface nanostructuring. However, there are still a gap between the ion induced nanostructuring of metallic films and their optical properties, as discussed in the above. In general, these unsolved issues can be summarized into 3 categaries:

1. The microstructure study is lack to clarify the relationship of nanoparticle's shape, size, and morphology (core-satallite structure) on the nanoparticles surface plasmon absorption behavior.

2. The studies of nanoparticles optical response dependence on the substrate (embedding depth, amorphous or single crystal) are not sufficient.

3. The studies of the nanoparticles chemical concentration (nominated chemical concentration and the impurities introduce by ion irradiation) dependence on their optical response is unclear.

The aim of this thesis is to clarify these unsolved issures as many as possible. Due to the present experimental conditions and the time limitation, the experimental arrangement is proposed in the following:

Firstly, the metallic films (various thickness) surface nanostructuring under Ar ion irradiation with various irradiation parameters (beam energy, current, and fluences) are analysized by AFM and SEM observation. The cross-sectional microstructure is characterized by TEM observation and selected area diffraction pattern. Also, the embedment depth could be obtained from cross-sectional TEM observation. In addition, SEM-EDS and TEM-EDS are used to get the chemical component concentrions in the

nanoscale. These informations are crucial important to clarify the dependence of nanoparticle's shape, size, and morphology (core-satallite structure) on surface plasmon excitation behavior.

Secondly, bimetallic film is used to study the chemical component dependence on optical response. Ag-Au bimetallic film was used in my study because Ag-Au alloy has composition–dependent surface plasmon excitation behavior and because complete miscibility of Au and Ag can be obtained at any composition in both bulk materials and nanoparticles. Also, theoretical estimation to the surface plasmon excitation behavior is required to confirm the reliability of experimental results.

Finally, ion surface nanostructuring of the same bimetallic films deposited on the sapphire substrate is conducted. The information based on surface plasmon excitation behavior of metallic nanostructures on sapphire is expected to estimate the substrate effects.

In summary, dependence of irradiation parameters (fluence, ion beam energy) and substrate surface conditions (amorphous, single crystal) on surface nanostructuring and their optical response behavior by ion beam irradiation are experimentally studied and these informations are expected to solve the unclear issues pointed out in this section.

1.6 Outline of The Thesis

The first chapter provides a brief and fairly general theoretical background, aiming to bridge the gap between ion beam surface nanostructuring and their optical properties. Chapter 2 gives a detailed description of the experimental procedures.

Chapter 3: Highlighting the experimental results of ion-beam surface nanostructruring in Au thin film dielectric substrate systems. The dewetting of the Au films on the SiO_2 glass substrate was occurred with the increase of the irradiation fluence, and a single layer of photosensitive gold nanoballs with highly spherical shape embedded in a SiO_2 substrate was obtained.

Chapter 4: Ag(50%)–Au(50%) bimetallic nanospheroids on the SiO_2 substrate were formed Ar–ion irradiation. The mean size of the nanospheroids decreases and the aspect ratio approaches unity with the increase in the irradiation fluence, resulting in a shift of the LSPR peaks towards the shorter wavelength. In addition, a remarkable LSPR peaks shifted approximately linearly towards the longer wavelength with the increase of the Au concentration has been obtained.

Chapter 5: the process of ion irradiation induced surface nanostructuring of Ag–Au bimetallic films on sapphire substrates was studied. Dependence of the LSPR on the chemical concentration was observed, and the LSPR peaks exhibited a tendency of red–shift with the increasing Au concentration.

Chapter 6: In conclusion, ion irradiation is an effective approach in surface nanostructuring and in controlling the LSPR properties of the metallic films on dielectric substrates, such as SiO_2 and sapphire, and the application of these nanocomposites in optical devices is expected.

2 Experimental Procedure

2.1 Specimen Preparation

Evaporation is a common method for thin film deposition [1, 2]. The vacuum allows vapor particles to travel directly to the target object (substrate), where they condense back to a solid state. Evaporation involves two basic processes: a hot source material evaporates and condenses on the substrate. In high vacuum (with a long mean free path), evaporated particles can travel directly to the deposition target without colliding with the background gas. Any evaporation system includes an energy source that evaporates the material to be deposited. Thermal evaporation is accomplished by passing a large current through a resistive wire or foil containing the material to be deposited. The heating element is often referred to as an evaporation source.

In our study, Au and/or Ag thin films were thermally evaporated on mirror polished amorphous SiO_2 or single crystal alumina (sapphire) substrates at room temperature by electrically heating the Au (purity, 99.5%) and/or Ag source in a 6.0×10^{-5} Torr vacuum placed on tungsten baskets (Figure 2.1). The thickness of the Au/Ag films was estimated by comparing the colors with that of the standard sample, which had been previously calibrated. The film thickness was also verified by transmission electron microscope, and a field–emission scanning electron microscope equipped with an energy-dispersive spectrometer was used for measuring the surface morphology and the chemical concentration of the as–deposited films.

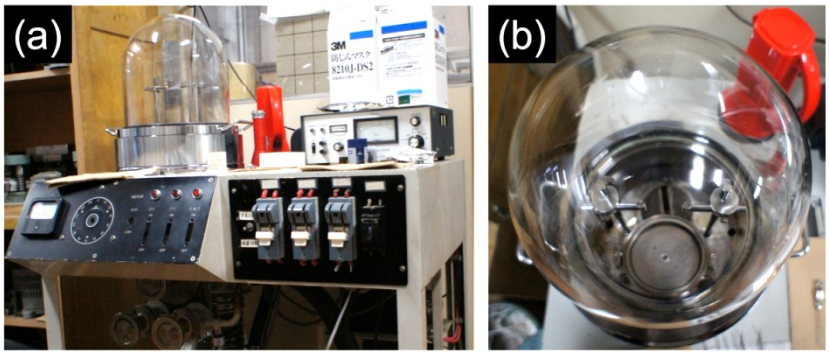

Fig. 2.1 (a) overview of the thermal evaporation deposition equipment; (b) the Ag (Au) wires were put on the tungust basket in the vacuum chamber.

For example, the 5 nm Au metallic thin films deposited on the SiO_2 substrates, the optical micrograph exhibits a blue color (Fig. 2.2a,) and the surface shows a continuous net-work like patterns with cracks (SEM micrograph in Fig. 2.2b).

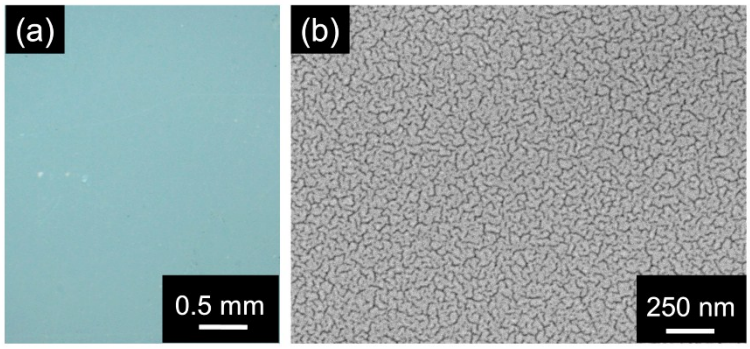

Fig. 2.2 (a) optical micrograph and (b) SEM micrograph of 5 nm Au thin films deposited on the SiO_2 substrates

2.2 Ion Irradiation

Subsequently, 10 nm and 30 nm Au films deposited samples were irradiated by 100 and 250 keV Ar ions at ambient temperature with verious fluences and fluxes. Energies of the ions have been chosen in such a way that the range is wider than the Au film thickness, as calculated by the SRIM 2011 code [3], shown in Figure 2.3.

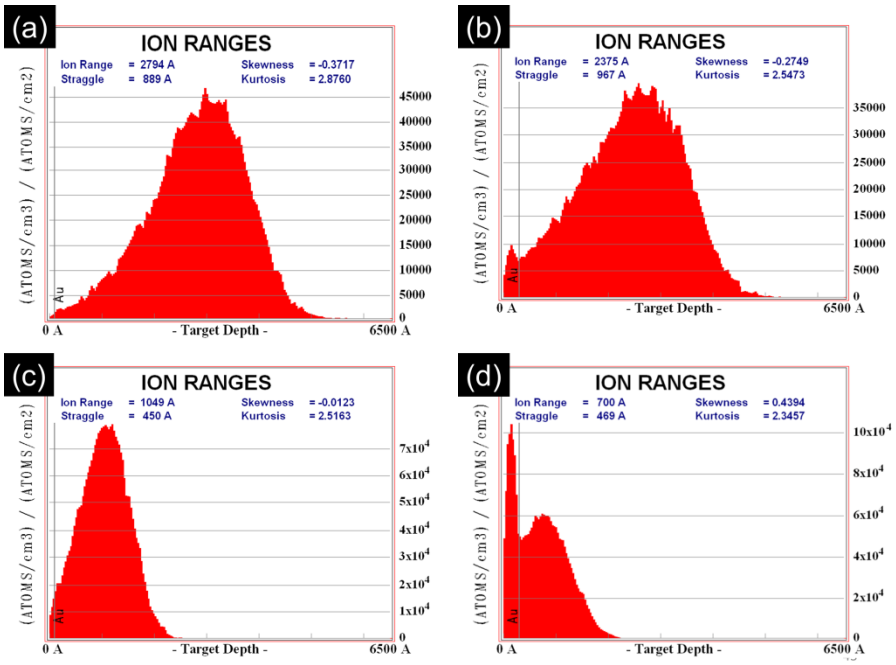

Fig. 2.3 SRIM calculation of the 250 keV Ar-ion distribution in the (a) 10 nm and (b) 30nm Au metallic film deposited on SiO_2 glass substrates; 100 keV Ar-ion distribution in the (c) 10 nm and (d) 30nm Au metallic film deposited on SiO_2 glass substrates.

Figure 2.3 was calculated to set the Au film thickness to be 10 and 30 nm, the Ar ion beam energy to be 100 and 250 keV, and the total number of incidence ions to be 20000. Compared with Figure 2.3a and c, we can see 10 nm Au film has very limited effects for the Ar distribution in the SiO_2 substrate, especially the 250 keV Ar has a much longer range in the substrate. It is obvious that for 250 keV Ar ions, the range (280 nm) is

much large than the range for 100 keV Ar ions (105 nm). Importantly, the 30nm Au film will have an effect on the Ar ions distribution in the SiO_2 substrate. It is noticed that Ar ion distribution has a peak in the 30 nm Au films (Fig. 2.3b and d). However, 250 keV Ar ions distribution peak in the 30 nm Au film is much smaller than that in the case of the 100 keVAr ions. Therefore, I conclude that thicker Au film and lower irradiation energy will induce more interaction between Ar with surface, and the pronounced surface nanostructuring by ion irradiation is achieved. Therefore, 100 keV Ar ion was choose to irradiated 30 nm metallic film deposited on dielectric matrix.

Experimentally, samples with 10 nm and 30 nm Au films deposited on SiO_2 galss were irradiated by 250 and 100 keV Ar ions, respectively, at ambient temperature to a fluences of 1.0×10^{17} cm^{-2}. For the 10 nm Au film on SiO_2 after Ar ion irradiation, the surface morphology is given in Fig. 2.4a and the corresponding cross-sectional TEM image is given in Fig. 2.4b. Compared with the case of 100 keV Ar ion irradiation of 30 nm Au film, there was no homogenous Au nanoball embedded in the substrate. Only the Ar bubbles were clearly identified. This means the Ar atoms penetrated the Au layer and aggregated to from Ar bubbles. Therefore, thsese differences emphasizes that proper beam energy and gold film thickness are necessary to achieve Au nanoballs embedded in a dielectric substrate.

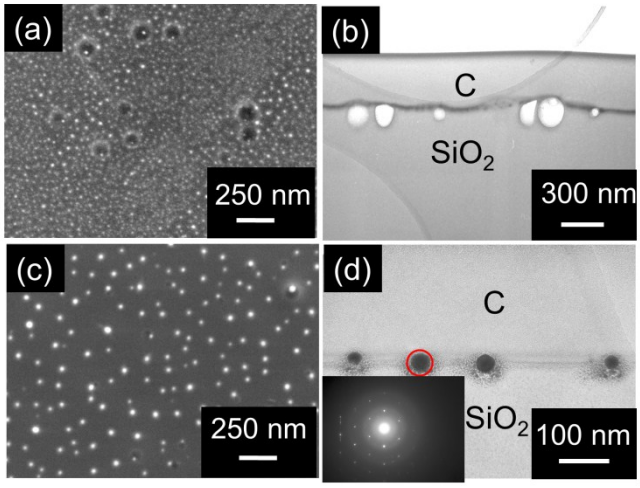

Fig. 2.4 SEM image of (a) 10 nm Au on SiO_2 irradiated by 250 keV Ar ions to a fluence of 1.0×10^{17} cm^{-2}; (b) Bright field cross–sectional TEM image of 10 nm Au on SiO_2 irradiated by 250 keV Ar ions to a fluence of 1.0×10^{17} cm^{-2}; (c) SEM image of 30 nm Au on SiO_2 irradiated with 100 keV Ar ions to a fluence of 1.0×10^{17} cm^{-2}; (d) Bright field cross–sectional TEM image with selected area diffraction pattern of 30 nm Au on SiO_2 irradiated with 100 keV Ar ions to a fluence of 1.0×10^{17} cm^{-2}.

Ar ion irradiation perpendicular to the specimen was performed using the 400 keV ion accelerator at High Voltage Electron Microscope Laboratory, Hokkaido University (Figure 2.5) [4]. A low pressure of 4.3×10^{-3} Pa was maintained inside the irradiation chamber. To ensure uniform irradiation, Ar beam was scanned and the current was kept between 1.0~2.0 $\mu A/cm^2$. Also, the target was continuously monitored by thermocouple and infrared thermal detectors, and the temperature at the beam spot was maintained below 150 °C.

400 keV Ion accelerator at High Voltage Electron Microscope Laboratory

The ion implantor is part of the multi-beam high voltage electron microscope system, which has a sputtering ion source. Ar gas was used as a sputtering gas, Au, Fe, Ni, … can be sputtered and extracted from the ion source with a beam current around 0.2 μA. the pressure in the ion source is aound 10^{-3} Pa. For the ion source, arc current is around 50 mA; maximum filament current is around 180 A and filament voltage is around 100V. The extraction voltage is 25 KV and the extraction current is around 0.3 mA; the implanting voltage can be increased to 375 KV. Ar ion was used in my study and the beam can be scaned with a frequency of 1.25 kHz.

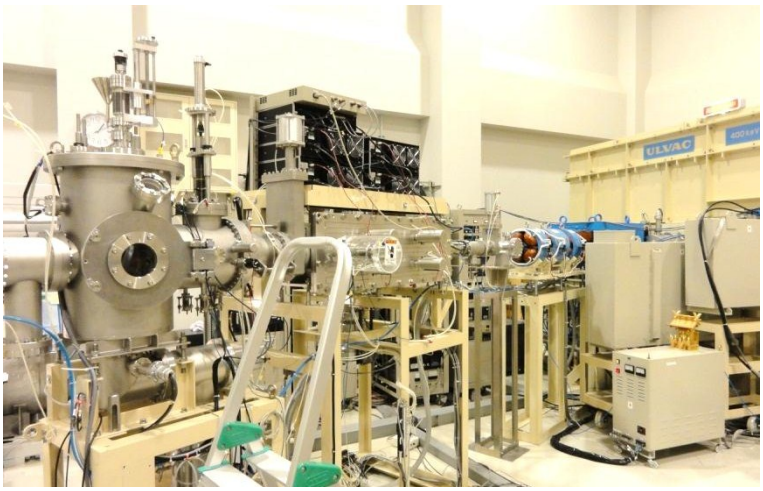

Fig. 2.5: A overview of the 400keV ion accelerator.

2.3 Surface Morphology and Microstructure Characterization

2.3.1 Spectrophotometry

A spectrophotometer is a photometer that measures intensity as a function of the light source wavelength, which is commonly used for the measurement of transmittance or reflectance of solutions, transparent or opaque solids, such as polished glass, or gases [5, 6]. In addition, the common spectrophotometers are used in the UV and visible regions of the light spectrum. There are two major classes of devices: single beam spectrophotometer and double beam spectrophotometer. A double beam spectrophotometer compares the light intensity between two light paths, one path containing a reference sample and the other the test sample.

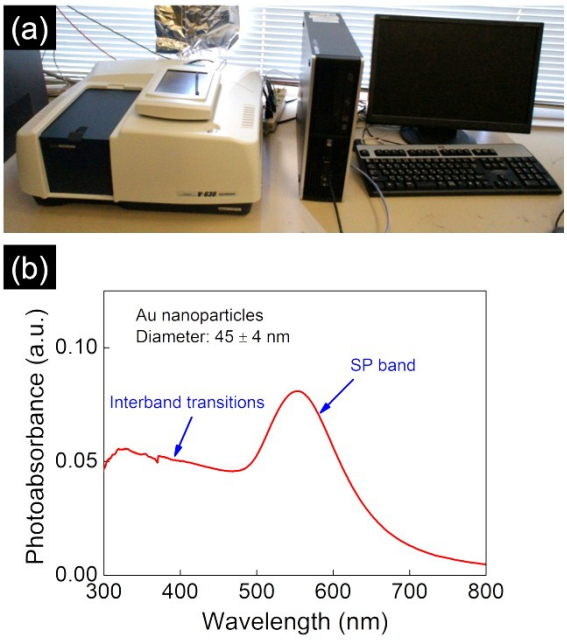

Fig. 2.6 (a) A overview of the spectrophotometer (JASCO V–630). (b) Optical absorption spectra for Au nanoparticles with diameters of 45±5 nm (embedded in a silica matrix with $\varepsilon = 2.25$), in which the contributions to the optical absorption of interband transitions and SPs are indicated.

In my study, optical absorption spectra were recorded by using a spectrophotometer (JASCO V–630) with iRM-700 intelligent remote module (Fig. 2.6a), which has a double-beam spectrophotometer with single monochromator and silicon photodiode detectors, the detection range is between 190 to 1100 nm with a spectral bandwidth of 1.5 nm. For example, there are Au nanoballs with a size of 45±5 nm formed on the sample of 30 nm Au film on SiO_2 irradiated with 100 keV Ar ions at fluence of 1.0×10^{17} cm^{-2}. The photo absorbance spectrum was measured (Fig. 2.6b), which shows a locallized surface plasmon resonance (LSPR) band resulted from the collective excitation of the free electrons. At the shorter wavelength side, the absorbance is due to the electronic resonance resulted from the interband electron transition [6].

2.3.2 Atomic force microscopy

Atomic force microscopy (AFM) is a high-resolution type of scanning probe microscopy, with demonstrated resolution on the order nanometer. It is one of the foremost tools for imaging, measuring, and manipulating matter at the nanoscale. The primary modes of operation for an AFM are static mode and tapping mode.

In my study, the surface morphology was analyzed using an atomic force microscope (AFM; KEYENCE VN–8000) (Figure 2.7d) working in the tapping mode. For example, the surface morphology of 30 nm Au on SiO_2 irradiated with 100 keV Ar ions at fluences of 1.0×10^{16} cm^{-2} was obtained (Fig. 2.7a) with the contour map image (Fig. 2.7b), with the coloured scale bar shown in the right side. In addition, the height profile along the horizontal line indicated in Fig. 2.7a can be obtained (Fig. 2.7c), and we can measure the nanostructures size and height, and therefore the volume.

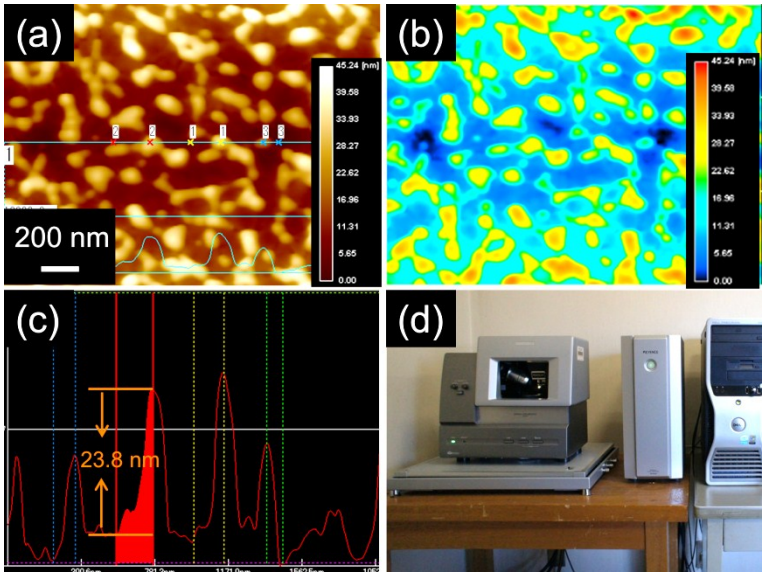

Fig. 2.7: (a) AFM image of 30 nm Au on SiO_2 irradiated with 100 keV Ar ions at fluences of $1.0 \times 10^{16}/cm^2$; (b); contour map image; (c) line profile along the horizontal line indicated in a, the hight of the nanostructure can be obtained at point 2 in a; and (d) a overview of AFM.

2.3.3 Scanning electron microscopy

A scanning electron microscope (SEM) is a type of electron microscope that produces images of a sample by scanning it with a focused beam of electrons. The electrons interact with atoms in the sample, producing various signals that can be detected and that contain information about the sample's surface topography and composition. The electron beam is generally scanned across the sample, and the beam's position is combined with the detected signal to produce an image.

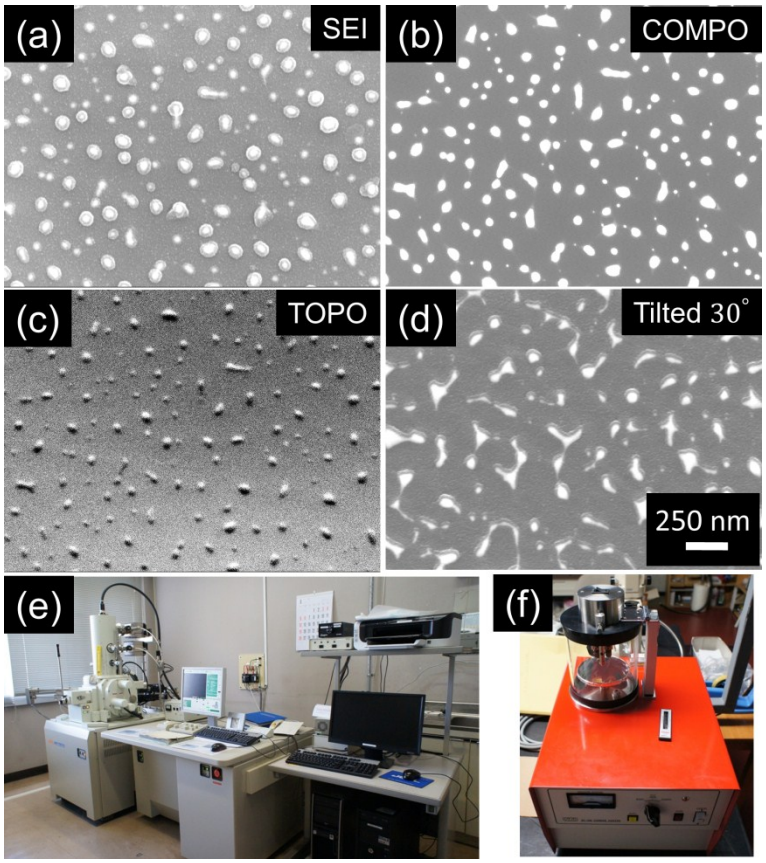

Fig. 2.8: SEM images of 30 nm $Ag_{75\%}$–$Au_{25\%}$ bimetallic film on SiO_2 irradiated with 100 keV Ar ions to a fluence of $1.0 \times 10^{17}/cm^2$: (a) SEI image; (b) COMPO image; (c) TOPO image; (d) SEI image tilted 30 degrees; (e) Overview of SEM and (f) Overview of carbon coator.

The signals result from interactions of the electron beam with atoms at or near the surface of the sample include secondary electrons (SE), back-scattered electrons (BSE), characteristic X-rays. Secondary electron detectors are standard equipment in all SEMs, but it is rare that a single machine would have detectors for all possible signals. In the most common or standard detection mode, secondary electron imaging or SEI (Figure 2.8a), Compo image (Figure 2.8b) and Topo image (Figure 2.8c) can be obtained. Also, the specimen can be tilted to a certain degree, in order to see the cross sectional morphology (Figure 2.8d).

Nonconductive specimens tend to charge up when scanned by the electron beam, and especially in secondary electron imaging mode, this causes scanning faults and artificial image. They are therefore usually coated with an ultrathin layer of electrically conducting material. Conductive materials in this study for specimen coating is graphite. However, we need to control the thickness of the deposited carbon layer. Uausally, 10 to 20 nm is enough for the dielectric substrate (Fig. 2.9a), if the graphite is over coated, (for example, more than 40 nm), we would get the artificial image (Fig. 2.9b).

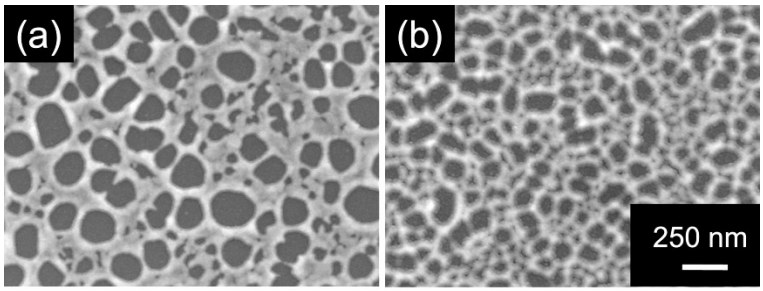

Fig. 2.9: SEM images of 30 nm $Ag_{50\%}$–$Au_{50\%}$ bimetallic film on Sapphire irradiated with 100 keV Ar ions to a fluence of $1.0 \times 10^{16}/cm^2$ with carbon depositions of (a) 10 nm and (b) 40nm.

The SEM has pronounced advantages, including the ability to image a comparatively large area of the specimen; the ability to image bulk materials (not just thin films or

foils); and the variety of analytical modes available for measuring the composition and properties of the specimen. Characteristic X-rays are emitted when the electron beam removes an inner shell electron from the sample. These characteristic X-rays are used to identify the composition and measure the abundance of elements in the sample. For example, point elemental concentration spectrum (Fig. 2.10), the line profile of elemental concentration (Fig. 2.11) and the elemental concentration maps can be obtained.

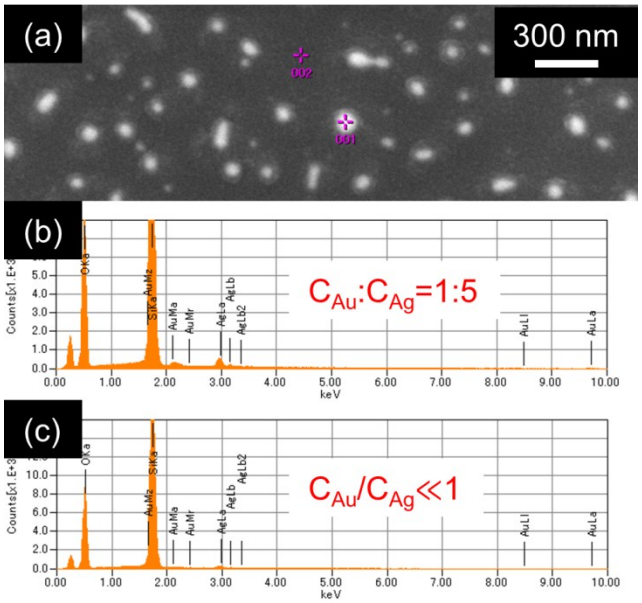

Fig. 2.10 (a) Typical SEM micrograph of a post–irradiation annealed sample of $Ag_{75\%}$–$Au_{25\%}$ bimetallic film on SiO_2 at a fluence of $1.0 \times 10^{17}/cm^2$; (b) gold and silver point elemental concentration at point 001 indicated in (a) shows a molar ratio of approximately 1:5; (c) gold and silver point elemental concentration at point 002 indicated in (a) shows neglictable concentration.

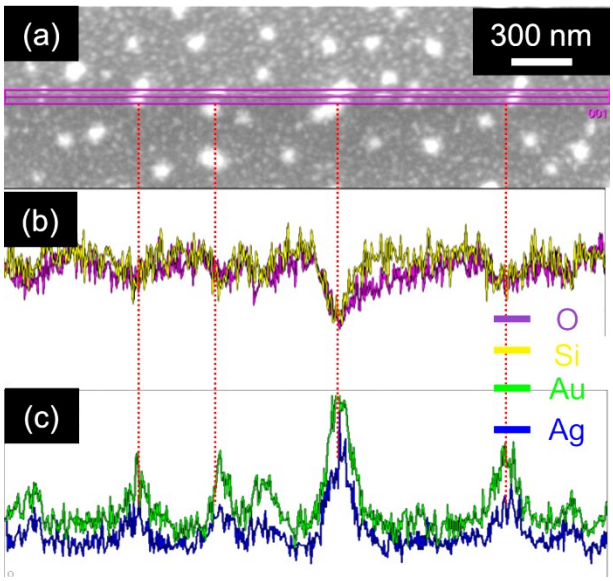

Fig. 2.11 (a) Typical SEM micrograph of a post–irradiation annealed sample of $Ag_{75\%}$–$Au_{25\%}$ bimetallic film on SiO_2 at a fluence of $1.0 \times 10^{17}/cm^2$; (b) line profiles of oxygen and silica along the horizontal line indicated in (a); (c) line profiles of gold and silver along the horizontal line indicated in (a).

In my study, a field–emission scanning electron microscope (SEM; JEOL JSM–7001FA) (Figure 2.8e) equipped with an energy dispersive spectrometer was used for measuring the surface morphology and the chemical concentration of the specimens. As SiO_2 and Sapphire have a poor conductivity, a thin layer of 10~20 nm carbon was usually deposited on the sample to increase the conductivity during SEM observation. The surface element concentration was evaluated by point energy–dispersive spectrometer (EDS) analysis (Fig. 2.10). The line (Fig. 2.11) element concentration patterns were indentified at nanoscale using the energy–dispersive spectrometer (EDS). Some of the line and surface chemical concentration profiles cross the surface were obtained when the SEM was operated at 6.0 keV.

2.3.4 Transmission electron microscopy

Transmission electron microscopy (TEM) is a microscopy technique whereby a beam of electrons is transmitted through an ultra-thin specimen. An image is formed from the interaction of the electrons transmitted through the specimen; the image is magnified and focused onto an imaging device, such as a fluorescent screen, a layer of photographic film, or to be detected by a sensor such as a CCD camera. TEMs are capable of imaging at a significantly higher resolution owing to the small de Broglie wavelength of electrons. This enables the user to examine fine structures, even as small as a single column of atoms.

In my study, microstructural characterization was performed by the cross–sectional transmission electron microscope (TEM; JEOL JEM–2010FE) operated at 200 keV, and the elemental concentration was obtained in the nanoscale by operating the TEM in the scanning mode, accompanied with an energy–dispersive spectrometer (Noran, Thermo Fischer Scientific). Cross–sectional TEM samples were prepared both by Precision Ion Polishing System (PIPS; JEOL AT–12310) and focused ion beam facility (JEOL JEM–9320FIB). A cold stage is used during oprating the PIPS and it is cold down by the liquid nitrgin.

2.4 Thermal Annealing Equipment

A quartz tube furnace is an electric heating device extensively used in material research. The commonly used quartz tubes are made of 99.9% SiO_2 and the maximum constant working temperature is 1200 °C. The length of the quartz tubes used in my study is 90 cm (Figure 2.12d). The temperature is controlled via a feedback from a thermocouple. The temperature controllers allows the operator to program the heating, dwelling and cooling rates. Generally, dewetting occurs when the thin metallic film annealed [7] (Fig. 2.12b), compared with the thin Au film before annealing (Fig. 2.12a). In addition, the photoabsorption changed (Fig. 2.12c).

As the radiation induced defects can be removed by annealing at temperatures higher than 623 K, post–irradiation thermal annealing is usually employed to anneal ion irradiated samples [8]. Therefore, thermal annealing was conducted *ex–situ* under high vacuum (4.25×10^{-5} Pa) at 773 K for two hours in my study. After that, optical absorption spectra were recorded using the spectrophotometer and the SEM observations were used to examine the surface modification. Moreover, microstructural characterization was performed using the TEM.

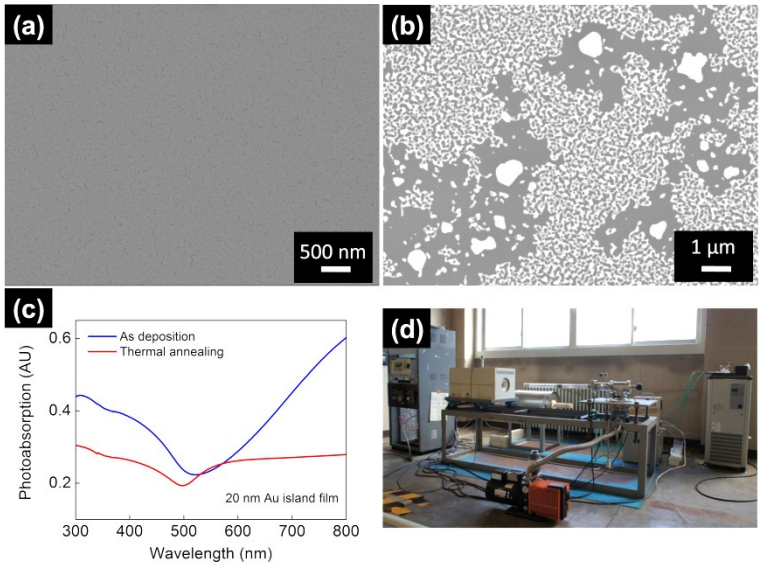

Fig. 2.12 (a) 20 nm Au film as-deposited on SiO_2; (b) 20 nm Au film on SiO_2 annealed at 773 K for 2 hours, (c) the photoabsorption spectra before and after the thermal annealing; (d) Overview of the thermal annealing system.

3 Ion Beam Surface Nanostructuring of Thin Au Film on SiO_2 Glass

3.1 Introduction

Surface–interface modification in metal–dielectric systems can be obtained using low–energy ion irradiation. Low–energy ions up to few hundred keV undergo nuclear stopping and the energy deposition is dominated by nuclear energy loss, which effectively induces mass transfer and therefore effectively introduces surface structuring. On the other hand, ion irradiation resulted in lattice damage and the microstructure evolution of the thin metal films on dielectric surface. The process of the ion beam induced surface nanostructuring on a dielectric substrate depends on the variation of irradiation parameters such as fluence, current and ion beam energy.

In this study, ion induced surface nanostructuring of Au films deposited on the SiO_2 glass substrates was examined, and ion induced lattice evolution and the chemical concentration of thin Au films were investigated. Also, the effects of ion beam energy on Au nanostructures on the SiO_2 glass substrates and on the photo absorption properties were also studied.

3.2 Experimental Details

Au thin films were evaporated on mirror polished SiO_2 substrates with an O–H density of 80–100 ppm (Shin–Etsu Chemical Co., Ltd.) at room temperature by electrically heating the Au source (purity, 99.9%) in a 6.0×10^{-5} Torr vacuum. The thickness of the Au films was estimated to be 30 nm by comparing the colors with that of the standard sample, which had been previously calibrated. Also, the film thickness was verified by cross–sectional transmission electron microscope (TEM; JEOL JEM–2010FE) observation. After the deposition, the surface morphology was analyzed using an atomic force microscope (AFM; KEYENCE VN–8000) working in the tapping mode. In addition, a field emission scanning electron microscope (SEM; JEOL JSM–7001FA) equipped with an energy dispersive spectrometer was used to verify the surface morphology and the chemical concentration.

Subsequently, as–deposited samples were irradiated by 100 keV Ar ions at ambient temperature with fluences of 1.0×10^{16} cm^{-2}, 2.0×10^{16} cm^{-2}, 6.0×10^{16} cm^{-2}, and 1.0×10^{17} cm^{-2}. In addition, the Ar ion irradiation at 150 keV was also carried out to a fluence of 1.0×10^{17} cm^{-2}. Energies of the ions have been chosen in such a way that the range is wider than the Au film thickness, as calculated by the SRIM 2011 code [1]. Ar ion irradiation perpendicular to the specimen was performed. A low pressure of 4.3×10^{-3} Pa was maintained inside the irradiation chamber. To ensure uniform irradiation, Ar beam was scanned and the current was kept around 2.0 μA cm^{-2}. Also, the target was continuously monitored by thermocouple and infrared thermal detectors, and the temperature of the beam spot was maintained below 120 °C.

After the irradiation, the photoabsorbance spectra were obtained using the Spectrophotometer (JASCO FP–6200), equipped with a UV measurement attachment (model FUV–420), at a wavelength range between 280 and 725 nm. After that, the AFM and the SEM were used to examine the surface modification. Microstructural characterization was performed by the TEM operated at 200 keV, and the elemental concentration was obtained in the nanoscale by operating the TEM in the scanning mode, accompanied with an energy–dispersive spectrometer (Noran, Thermo Fischer Scientific). Cross–sectional TEM specimens were prepared both by Precision Ion Polishing System (PIPS; JEOL AT–12310) and focused ion beam facility (JEOL JEM–9320FIB).

3.3 Results

The process of the ion beam induced surface nanostructuring on a dielectric substrate depends on the variation of irradiation parameters such as fluence, current and energy of the ion beam. In this study, the fabrication of Au nanoparticles with controlled size and shape in a two–dimensional distribution can be achieved by applying the appropriate irradiation fluence, beam energy and Au foil's thickness [2-6].

3.3.1 Surface nanostructuring after Ar ion irradiation

Surface morphology of the samples was examined before and after irradiation using AFM and SEM. Figure 3.1 gives the AFM images of samples irradiated with 100 keV Ar ions at the fluence of (b) 1.0×10^{16} cm^{-2}, (c) 6.0×10^{16} cm^{-2}, and (d) 1.0×10^{17} cm^{-2}.

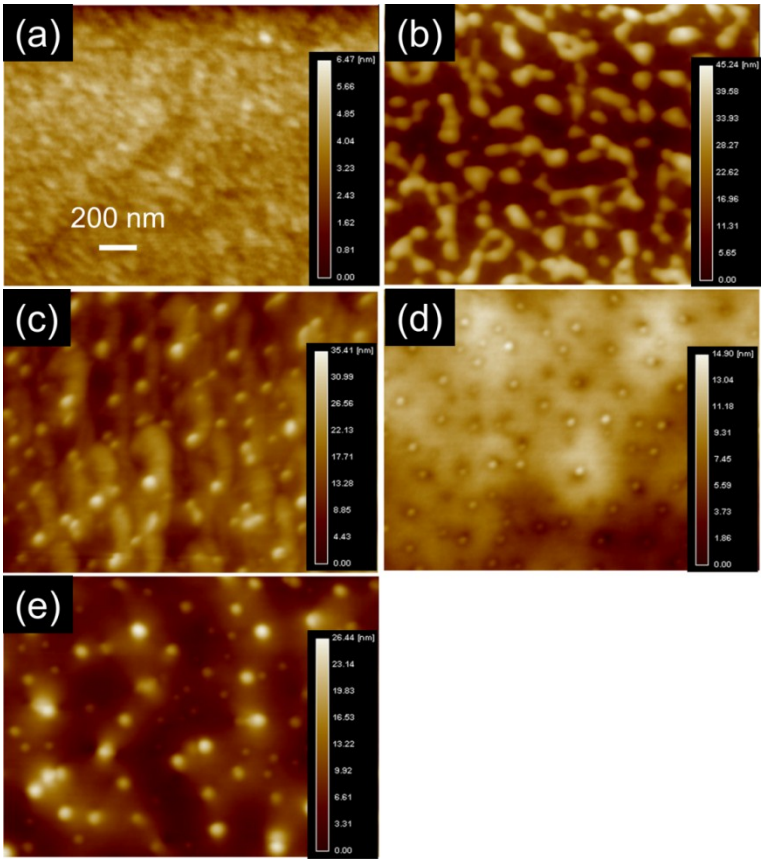

Fig. 3.1 AFM micrographs (2.0 μm × 1.5 μm) with the Z scale of nm of (a) as–deposited SiO_2, samples irradiated with 100 keV Ar ions at fluences of (b) 1.0×10^{16} cm^{-2}, (c) 6.0×10^{16} cm^{-2}, (d) 1.0×10^{17} cm^{-2}, and (e) the sample irradiated with 150 keV Ar ions at a fluence of 1.0×10^{17} cm^{-2}.

The corresponding SEM images are given in Fig. 3.2, in which the bright parts represents the Au films and the dark parts represents the exposed substrate. Therefore, the process of Au film's dewetting under Ar ion irradiation was clearly distinguished and finally the formation of nanodots was observed.

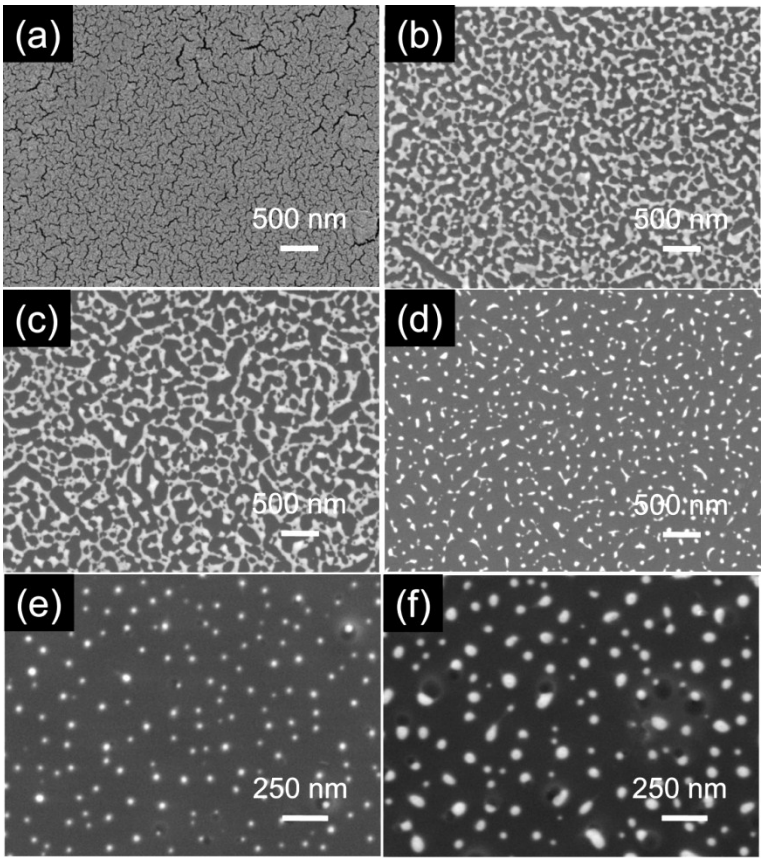

Fig. 3.2 SEM images of (a) as–deposited SiO_2, samples irradiated with 100 keV Ar ions at fluences of (b) 1.0×10^{16} cm^{-2}, (c) 2.0×10^{16} cm^{-2}, (d) 6.0×10^{16} cm^{-2}, (e) 1.0×10^{17} cm^{-2}, and (f) the sample irradiated with 150 keV Ar ions at a fluence of 1.0×10^{17} cm^{-2}.

While the surface of the as–deposited SiO_2 glass substrate was smooth with homogenous cracks (shown in Fig. 3.2a), which can be confirmed by cross–sectional TEM image shown in Fig. 3.3a, the holes and partially connected nanoscale islands were formed by the lateral transport of Au atoms after irradiated to a fluence of 1.0×10^{16} cm^{-2}. It is therefore concluded that the cracks are the triggers of the holes formation and therefore starting the dewetting process, which is enhanced by the Ar ion irradiation, taking into the effect of surface sputtering. As the fluence increased to 2.0×10^{16} cm^{-2}, the nanoscale Au islands on the surface became discontinuous. Similar features of ion induced dewetting have been reported by 800 keV Kr^{++} ion irradiation of thin Pt films on SiO_2 substrate [2, 3] and 150 keV Ar ion irradiation of thin Au films on carbonaceous substrate [5], and the mechanism of the irradiation enhanced dewetting was ascribed to be the radiation enhanced diffusion [6, 7].

At the higher fluence of 6.0×10^{16} cm^{-2}, the spherical nanodots on the substrate were observed. Compared with the surrounding areas, the aggregation of Au atoms in the nanodots was identified by SEM–EDS spectra, and these nanodots were therefore entitled Au nanoballs. When the irradiation fluence increased to 1.0×10^{17} cm^{-2}, the nanoballs were modified to be highly spherical nanoballs. In addition, two–dimensional autocorrelation function image of the SEM image indicate the nanoballs has a homogenous distribution along their radius. Figure 3.5a gives the size distribution of these nanoballs (NBs), reproduced by a Gaussian fit (black line). The mean diameter <D> was deduced as the position of the Gaussian peak and the error on <D> was evaluated as the standard deviation of the Gaussian fit. A mean diameter of 33.9 ± 8.8 nm was obtained with a number density of approximately 27.9 μm^{-2}. However, according to the AFM observation, the average height of the nanoballs was much

smaller than their lateral dimension. This can be clarified by the following cross–sectional TEM analysis: nanoballs with exposed height lesser than their lateral size would be embedded in the substrate.

3.3.2 Microstructure evolution after Ar ion irradiation

Figure 3.3 gives the bright field cross–sectional TEM images together with selected area diffraction pattern for the specimens irradiated with 100 keV Ar ions at the fluence of (b) 1.0×10^{16} cm^{-2}, (c) 2.0×10^{16} cm^{-2}, (d) 6.0×10^{16} cm^{-2}, and (e) 1.0×10^{17} cm^{-2}. While the diffraction pattern for the SiO_2 substrate showing diffused rings indicated the substrate was amorphous before and after the Ar ion irradiation, diffraction patterns with bright spots for the Au layers or nanoballs indicates a crystalline nature. In order to confirm the element concentrations of the nanostructures, a two dimensional EDS elemental mapping was obtained (shown in Fig. 3.4c) and the corresponding STEM image is given in Fig. 3.4a. The upper yellow area shows carbon deposition, which was used to protect the specimen during FIB sample preparation and the bottom area represents the SiO_2 glass substrate. The red nanoballs in the middle represent the Au atoms assembled in the form of spherical nanoballs and exhibit a single layer distribution. According to the primary measurement, around 50% of these nanoballs were found to be single crystals.

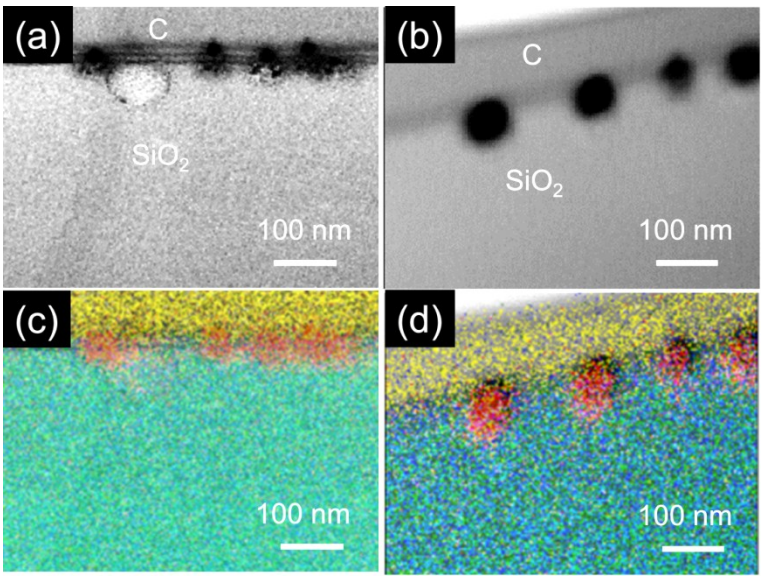

Fig. 3.4: Cross–sectional STEM image (a) with EDS mapping (c) of Au nanoballs embedded in SiO_2 substrates after 100 keV Ar ion irradiation to a fluence of $1.0 \times 10^{17}/cm^2$; STEM image (b) with EDS mapping (d) of Au nanoballs embedded in SiO_2 substrates after 150 keV Ar ion irradiation to a fluence of $1.0 \times 10^{17}/cm^2$.

Furthermore, diffraction patterns for several nanostructures with FCC structure for each irradiation fluence were obtained, and each image gives a typical diffraction pattern. These diffraction patterns enable us to study the lattice evolution under Ar ion irradiation. The lattice parameter at each irradiation fluence is given in Table 1, and an increase of lattice parameter with the irradiation fluence was observed. From the TEM observation, the Au nanoscale islands due to irradiation remained on the surface of the substrate at a fluence of 1.0×10^{16} cm^{-2}, while a lattice expansion was observed from several Au nanoscale islands. Therefore, lattice expansion (E) was defined (Eq. 3.1) to characterize the effects of ion irradiation:

$$E = (a_M - a_{Au})/a_{Au} \times 100\%, \quad (3.1)$$

where a_M is the lattice parameters of Au nanoscale islands after Ar ion irradiation and a_{Au} is the documented value corresponding to bulk Au [8]. A lattice expansion of 2.3 % was observed and irradiation induced defects like vacancies and interstitials have been ascribed to account for this lattice expansion.

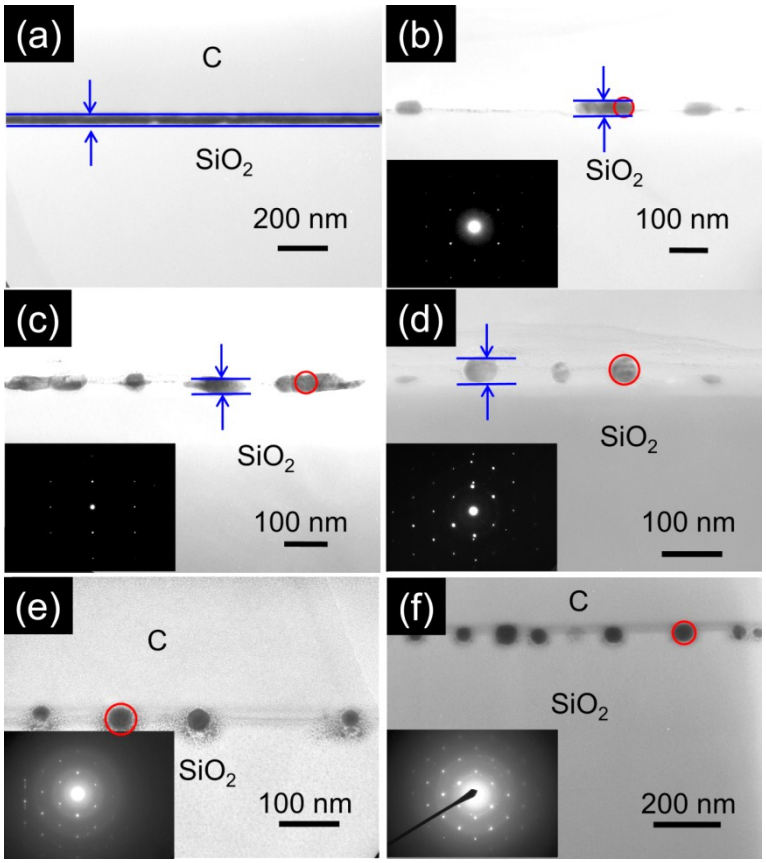

Fig. 3.3 Bright field cross–sectional TEM images with selected area diffraction pattern of (a) as–deposited SiO_2, samples irradiated with 100 keV Ar ions at fluences of (b) 1.0×10^{16} cm^{-2}, (c) 2.0×10^{16} cm^{-2}, (d) 6.0×10^{16} cm^{-2}, (e) 10.0×10^{16} cm^{-2}, and (f) the sample irradiated with 150 keV Ar ions at a fluence of 10.0×10^{16} cm^{-2}.

When the fluence of the irradiation increased to 2.0×10^{16} cm^{-2}, the interface between the Au nanoscale islands and the surface of the substrate became blurring, indicating the Au nanoscale islands began to burrow into the SiO_2 substrate. In addition, a lattice

expansion of 3.9 % was observed. When the fluence increased to 6.0×10^{16}cm^{-2}, nanostructures with fine particles surrounding the larger nanoballs partially embedded in the near surface with a layer distribution was identified, and a lattice expansion of 5.4 % was obtained. When the fluence increased to 1.0×10^{17} cm^{-2}, the Au nanoballs were modified to be highly spherical shape and deeply embedded in the substrate with a mean diameter of 33.3 ± 9.0 nm (given in Fig. 3.5c), and a lattice expansion of 15.7 % was obtained. As increasing the irradiation fluence up to 6.0×10^{16} cm^{-2}, the lattice expansion showed linear tendency. After the irradiation to a fluence of 1.0×10^{17}cm^{-2}, the lattice expansion deviated from the linear tendency. Because the sample of cross–sectional TEM specimen after 1.0×10^{17} cm^{-2} irradiation was prepared by FIB system, the Ga irradiation could also have a contribution to the lattice expansion.

Table 3.1: The expansion of the lattice parameter after Ar ion irradiation.

Specimens	Irradiation fluence	[a] a_{Au} (Å)	[b] a_M (Å)	Expansion (%)
100 keV Ar^+	1.0×10^{16} cm^{-2}	4.0786	4.04	2.3
	2.0×10^{16} cm^{-2}		4.24	3.9
	6.0×10^{16} cm^{-2}		4.30	5.4
	10.0×10^{16} cm^{-2}		4.72	15.7
150 keV Ar^+	10.0×10^{16} cm^{-2}		5.00	22.6

[a] a_{Au} represents the lattice parameter from the documented values [8]

[b] a_M represents the lattice parameters from measurement

The kinetic energy deposition due to continued Ar ion irradiation resulted in greater defects movement than that expected with ambient temperature, which can be 100 times faster [9]. This is referred as radiation–enhanced diffusion, which is thought to dominate the mass transport in ion mixing [6, 7]. Therefore, the Si atoms are inevitably recoiled into Au nanoparticles, which has a contribution to the nanoparticles lattice

expansion. In addition, the Ar ion irradiation induced defects also has a contribution to the nanoparticles lattice expansion. We have tried to clarify these two effects by experiment measurement (such as HR-TEM observation and also EDS spectra analysis) and it's hard to quantitatively estimation the concentration of the mixed Si atom. However, the lattice constant in this study was compared with several published Au silicates' lattice constant. Metastable Au–Si (hexagonal structure) alloys with larger lattice parameters were obtained by ion–beam interface mixing of Au–Si multilayers [10, 11] was obtained. However, the Au nanostructures showed FCC structure in this study. In addition, the published Au silicates' lattice constant is much larger (approximately 20% larger for the rarest Si concentration in a Au silicate). Therefore, I can make a conclusion that there are Si atoms mixed in Au nanoparticles in my study but they are not Au silicate.

The Au nanoballs embedment in the SiO_2 substrate can be interpreted as irradiation induced burrowing. The mechanism of the nanoballs burrowing was particularly investigated [12, 13]. Thermodynamic driving force, which related to the surface and interface energies of nanoballs and substrate, is account for this burrowing effect, and the sputtering effect of nanoballs was also taken into consideration. In addition, irradiation induced viscosity of the SiO_2 substrate was sufficient enough to accomplish this burrowing process [13]. In the following part, a detailed discussion of sputtering effect was given.

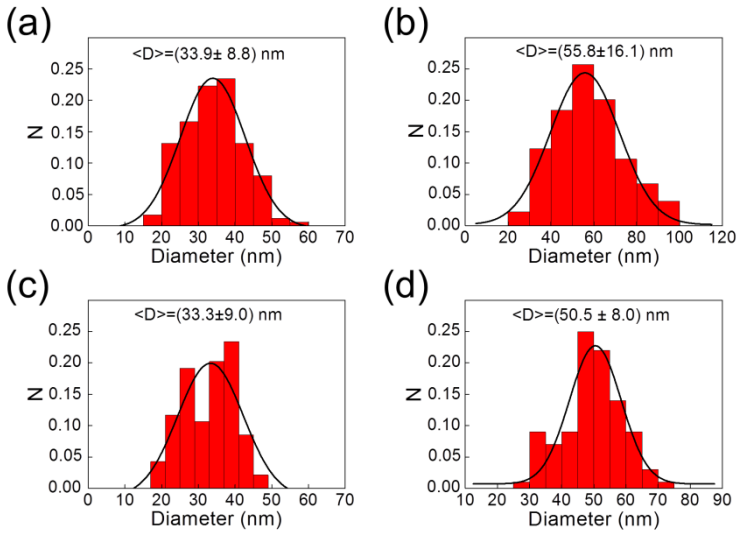

Fig. 3.5: Each figure shows the diameter distribution (N is the portion of Au nanoballs embedded in SiO_2 substrate, and <D> is the mean diameter of nanoballs) of the acquired nanoballs formed by Ar ion irradiation to a fluence of 1.0×10^{17} cm^{-2}: (a) SEM images exhibits a mean diameter of 33.9 ± 8.8 nm for the nanoballs under 100 keV Ar ion irradiation, and the corresponding TEM images exhibits a mean diameter of 33.3 ± 9.0 nm (c); (b) SEM images exhibits a mean diameter of 55.8 ± 16.1 nm for the nanoballs under 150 keV Ar ion irradiation, and the corresponding TEM images exhibits a mean diameter of 50.5 ± 8.0 nm (d).

3.3.3 Sputtering effects under Ar ion irradiation

For the specimens before and after irradiation up to 6.0×10^{16} cm^{-2}, the covered surface fractions of Au films can be obtained by integrate the bright parts in the SEM images (Fig. 3.2). In addition, the thickness of the Au films can be estimated using the cross–sectional TEM images (Fig. 3.3). Then the volume of the retained Au atoms within unit area on the SiO_2 substrate corresponding to each irradiation fluence can be obtained by simply multiply the Au covered region with the film thickness, and the uncertainty was also estimated.

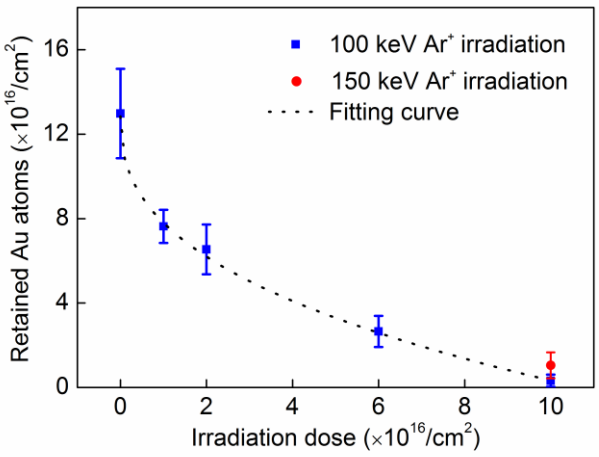

Fig. 3.6: Retained Au concentrations on SiO_2 substrate as a function of irradiation fluence.

For the highest irradiation fluence of 1.0×10^{17} cm^{-2}, the nanoballs were modified to be perfectly spherical nanoballs partially embedded in the substrate. Each Au nanoballs was treated as a sphere, and the volume of the Au nanoballs within unit area can be obtained by multiply the number density. Finally, Au atoms within unit area can be calculated by assuming the density of retained Au after ion irradiation kept the same as bulk Au, and the results are summarized in Fig. 3.6. Figure 3.6 shows the plot of concentration of Au varying with irradiation fluence which reveals sputtering effects of Au under ion irradiation. It shows that at the initial irradiation fluence of 1.0×10^{16} cm^{-2}, sputtering yield is about 5.4 atoms/ion. Afterwards, the retained Au atoms decreases with the irradiation fluence with a deviation from the linear tendency indicating the sputtering yields decreases with the irradiation fluence. At the highest irradiation fluence of 1.0×10^{17} cm^{-2}, the sputtering rate decreases to less than 0.6 atoms/ion. The reason for this low sputtering rate is the small fraction of surface area coverage by Au film which decreases with increasing irradiation fluence as observed in SEM images.

3.3.4 Beam energy dependence on the nanoballs formation

Figure 3.1e gives the AFM image of 150 keV Ar ions irradiation of the same sample to a fluence of 1.0×10^{17} cm^{-2}. The corresponding SEM image is given in Fig. 3.2f. The homogeneous distribution of Au nanoballs on the substrate was identified, and a mean diameter of 55.8 ± 16.1 nm was obtained (Fig. 3.5b) with a number density of approximately 26.3μm^{-2}. Figure 3.3f is the bright field cross–sectional TEM image, and the EDS elemental mapping is shown in Fig. 3.4d together with the corresponding STEM image in Fig. 3.4b. A layer of Au nanoballs embedded in the substrate was identified with a mean diameter of 50.5 ± 8.0 nm (Fig. 3.5d), and a lattice expansion of around 22.6 % was obtained. Note that nanoballs produced by 100 keV Ar ion irradiation has a mean diameter of 33.9 ± 8.8 nm with a number density of around 27.9μm^{-2}. It is therefore concluded that the higher energy ion irradiation results in a sparser but larger nanoballs distributed on the SiO_2 glass substrate. In addition, the retained Au concentration under 150 keV Ar ion irradiation to a fluence of 1.0×10^{17} cm^{-2} is also given in Fig. 3.6, shown in red solid circle. It is obvious that the higher energy ion irradiation results in a larger Au concentration retained on the SiO_2 substrate, and the reason is the lower nuclear energy loss in the Au layer resulted in lower sputtering yield by higher energy ion irradiation.

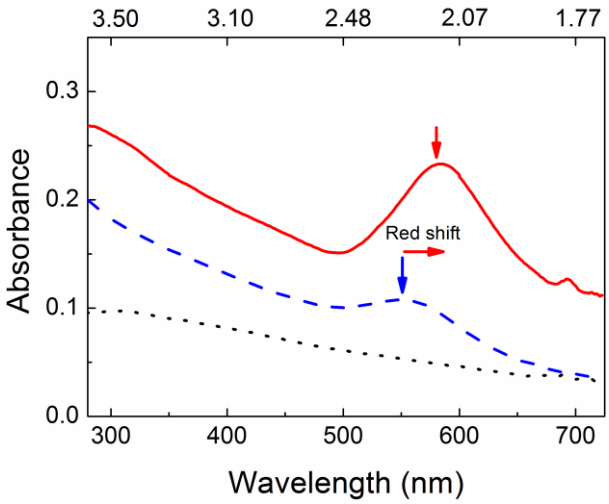

Fig. 3.7: Photoabsorbance spectra of the samples irradiated by Ar ions at 100 keV (dashed line) and 150 keV (solid line) to a fluence of 1.0×10^{17} cm^{-2}. The photoabsorbance spectra of the pure SiO_2 irradiated with 100 keV Ar ions to a fluence of 1.0×10^{17} cm^{-2} was also obtained (dotted line). The top scale represents the photo energy in eV.

Figure 3.7 shows the photo absorbance spectra of 100 keV (dashed line) and 150 keV (solid line) Ar ion irradiated samples to a fluence of $1.0 \times 10^{17}/cm^2$. Compared with the photo absorbance spectra for the 100 keV Ar ion irradiation of the pure SiO_2 to a fluence of 1.0×10^{17} cm^{-2} (dotted line), the absorbance band located around 550 nm corresponds to the surface plasmon resonance (SPR) peak possessed by Au nanoballs embedded in SiO_2 [14, 15], while the 150 keV irradiation resulted in a broadening peak with increased intensity. In general, the intensity and position of the SPR peak are closely related to the size and volume fraction of the nanoballs embedded in the dielectrics. As the irradiation energy of Ar ions increased from 100 keV to 150 keV, the average diameter of the Au nanoballs increased and the red shift of the SPR peak was observed.

This tendency of the experimental SPR peaks corresponds to those of the theoretical calculated SPR peaks using the code for electromagnetic scattering by spheres, in which Mie solution was applied to nanoballs with a unique size [15]. However, it is hard for nanoballs fabricated by ion irradiation to keep a unique size and pure chemical concentration because of ion–mixing, in which the existence of the Si in the Au nanoballs was observed. In the case of the sample after 100 keV Ar ion irradiation to 1.0×10^{17} cm^{-2}, the experimental SPR peak was 550 nm and the calculated SPR peak was 520 nm by using Jain's calculation [15]. On the other hand, the experimental SPR peak for the sample after 150 keV Ar ion irradiation was 590 nm and the calculated SPR peak was 550 nm. Jain's calculation was considered on the assumption of spherical Au nanoparticles with unique diameter dispersed in the solution homogenously. However, the red shift tendency of the SPR peak depending on the particle size was consistent.

3.4 Discussions

3.4.1 Radiation-enhanced dffusion and ion induced dewetting

As an ion impinges on a solid it begins a series of collision with both the electrons and the ion cores of target atoms. The collisions with electrons are more numerous owing to their larger number and cross section, but since their mass is small they do not much alter the trajectory of the incoming ion, nor do they usually result in atomic displacements. In most materials, therefore, these inelastic collisions can be treated simply by assuming that the electrons form a viscous background that extracts energy from the fast-moving ions and slows them down. At elevated temperatures the high concentrations of defects produced in the cascade can migrate throughout the material and begin to restore equilibrium. This induces the so-called radiation-enhanced diffusion. During irradiation at elevated temperature, the defect concentrations typically reach their steady states long before the phase transformations take place, and spatial variations in the steady-state concentrations often remain small, so that the defect concentrations are easily obtained. This behavior is very different from that arising from thermal diffusion.

It was discovered by Hu *et al* [2, 3] that for a thin metallic film on a dielectric substrate with a high interfacial energy, the pre-existing holes in the metallic film would grow during ion irradiation [3]. The growth of these holes was condidered due to the dewetting of the film. The film became discontinuous with further irradiation and eventually turned into a patterned structure of nanodots, with regular spacing between them. The thermodynamic reason for the dewetting of the metal film is the high interfacial energy and hence the continuous film is unstable on the substrate. Kinetically,

the occurrence of this process requires the mass transportation of the metal atoms, indicating that mobility of the metal atoms is significantly enhanced by ion irradiation.

3.4.2 Irradiation- enhanced viscous flow and ion induced embeddment

As observed in this Figure 3.3, the nanospheroids are partially embedded in the substrate, and the mechanism of the embedment has been studied in detail by Klimmer et al. It has been concluded that these nanospheroids are embedded by irradiation induced viscous flow, considering the effect of surface sputtering.

Klimmer *et al* and Hu *et al.* [12, 13] attributed the ion induced burrowing of nanoparticles to capillary forces acting on a solid particle on top of a viscous medium, where the viscosity η of the substrate is locally enhanced due to the ion bombardment. As discussed by Averback [16, 17], spike effects as well as point defect like entities may mediate the viscous flow in amorphous substrates. In both cases, however, the driving force for burying a solid spherical particle of radius *R* is thermodynamically related to its surface energy γ_p, to the surface energy of the viscous substrate γ_s, as well as to the corresponding interface energy $\gamma_{p,s}$. Hu et al. [12] parameterized the problem is by the two quantities

$$a = \frac{\gamma_s+\gamma_p-\gamma_{p,s}}{\gamma_s} = 1 + \cos\theta, \tag{3.2}$$

and

$$b = \frac{2\gamma_s}{3\eta}, \tag{3.3}$$

Equation 3.2 relates the surface and interface energies to the wetting angle between the viscous substrate and the solid particle. The wetting behavior as expected for various

values of the parameter a is sketched in Fig. 3.8b comprising all situation from complete dewetting for a=0 to complete wetting for a=2.

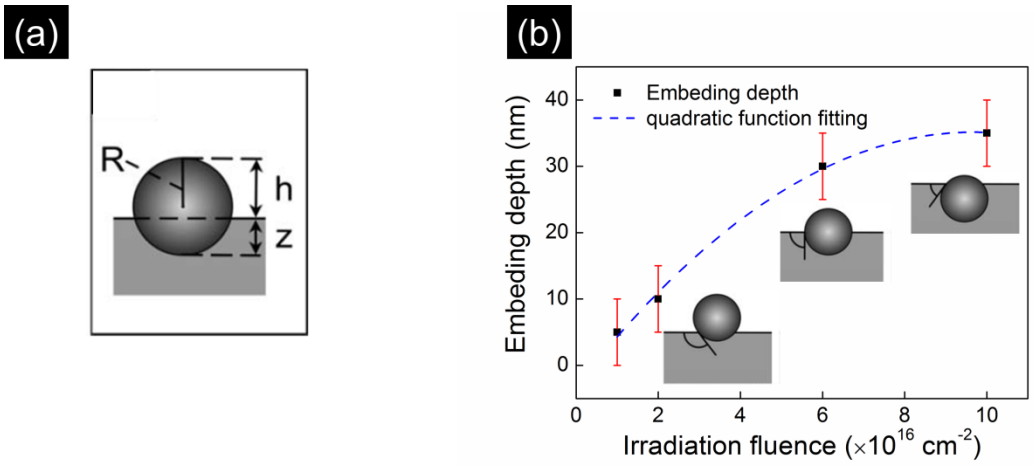

Fig. 3.8 (a) Definition of the two lengths z and h used in the theoretical description. The embedding depth obtained from bright field cross–sectional TEM images of Ag-Au bimetallic films as a function of irradiation fluence. Schematics of final equilibrium positions of solid spheres sinking into a viscous substrate depending on the wetting conditions is show in the Figure b.

The burrowing velocity is found to be

$$\frac{dz}{dt} = b\frac{(aR-z)}{z}, \tag{3.4}$$

and the standard viscosity η is substituted by an ion-induced viscosity η_r and scaled by the ion flux $d\phi/dt$,

$$\eta = \eta_r\left(\frac{d\phi}{dt}\right)^{-1}, \tag{3.5}$$

Therefore,

$$\frac{dz}{d\phi} = b'\frac{(aR-z)}{z}, \tag{3.6}$$

and

$$b' = \frac{2\gamma_s}{3\eta_r}, \tag{3.7}$$

a integrating of Eq. 3.6 yields:

$$\phi(z) = \frac{a}{b'} R ln \frac{aR}{aR-z} - \frac{z}{b'}, \tag{3.8}$$

We relate dose ϕ to embedment depth z by replacing viscosity with radiation-induced viscosity η_r. From these formulas, we can have a estimation of the radiation-induced viscosity η_r.

However, the conventional sputtering of nanoparticles leading to an ion induced continuously decreasing of the particle size [13]. It is reasonable to assume

$$2R(\phi) = h(\phi) + z(\phi), \tag{3.9}$$

and taking the decrease of the radius due to sputtering explicitly into account, thus, a additional part $2\,dR/d\phi$ is present in the expression of $dz/d\phi$, resulting in

$$\frac{dz}{d\phi} = b' \frac{(aR-z)}{z} + 2\frac{dR}{d\phi}, \tag{3.10}$$

It is reported that for a low ion–induced viscosity η_r substrate like sapphire, the burrowing effect can be neglected [13]. However, the near surface of the sapphire became amorphous after the extensive Ar–ion irradiation. Therefore, ion irradiation induced viscosity of the amorphous sapphire layer was sufficient enough to accomplish this burrowing process. As can be seen in the Chapter 5, where the Ar ion irradiation induced nanostructuring on single crystal alumina (sapphire) substrate was studied.

3.4.3 Optical properties of metallic nanostructures

A formal solution of rigorous scattering theory for nanoparticles is unfortunately only possible for restricted geometries. The *Mie* theory [18, 19] is an exact solution of the Maxwell equations for the scattering and absorption problem of spherical particles, and it is usually employed to derive approximate solutions for similar geometries.The extinction and scattering cross sections or the electromagnetic fields outside the spherical particle can be calculated:

$$\sigma_{ext} = \frac{2\pi}{k_M^2}\sum_{n=1}^{\infty}(2n+1)Re(a_n + b_n) \tag{3.11}$$

$$\sigma_{sca} = \frac{2\pi}{k_M^2}\sum_{n=1}^{\infty}(2n+1)(|a_n|^2 + |b_n|^2) \tag{3.12}$$

The scattering coefficients a_n and b_n are widely used, as show below:

$$a_n = \frac{\psi_n(x)\psi_n'(mx) - m\psi_n'(x)\psi_n(mx)}{\xi_n(x)\psi_n'(mx) - m\xi_n'(x)\psi_n(mx)}, \tag{3.13}$$

$$b_n = \frac{m\psi_n(x)\psi_n'(mx) - \psi_n'(x)\psi_n(mx)}{m\xi_n(x)\psi_n'(mx) - \xi_n'(x)\psi_n(mx)}, \tag{3.14}$$

where $\psi_n(x) = xj_n(x)$, $\chi_n(x) = x\gamma_n(x)$ and $\xi_n(x) = xh_n^{(1)}(x)$ are Riccati–Bessel, Riccati–Neumann and Riccati–Hankel functions, respectively. A notable property of the scattering coefficients a_n and b_n is that their denominator can become very small. The minima are complex-numbered poles. At these poles the corresponding partial wave exhibits a resonance with different magnitudes for the scattered fields due to the different numerator. The resonances caused by bound electrons are denoted *electronic resonances* and the resonances by free electrons are denoted *surface plasmon polaritons*. A pronounced SPP resonance can be found for aluminum, alkali

metal, and noble metal nanoparticles. An example is given in Figure 3.9 for Ag, Au, and Cu nanospheres with 2R=30 nm.

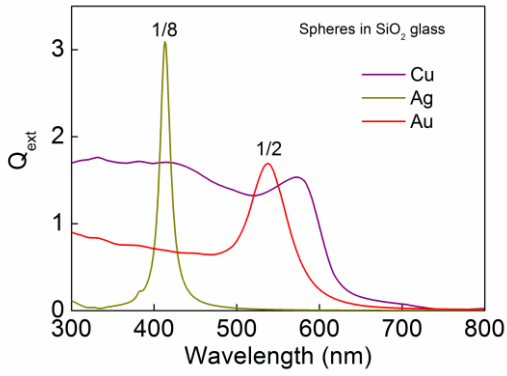

Fig. 3.9 Computed extinction efficiencies Q_{ext} for non-interacting gold spherical particles with 2R = 30 nm dispersed in a homogeneous dielectric host (ε_h = 2.25), showing an SPP.

The noble metals show pronounced features, since the contribution χ_{IB} of interband transitions from the $3d$ (Cu), $4d$ (Ag), or $4d$ (Au) electrons to the hybridized $4sp$ (Cu), $5sp$ (Ag), or $6sp$ (Au) band has an enormous influence on the positions of the plasmon polaritons. The SPP resonances in noble metal nanoparticles therefore cannot be regarded as free electron resonances even at a rough approximation; rather, they are hybrid resonances resulting from cooperative behavior of both the d electrons and the conduction electrons. This is demonstrated in Figure 3.9 by representative spectra for Cu, Ag, and Au nanoparticles, calculated by Mieplot [20]. For Au nanoparticles, the influence of the interband transitions can also be clearly recognized, but is already strongly reduced because they are more separated from the resonance position of the SPP. The modest influence of the interband transitions on the SPP is obtained for Ag nanoparticles. Although the interband transitions contribute to the spectra at shorter wavelengths, the peak position of the SPP is well separated from the interband

transitions, so a sharp resonance is obtained. So far, Ag behaves very similarly to the Drude metals. The resonant structures in the extinction lead to characteristic colors for the smaller particles: red for Cu and Au and yellow for Ag.

We present the calculated spectra for the extinction efficiencies Q_{ext}, defined as the sum of the absorption and scattering cross-sections renormalized by the geometrical cross-sections πa_γ^2, as a function of the wavelength:

$$Q_{ext,\gamma} = (\sigma_{abs,\gamma} + \sigma_{sca,\gamma})/\pi a_\gamma^2 \tag{3.15}$$

Influence of the particle size

In Fig. 3.10a the extinction spectra, calculated employing the Mie theory, are reported for spherical particles with diameters between 10 nm and 150 nm; the corresponding peak positions and linewidths are highlighted in Fig. 3.10b. We can see that increasing the diameter d the resonances are systematically red shifted with their linewidth monotonically increases. These trends are mainly due to surface damping and retardation effects. For small particles, the former is dominant, so the LSP position is slightly affected by the size. At larger size, dynamic depolarization and radiation damping rapidly grow, inducing a strong red shift and broadening of the peaks, and reducing their intensity. Higher order surface plasmon resonances for multipole order $n > 1$ can be observed for larger nanoparticles. The total extinction reveals a complex multipeak structure, which results from the various multipole contributions of SPPs to the absorption and scattering.

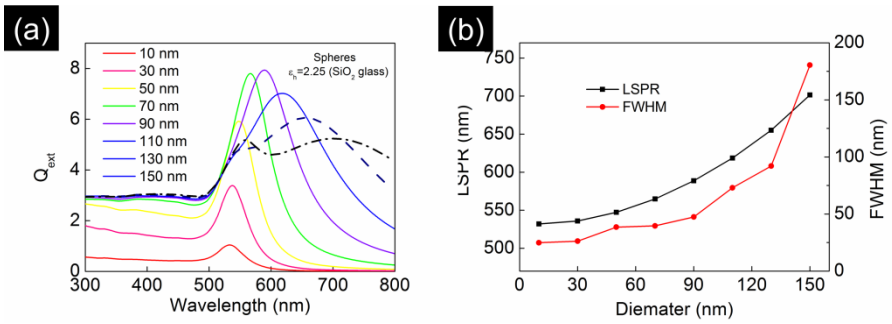

Fig. 3.10 (a) Computed extinction efficiencies Q_{ext} for non-interacting gold spherical particles, having different radii, dispersed in a homogeneous dielectric host ($\varepsilon_h = 2.25$). (b) position (λ_{max}, red line) and full width at half maximum (FWHM, black curve) of the LSP peaks in panel (a) as a function of the particle radius.

Influence of the environment

We start by considering spherical particles of radius $d = 30\,nm$, and analyse the effects of a variation of the host dielectric constant ε_h. Since the particles are immersed in a dense medium, the local electric field differs from the external excitation due to the polarization of the medium. In Fig. 3.11 we report the calculated curves for Q_{ext} with ε_h varying from 1 (vacuum) up to 3, computed with Mieplot. We can see that the position of the resonance moves to larger wavelengths (lower energies) at higher ε_h and correspondingly its magnitude increases. Employing the Fröhlich condition and looking at ε_m, we can deduce that the resonance red-shift is due to the negative slope of the real part of ε_m; the enhancement of the resonances is instead related to the proportionality between the induced dipole and ε_h.

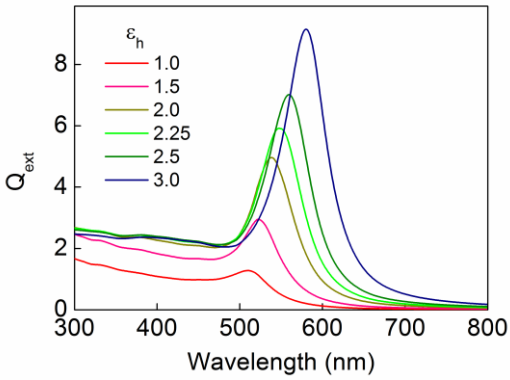

Fig. 3.11 Computed extinction efficiencies Q_{ext} for non-interacting gold spherical particles, of diameter $d = 30\ nm$, as a function of the dielectric constant ε_h of the host.

As we can see, as increasing the diameter d the resonances are systematically red shifted, which is in good agreement with the experiment results. In addition, even the slightest change in the dielectric surrounding leads to a detectable shift of the resonance energy. That is the reason why metallic nanoparticles are very suitable for surface enhanced Raman spectroscopy: placing a molecule in the vicinity of a nanoparticle effects the dielectric environment and therefore there is the enhanced photo emission.

As we can see, the nanoparticles optical properties are strongly depends on their size, shape, sorrouding environment and the chemical component, the experimental focused on the optical response control were described in the following two chapters (chapter 4 and chapter 5).

3.5 Conclusions

In this study, to study the process of ion irradiation induced surface nanostructuring of Au film deposited on SiO_2 glass substrate and its optical properties, the surface morphology was examined using an AFM and a SEM, and the microstructural evolution and the chemical concentration of Au films were investigated using a TEM equipped with an energy dispersive spectrometer. The following conclusions were obtained;

1. With the irradiation fluence increased from 1.0×10^{16} cm^{-2} to 1.0×10^{17} cm^{-2}, the dewetting of the Au films on the SiO_2 glass substrate was occurred and the Au nanoscale islands were formed on the substrate. Finally a single layer of photosensitive gold nanoballs with highly spherical shape embedded in a SiO_2 substrate was obtained.

2. The lattice expansion was observed as increasing irradiation fluence. These lattice expansions could be caused by irradiation induced lattice defects and the irradiation induced interface ion–mixing. However, the Au nanoparticles and the Au nanoballs in this study showed FCC structure instead of the hexagonal metastable phase in the previous study. Half amounts of the Au nanoballs were also found to be single crystals.

3. As increasing the irradiation energy from 100 to 150 keV, the average diameter of the Au nanoballs increased and a red shift of the SPR peak was observed. Ion beam induced nanostructuring method could be useful in controlling the SPR properties of the Au film deposited on SiO_2 glass substrate.

4 Ion Beam Surface Nanostructuring of Ag-Au Bimetallic Films on SiO_2 Glass

4.1 Introduction

There has been a great deal of research conducted on controlling the morphology and composition of these nanoparticles. The synergistic control of various parameters sensitive to the LSPR band includes both particle size and shape. Further control of LSPR frequency over a wider range has been achieved by synthesizing bimetallic nanoparticles fabricated in the form of alloys of two metals. In general, the resulting LSPR frequency lies in between that of the pure components, and depends on the relative amounts of the two components. In particular, Ag–Au nanocomposites have attracted increasing interest because of their composition–dependent tunable optical properties and because complete miscibility of Au and Ag can be obtained at any composition in both bulk materials and NPs.

In chapter 3, we have described the synthesizing of photosensitive gold nanoparticles partially embedded in SiO_2 glass substrates. In this study, the synthesis method of Ag–Au alloy nanospheroids in SiO_2 glass substrate by ion irradiation was described with its tunable optical properties. In this method, the synthesized nanoparticles with advanced functionalization surface partially embedded in the dielectric matrix were obtained.

4.2 Experimental Details

Ar–ion irradiation induced surface nanostructuring of Ag–Au bimetallics with various molar ratios deposited on SiO_2 substrate was performed, and tunable plasmon resonance frequency was obtained. The Ag–Au bimetallic thin films were thermally evaporated on mirror polished SiO_2 substrates at ambient temperature by electrically heating the Ag and Au sources under a 6.0×10^{-5} Torr vacuum. In general, the Ag nanostructures are unstable and easily get oxidized [1-3] Therefore, the as–deposited samples were kept in the vacuum condition. However, a strong increase in the oxidation resistance was observed with the increase of Au atomic fraction inside the nanostructures [3], and it is reported that most of the Au–Ag nanostructures was not oxidized at gold fractions above 0.4 in solution [4]. Therefore, the Au–Ag bimetallic films on SiO_2 substrates were thought to be stable in this study. The film thickness was verified to be 30 nm by transmission electron microscope (TEM; JEOL JEM–2010F), and a field–emission scanning electron microscope (SEM; JEOL JSM–7001FA) equipped with energy dispersive spectrometer (EDS; Noran Thermo Fischer Scientific) was used for measuring the compositions of the as–deposited and irradiated samples.

For the 30 nm $Ag_{(50\%)}$–$Au_{(50\%)}$ bimetallic films deposited on the SiO_2 substrates, the optical micrograph exhibits a blue color (Fig. 4.1a, upper section) and the surface is uniformly smooth and consists of planar grains as small as a few nanometers in size (SEM micrograph in Fig. 4.1a, lower section). 100 keV Ar ions irradiation at ambient temperature with fluences of 4.0×10^{16} cm^{-2}, 5.5×10^{16} cm^{-2}, 7.0×10^{16} cm^{-2}, 1.0×10^{17} cm^{-2}, and 1.4×10^{17} cm^{-2} were performed to study the fluence dependence. The energies of the ions were chosen such that the range is wider than the thickness of the

bimetallic layer, as calculated by the SRIM 2011 code [5]. Ar–ion irradiation on the samples was performed using the 400 keV ion accelerator at the HVEM laboratory, Hokkaido University. A low pressure of 10^{-3} Pa was maintained inside the irradiation chamber. To ensure uniform irradiation, Ar–ion beam was scanned and the current was maintained at approximately 2.0 μA cm^{-2}. Furthermore, on top of the SiO_2 samples, pure silver, pure gold, and three different bimetallic Ag–Au films with molar ratios of 0.25:0.75, 0.5:0.5, and 0.75:0.25 were deposited to investigate the component dependence, and consequent Ar–ion irradiation of these bimetallic films were also performed to a fluence of 1.0×10^{17} cm^{-2}. For the as–deposited samples, the color changed from blue to yellow green (upper sections of Fig. 4.5a–e) and the surface remained uniformly smooth (lower section of Fig. 4.5a –e).

As the radiation induced defects can be removed by annealing at temperatures higher than 623 K [6], post–irradiation thermal annealing is usually employed to anneal ion irradiated samples. Therefore, thermal annealing was conducted *ex–situ* under high vacuum (4.25×10^{-5} Pa) at 773 K for two hours. After that, optical absorption spectra were recorded over a wavelength range of 300–800 nm on a spectrophotometer (JASCO V–630) with a spectral bandwidth of 1.5 nm, and the SEM observations were used to examine the surface modification. The line and surface element concentration were evaluated at the nanoscale using the SEM coupled with an EDS, and the line chemical concentration profiles cross the surface were obtained using the SEM operated at 6.0 keV. Moreover, microstructural characterization was performed using the TEM operated at 200 keV. The cross–sectional TEM samples were prepared using a precision ion polishing system (PIPS; JEOL AT–12310).

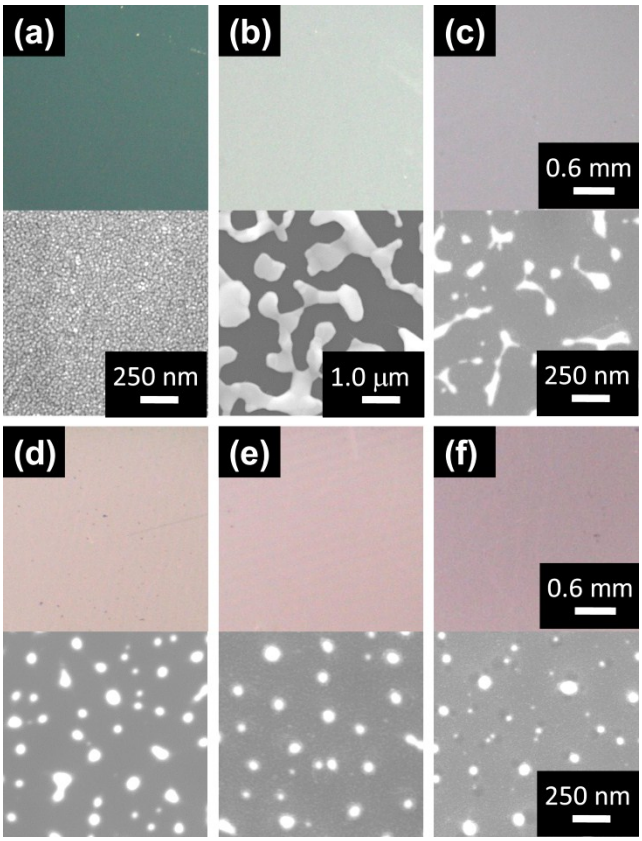

Fig. 4.1: Optical micrographs (upper sections of each panel) and SEM micrographs (lower sections of each panel) of (a) $Ag_{50\%}$–$Au_{50\%}$ as–deposited SiO_2, (b) thermally annealed sample, and post–irradiation annealed samples with irradiation fluences of (c) 4.0×10^{16} cm^{-2}, (d) 7.0×10^{16} cm^{-2}, (e) 1.0×10^{17} cm^{-2}, and (f) 1.4×10^{17} cm^{-2}.

4.3 Results

4.3.1 Fluence effect on surface nanostructuring by ion irradiation

The morphology of the surface nanostructuring by ion irradiation on the dielectric substrate depends on variations in the irradiation parameters such as fluence, current and beam energy. In this study, fluence dependence on the ion induced surface nanostructure was studied using 100 keV Ar–ion irradiation of 30 nm $Ag_{(50\%)}$–$Au_{(50\%)}$ bimetallic films deposited on SiO_2 substrates with the irradiation fluence increasing from 4.0×10^{16} cm^{-2} to 1.4×10^{17} cm^{-2}. A color change from dark green to light violet was observed, as can be observed in the optical micrographs in the upper sections of Fig. 4.1. SEM was used to study the surface nanostructure after the post–irradiation thermal annealing. The lower sections of each panel in Figure 4.2 shows SEM micrographs of (a) as–deposited $Ag_{(50\%)}$–$Au_{(50\%)}/SiO_2$, (b) annealed sample, and post–irradiation annealed samples with irradiation fluences of (c) 4.0×10^{16} cm^{-2}, (d) 7.0×10^{16} cm^{-2}, (e) 1.0×10^{17} cm^{-2}, and (f) 1.4×10^{17} cm^{-2}. For the specimen irradiated at the lowest fluence (4.0×10^{16} cm^{-2}), the line profiles of the chemical concentration across the surface were obtained (Fig. 4.2).

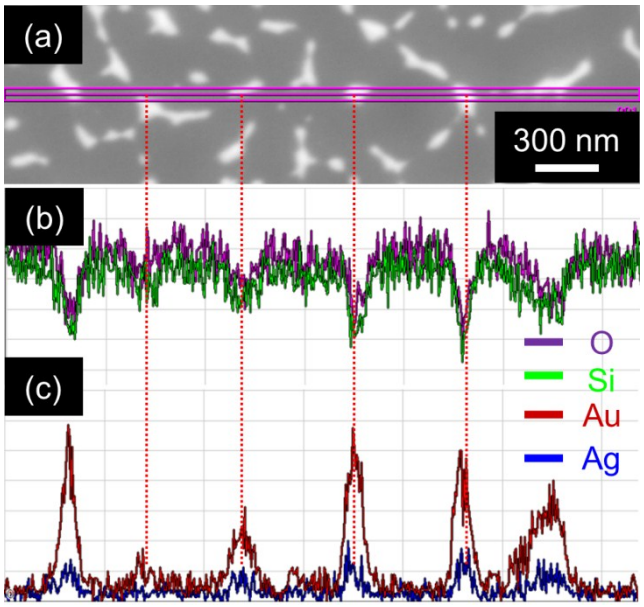

Fig. 4.2: (a) Typical SEM micrograph of post–irradiation annealed sample of $Ag_{50\%}$–$Au_{50\%}$ bimetallic film on SiO_2 at a fluence of $4.0 \times 10^{16}/cm^2$; (b) line profiles of silica and oxygen along the horizontal line indicated in (a); (c) line profiles of silver and gold along the horizontal line indicated in (a).

Figure 4.2a shows the typical SEM image, and the red line indicates the line along which the element concentration was determined. Fig. 4.2b shows the line profile of silica and oxygen concentrations. Fig. 4.2c shows the line profile of silver and gold concentrations with the Ag peaks appearing in the same place as the Au peaks; both peaks occur at troughs in the silica and oxygen profiles, and the peaks in the concentration profiles correspond to the bright areas shown in Fig. 4.2a, indicating that silver and gold alloyed at the nanoscale. Therefore, the bright contrast areas in the SEM micrographs represent the retained bimetallic films on the substrates.

While the surface of the as–deposited SiO_2 substrate is smooth with fine particles a few nanometers in size (lower section of Fig. 4.1a), relatively large polygonal pitches with a

Heywood diameter greater than 900 nm were observed (lower section of Fig. 4.1b) after thermal annealing because of the thermal induced homogeneous nucleation [7, 8]. As–deposited SiO_2 is quite different from the ion irradiated samples. With increasing irradiation fluence, the process of bimetallic film evolution under Ar–ion irradiation is clearly observed, with the formation of isolated photosensitive nanospheroids. Partially connected nanoscale islands formed after irradiation to a fluence of 4.0×10^{16} cm^{-2} because of ion induced dewetting of thin metallic films [9]. When the fluence increased to 7.0×10^{16} cm^{-2}, elongated nanospheroids were obtained on the substrate. A detailed study of the $Ag_{(50\%)}$–$Au_{(50\%)}$ bimetallic nanospheroids was conducted by measuring the nanospheroids diameter and aspect ratio, and the results are summarized in Table 4.1.

Table 4.1: Statistical analysis of morphology and optical properties for post–irradiation thermal annealed $Ag_{(50\%)}$–$Au_{(50\%)}/SiO_2$ at various fluences.

Fluence ($\times 10^{16}$ cm^{-2})	d[a] (nm)	Aspect ratio[b]	LSPR[c] (nm)	LSPR[d] (nm)
4.0	64.3 ± 27.4	1.94 ± 0.79	565.0 ± 3.0	587
5.5	56.5 ± 25.5	1.67 ± 0.69	526.0 ± 0.5	552
7.0	50.4 ± 19.5	1.37 ± 0.47	500.0 ± 0.4	511
10.0	50.3 ± 19.5	1.24 ± 0.28	498.2 ± 0.4	494
14.0	46.1 ± 18.8	1.15 ± 0.17	522.0 ± 0.3	483

[a] d is the mean diameter of $Ag_{(50\%)}$–$Au_{(50\%)}$ bimetallic nanospheroids;

[b] Aspect ratio is the mean aspect ratio of $Ag_{(50\%)}$–$Au_{(50\%)}$ bimetallic nanospheroids;

[c] LSPR is the measured maximum absorption of the LSPR band of $Ag_{(50\%)}$–$Au_{(50\%)}$ bimetallic nanospheroids;

[d] LSPR is the calculated maximum absorption of the LSPR band of $Ag_{(50\%)}$–$Au_{(50\%)}$ bimetallic nanospheroids.

Figure 4.4a illustrates the mean diameter and aspect ratio of the $Ag_{(50\%)}$–$Au_{(50\%)}$ nanospheroids as a function of irradiation fluence. Both show a systematic decrease

with the irradiation fluence, and their deviations also decrease with the irradiation fluence. Bright field cross–sectional TEM micrograph of these nanospheroids were obtained (Fig. 4.3a), and the diffraction pattern for a typical nanospheroid is given in Fig. 4.3b showing a FCC structure. As observed in this figure, the nanospheroids are partially embedded in the substrate, and the mechanism of the embedment has been studied in detail by Hu et al [10]. It has been concluded that these nanospheroids are embedded by irradiation induced viscous flow, considering the effect of surface sputtering [11].

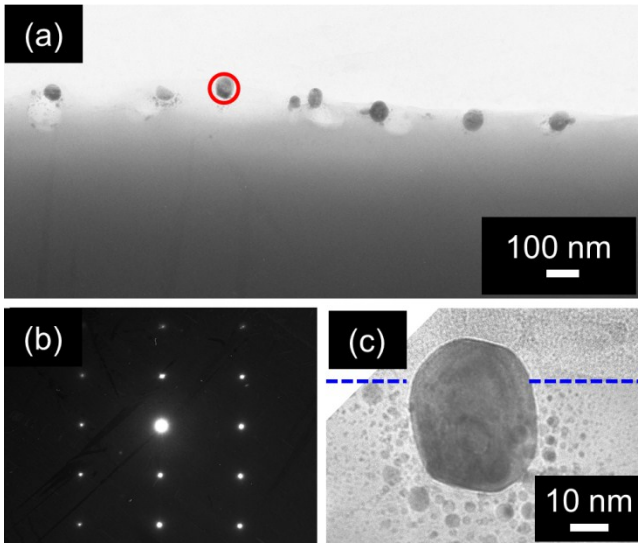

Fig. 4.3: (a) Typical bright field cross–sectional TEM micrograph of $Ag_{(50\%)}$–$Au_{(50\%)}$ bimetallic nanospheroids partially embedded in SiO_2 substrate fabricated by post–irradiation annealing of $Ag_{(50\%)}$–$Au_{(50\%)}/SiO_2$ irradiated to a fluence of 1.0×10^{17} cm^{-2}; (b) diffraction pattern for a typical $Ag_{(50\%)}$–$Au_{(50\%)}$ bimetallic nanospheroid circled in (a); (c) High resolution TEM micrograph for a typical $Ag_{(50\%)}$–$Au_{(50\%)}$ bimetallic nanospheroid circled in (a) with the dashed bule line indicating the interface between SiO_2 substrate and vacancy.

Optical absorption spectra were recorded for each specimen after irradiation. Figure

4.4b shows the absorption spectra of the samples irradiated at fluences ranging from 4.0×10^{16} cm^{-2} to 1.4×10^{17} cm^{-2}. For the specimen irradiated at a fluence of 4.0×10^{16} cm^{-2}, a broad absorption peak was observed, while narrower absorption peaks were clearly observed for specimens irradiated at fluences exceeding 7.0×10^{16} cm^{-2}. These absorption peaks were induced by the resonance of the incident light with the combined oscillation of the free electrons aggregated at the surface of these $Ag_{(50\%)}$–$Au_{(50\%)}$ bimetallic nanospheroids partially embedded in the SiO_2 substrate. This enhanced absorption is a characteristic of LSPR, and the peak positions are summarized in Table I. These absorbance bands correspond to the LSPR peak exhibited by Ag–Au bimetallic nanospheroids sustaied on or embedded in a SiO_2 matrix [12, 13]. As the irradiation fluence of the Ar ions increased, a shift of the LSPR peak positions toward the short wavelength was observed up to an irradiation fluence of 1.0×10^{17} cm^{-2}, and then shifted towards the longer wavelength on further increase of the fluence (Fig. 4.4c).

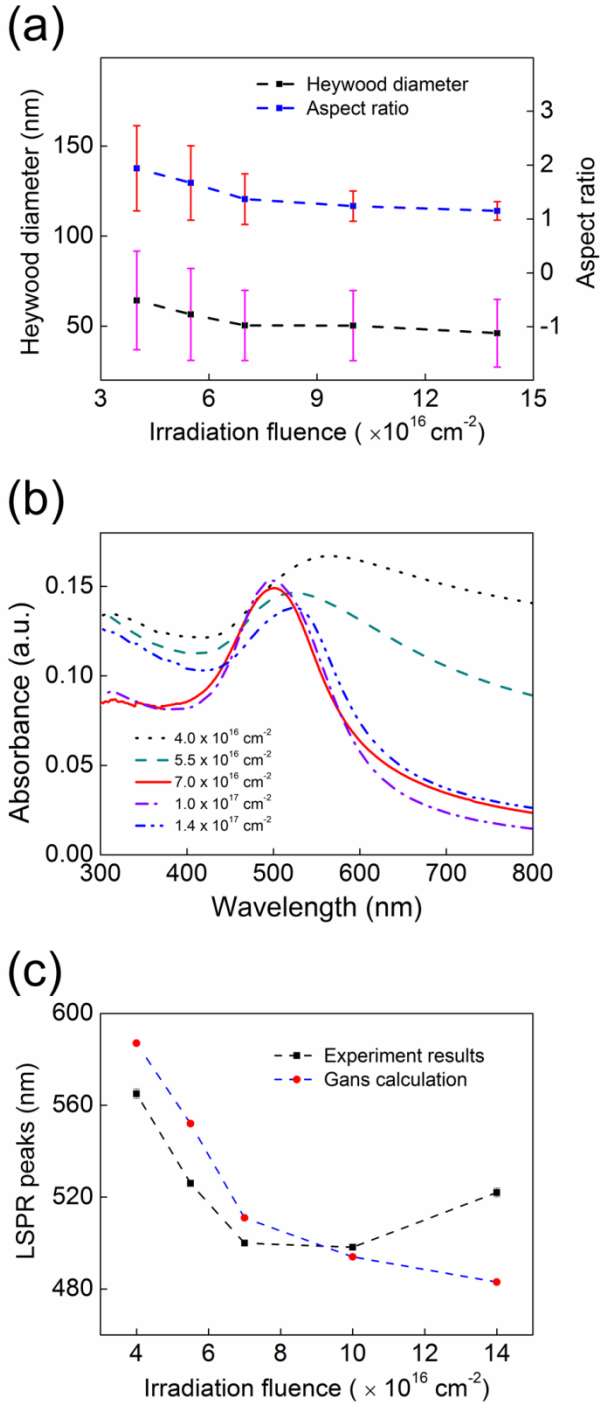

Fig. 4.4: (a) Heywood diameters and aspect ratios of the nanospheroids plotted against the irradiation fluence; (b) photoabsorbance spectra of the samples after post–irradiation thermal annealing; and (c) experimentally measured and Gans calculation of the maximum absorption wavelength position plotted against irradiation fluence.

4.3.2 Ag–Au nanospheroids with tunable surface plasmon resonance frequency

Bimetallic nanospheroids with various Au–Ag molar ratios (0.0:1.0, 0.25:0.75, 0.5:0.5, 0.75:0.25, 1.0:0.0) were synthesized using Ar–ion irradiation of Au–Ag bimetallic films deposited on SiO_2 substrates. A color change from light yellow to violet was observed by optical microscope for the five samples (upper sections of Fig. 4.5a'–e'). SEM was used to study the surface nanostructuring after post–irradiation thermal annealing. SEM micrographs (lower sections of Fig. 4.5a'–e') shows the surface morphology of the post–irradiation annealed samples of pure silver, $Ag_{(75\%)}$–$Au_{(25\%)}$, $Ag_{(50\%)}$–$Au_{(50\%)}$, $Ag_{(25\%)}$–$Au_{(75\%)}$, and pure gold deposited on SiO_2 substrates. A detailed study of the $Ag_{(X\%)}$–$Au_{(100\text{-}X\%)}$ bimetallic nanospheroids was conducted by measuring the nanospheroids diameter and aspect ratio, and the results are summarized in Table 4.2. Figure 4.6a illustrates the mean diameter and aspect ratio of the Ag–Au nanospheroids as a function of Au concentration, which shows the formation of nanospheroids with comparable size and aspect ratio for the five samples.

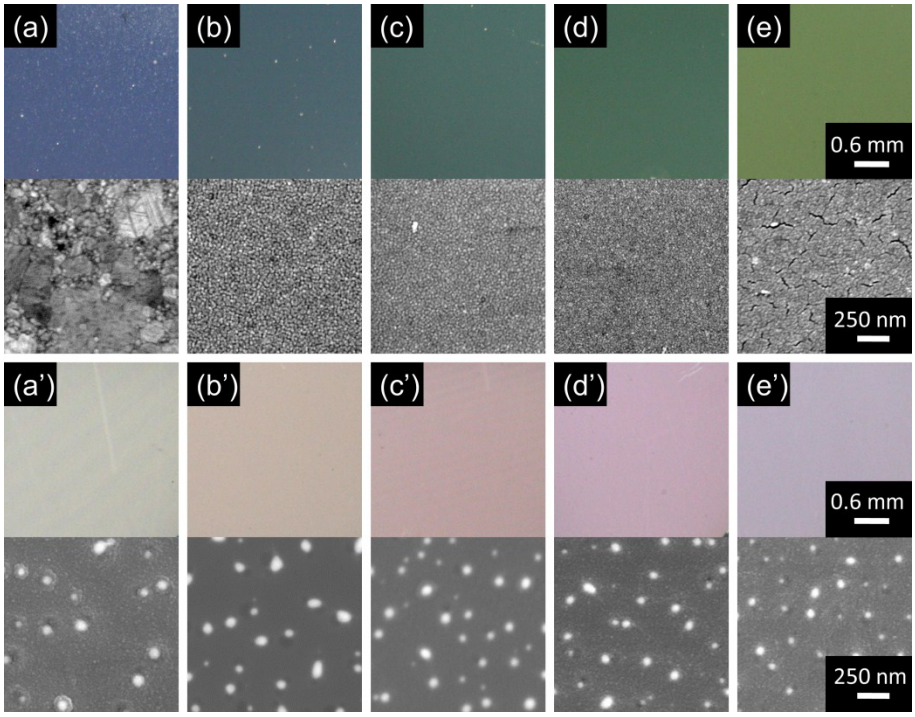

Fig. 4.5: Optical micrographs (upper section of each panel) and SEM micrographs (lower section of each panel) of (a) pure silver, (b) $Ag_{(75\%)}$–$Au_{(25\%)}$, (c) $Ag_{(50\%)}$–$Au_{(50\%)}$, (d) $Ag_{(25\%)}$–$Au_{(75\%)}$, and (e) pure gold as–deposited on SiO_2. Figure 4.5a'–e' are optical micrographs and SEM micrograph of these five samples after post–irradiation thermal annealing.

Optical absorption spectra were recorded for each specimen after post–irradiation annealing. Figure 4.6b shows the tunable characteristics of LSPR frequency of Ag–Au bimetallic nanospheroids of all five samples, and a single localized surface plasmon absorption band for each sample was observed. Figure 4.6c shows the UV–Vis absorption peak position plotted against the percentage of Au concentrations. This figure demonstrates that the LSPR peak positions shift approximately linearly from 424.5 nm (Ag nanospheroids) to 566.6 nm (Au nanospheroids) with an increase in Au molar fractions. The wavelength of the maximum absorption band for each sample is summarized in Table 4.2. In this study, the nanospheroids were synthesized in the

vacuum chamber. However, *ex–situ* photoabsorption spectra measurement was carried out in air. Therefore, a layer of oxide Ag (usually Ag_2O) was formed on the nanospheriods surface, and the Ag–core Ag–oxide shell structure will induce a red shift of the characteristic surface plasmon resonance response for pure Ag, which located at around 400 nm [1, 2]. However, this plasmon absorption peak was rather stable over time: after 8 months in a low vacuum condition, the plasmon absorption intensity has decreased a little (Figure 4.7).

Table 4.2: Statistical analysis of morphology and optical properties for post–irradiation thermal annealed $Ag_{(X\%)}$–$Au_{(100-X\%)}/SiO_2$ at a fluence of 1.0×10^{17} cm^{-2}.

Samples	d[a]	Aspect ratio[b]	LSPR[c] (nm)	LSPR[d] (nm)
Ag/SiO_2	48.3 ± 20.0	1.24 ± 0.33	424.5 ± 2.5	452
$Ag_{(75\%)}$–$Au_{(25\%)}/SiO_2$	51.7 ± 19.1	1.20 ± 0.20	486.3 ± 0.2	473
$Ag_{(50\%)}$–$Au_{(50\%)}/SiO_2$	50.3 ± 19.5	1.24 ± 0.28	498.2 ± 0.4	494
$Ag_{(25\%)}$–$Au_{(75\%)}/SiO_2$	45.2 ± 19.5	1.33 ± 0.43	538.5 ± 0.2	522
Au/SiO_2	37.5 ± 15.0	1.18 ± 0.19	566.6 ± 0.4	521

[a] d is the mean diameter of $Ag_{(X\%)}$–$Au_{(100-X\%)}$ bimetallic nanospheroids;

[b] Aspect ratio is the mean aspect ratio of $Ag_{(X\%)}$–$Au_{(100-X\%)}$ bimetallic nanospheroids;

[c] LSPR is the measured maximum absorption of the LSPR band of $Ag_{(X\%)}$–$Au_{(100-X\%)}$ bimetallic nanospheroids;

[d] LSPR is the calculated maximum absorption of the LSPR band of $Ag_{(X\%)}$–$Au_{(100-X\%)}$ bimetallic nanospheroids.

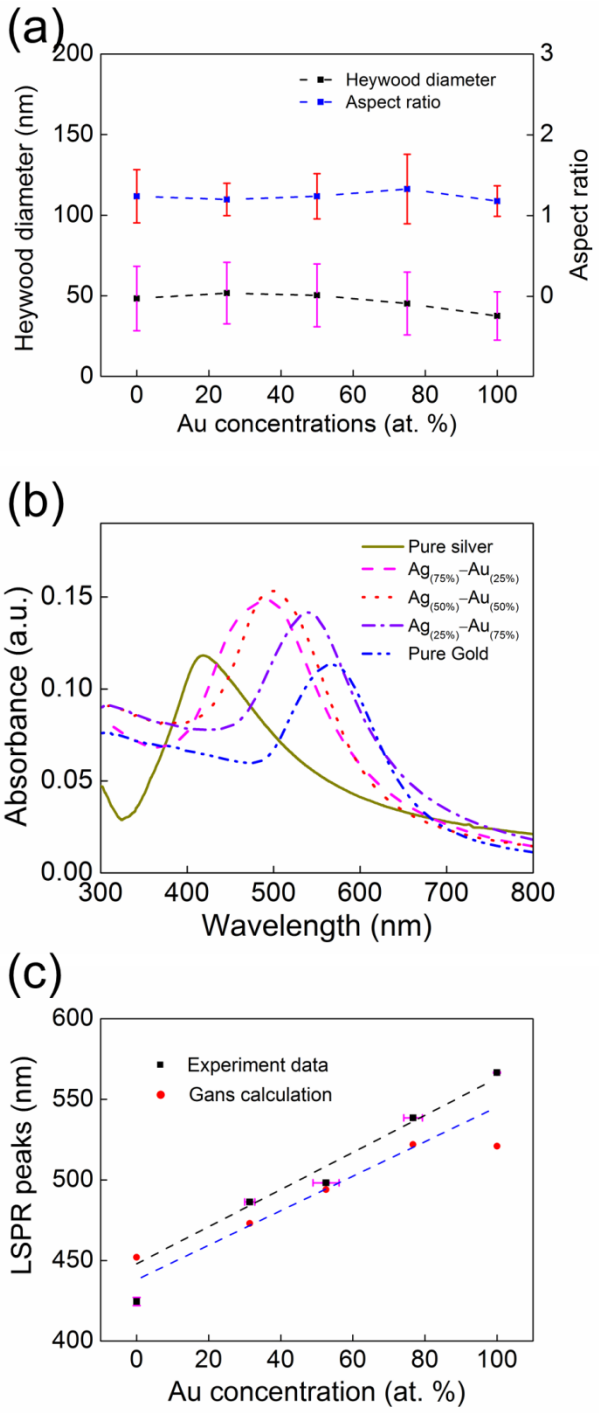

Fig. 4.6: (a) Heywood diameters and aspect ratios of the $Ag_{(X\%)}$–$Au_{(100-X\%)}/SiO_2$ nanospheroids plotted against the Au concentration; (b) photoabsorbance spectra of the samples after post–irradiation thermal annealing; and (c) experimentally measured and Gans calculation of the

maximum absorption wavelength position plotted against the Au concentration, and the dashed lines are used for guiding the eyes only.

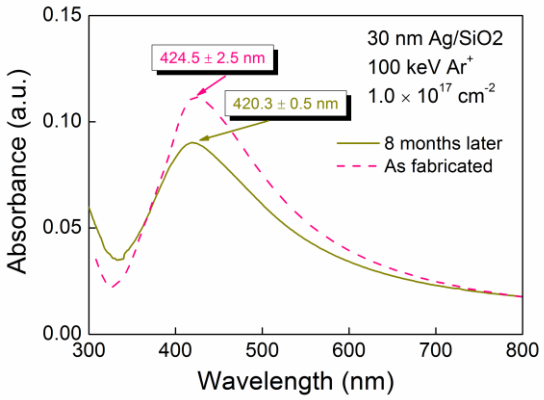

Fig. 4.7 Photoabsorbance spectra of the sample (Ag(30nm)/SiO_2) after 100 keV Ar ion irradiation at a fluence of 1.0×10^{17} cm^{-2} (pink dashed line); and (b) photoabsorbance spectra of the same sample taken 8 months later kept in vacuum box (dark yellow solid line).

4.4 Discussions

4.4.1 Optical Properties of Ellipsoids

For particles whose size is small compared to local variations of the incident light, the phase of the EM fields varies very little over the particles volume and we can assume uniform and non-retarded fields: this is called the *quasi-static approximation* (QSA) [14, 15]. For common metals, like Ag, Au, Cu, Al, which have the LSP resonances in the visible and UV range, this approximation can adequately describe the optical response of spherical and ellipsoidal particles with sizes below $100\ nm$. Treating the ellipsoidal particle in the Rayleigh approximation as done by Gans [16], we can restrict considerations to excitation of a dipole moment in the particle. Let's consider a metallic ellipsoidal particle immersed in a transparent dielectric host and far from any other polarizable entity (Fig. 4.8).

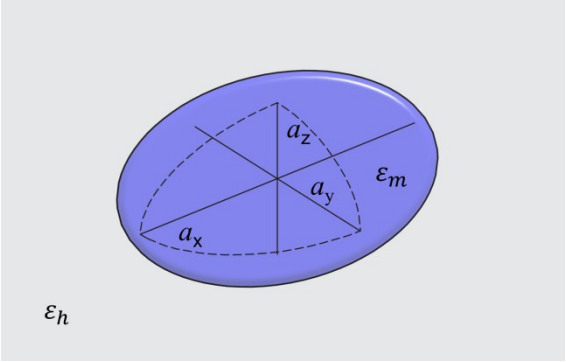

Fig. 4.8 Sketch of an isolated metallic ellipsoidal particle, with principal semiaxis (a_x, a_y, a_z) and dielectric function ε_m, immersed in a dielectric host of dielectric constant ε_h.

In general, the optical property of nanoparticles is characterized by photoabsorbance. The photoabsorbance A is proportional to the extinction cross–section σ_{ext}, which can be obtained by the Mie scattering theory [15]. However, Mie theory is only applicable

to spherical particles. Richard Gans generalized Mie's results to spheroidal particles of any aspect ratio in the small particle approximation [16]. In the case of a single uncharged spheroidal particle with dielectric function $\varepsilon = \varepsilon_1 + i\varepsilon_2$ dispersed in a surrounding medium with dielectric function ε_m. The general expression of the extinction cross–section takes the following form:

$$\sigma_{\text{ext}} = \frac{2\pi\varepsilon_m^{3/2}V}{3\lambda}\sum_{j=1}^{3}\frac{\left(1/P_j^2\right)\varepsilon_2}{\{\varepsilon_1+[(1-P_j)/P_j]\varepsilon_m\}^2+\varepsilon_2^2}\ , \tag{4.1}$$

where λ the incident light wavelength, V the particle volume, and $\varepsilon = \varepsilon_1 + i\varepsilon_2$ the size–dependent complex dielectric function of the particle.

Equation (1) is valid if the particle size is much smaller compared to the light wavelength λ. Here, P_j includes P_A, P_B, and P_C termed depolarization factors, for each axis of the particle. In our study, $\mathrm{A} > \mathrm{B} = \mathrm{C}$ is assumed for a prolate spheroid. The depolarization factors anisotropically alter the values of ε_1 and ε_2, and therefore the resulting LSPR peak frequencies. The depolarization factors are given as follows:

$$P_A = \frac{1-e^2}{e^2}\left[\frac{1}{2e}\ln\left(\frac{1+e}{1-e}\right)-1\right], \tag{4.2a}$$

$$P_B = P_C = (1-P_A)/2, \tag{4.2b}$$

where e is the following factor, which includes the particle aspect ratio R:

$$e = [1-(B/A)^2]^{1/2} = (1-1/R^2)^{1/2}, \tag{4.3}$$

The LSPR absorption holds when the denominator in Eq. 1 exhibits a minimum, that is:

$$\varepsilon_1 = -\left[\left(1-P_j\right)/P_j\right]\varepsilon_m\ , \tag{4.4}$$

In particular for noble–metal NPs the equation has a solution in the visible range at the

LSPR frequency, because the real part of the dielectric function is negative. The extinction spectrum from Eq. 1 has two peaks, one corresponding to the transverse plasmon mode and the other corresponding to the longitudinal plasmon mode. Equation 1 provides an intuitive understanding of the effects of aspect ratio on the LSPR peak wavelength. The factor $(1 - P_j)/P_j$ increases with aspect ratio and can be greater than 2, leading to a shift of the LSPR peak towards the longer wavelength. For nanoparticles other than these spheres and spheroids, particle shape plays a significant role on the LSPR spectra. However, this cannot be determined by analytical analysis, and must be studied numerically. Numerical methods for plasmonic nanoparticles include the generalized multisphere Mie (GMM) theory [17], and the discrete dipole approximation (DDA) [18], and the Finite-Difference Time-Domain (FDTD) method [19].

An extension of Gans theory for the calculation of optical absorption spectra in bimetallic nanoparticles has been developed. While dealing with the optical properties of alloyed metal nanoclusters the most important aspect is the correct choice of the alloyed nanoparticle dielectric function. The bimetallic nanoparticle dielectric function is assumed to be a weighted linear combination of dielectric functions for single particles. It can be calculated in terms of the dielectric functions ε_{Ag} and ε_{Au} for nanoparticles of the same size consisting of the pure metals [20, 21]:

$$\varepsilon_{Alloy} = \alpha\varepsilon_{Ag} + (1 - \alpha)\varepsilon_{Au}, \tag{4.5}$$

where α the relative volume concentration of Ag inside the nanoparticle.

The important quantity in Eqs.1 and 5 is the nanoparticles dielectric function ε which differs from that of the bulk metals. It has been shown that the noble metals gold and silver cannot be treated as a free electron gas, in which the dielectric function can be

written within the Drude formula. It is generally accepted that a good approximation of the dielectric function of small particles is obtained from the bulk dielectric function, considering the contributions of the interband contributions [21, 22]. Consequently, the dielectric function is written as:

$$\varepsilon = \varepsilon_1 + i\varepsilon_2, \tag{4.6}$$

$$\varepsilon_{1,2} = \varepsilon_{1,2}^{D} + \chi_{1,2}^{IB}, \tag{4.7a}$$

$$\varepsilon_1^D = 1 - \omega_p^2/(\omega^2 + \gamma^2), \tag{4.7b}$$

$$\varepsilon_2^D = \omega_p^2\gamma/[\omega(\omega^2 + \gamma^2)], \tag{4.7c}$$

where $\varepsilon_{1,2}^{D}$ and $\chi_{1,2}^{IB}$ are the real and imaginary parts of the free electrons and interband contributions into ε, ω_p is the plasma frequency, and γ the rate of electron collisions. Silver and gold have close bulk plasma frequencies: $\hbar\omega_p = 8.5\,eV$ for silver and $\hbar\omega_p = 9.0\,eV$ for gold, and $\hbar$ is the reduced Planck constant [21, 23]. As the particle size reduces, the rate of scattering from the particle surface γ_s becomes larger than the bulk scattering γ_0, and the following relation can be obtained:

$$\gamma = \gamma_0 + \frac{aV_F}{r}, \tag{4.8}$$

where V_F is the Fermi velocity and r is the particle radius. For gold and silver, the Fermi velocity gets almost the same value $V_F = 1.4\,nm \cdot fs^{-1}$, $\hbar\gamma_0 = 0.021\,eV$ and $0.07\,eV$ for silver and gold, respectively [23, 24]. The coefficient a in Eq. 4.8 usually takes the value of unity, which is actually used to consider some of the other factors like electron density at the surface. Therefore, the differences between the dielectric functions of nanoparticles and bulk metals are included in the free electron part of the dielectric function. The contribution arising from interband transitions is assumed to be

unchanged. The analytical calculation of interband dielectric function is complicated. However, it is possible to approximate the real interband part of the dielectric function χ_1^{IB} by using the appropriate values. In the present calculations, the interband dielectric functions were extracted from pure gold and silver nanoparticles with diameters of several tens of nanometers [22]:

$$\chi_1^{IB}(Ag) = Re\left(\chi_{Ag}^{IB}\right) = 2.25 \pm 0.1, \tag{4.9a}$$

$$\chi_1^{IB}(Au) = Re(\chi_{Au}^{IB}) = 7.2 \pm 0.1, \tag{4.9a}$$

In general, if the imaginary interband part of the dielectric function χ_2^{IB} is much smaller than the real part χ_1^{IB}, the following expression for the resonance frequency can be obtained from Eq. 1:

$$\omega_R = \left(\frac{\omega_p^2}{1+\chi_1^{IB}+[(1-P_j)/P_j]\varepsilon_m} - \gamma^2\right)^{1/2}, \tag{4.10}$$

where ω_R is the LSPR peak frequency. Converting from frequency to wavelength via $\lambda = 2\pi c/\omega_R$, the LSPR peak wavelengths can be obtained as follows:

$$\lambda_R = 2\pi c\left(\frac{\omega_p^2}{1+\chi_1^{IB}+[(1-P_j)/P_j]\varepsilon_m} - \gamma^2\right)^{-1/2}, \tag{4.11}$$

In the Gans estimation of LSPR peak positions, the effect of SiO_2 glass substrate must be taken into consideration. We have used the effective medium approximation of Kelly *et al*. [25]. In that method, the effective dielectric constant of the medium surrounding the nanospheroids was defined as the weighted average of the dielectric constants of the substrate and of the air above the substrate, with the weight determined by the relative areas of the nanoparticle exposed to the substrate and to air [25, 26]. As the dielectric constant of the SiO_2 glass substrate used in our study is 3.9, the effective dielectric constant surrounding the nanospheroids is:

$$\varepsilon_m = \frac{\varepsilon_{air}+\varepsilon_{SiO_2}}{2} = 2.45, \quad (4.12)$$

assuming the nanostructures are half embedded in the SiO_2 substrate. Therefore, the longitudinal plasmon mode for the LSPR peak positions of $Ag_{(50\%)}$–$Au_{(50\%)}$ bimetallic nanospheroids as a function of the irradiation fluence is estimated to be shifted from 587 to 483 nm, as shown in Fig. 3c, where the average sizes and aspect ratios obtained from SEM micrographs were used. However, the calculations overestimate the LSPR peaks for the samples with the irradiation fluences less than 7.0×10^{16} cm^{-2}. This is because the bimetallic nanostructures were simplified to be prolate spheroids, in which the aspect ratio is only used to characterize the shape. The shapes other than spheroid like triangle and dumbbell like nanostructures has a certain contribution to the resonance frequency, which can be verified by the large deviation of the aspect ratio obtained by lower dose irradiation ($< 7.0\times10^{16}$ cm^{-2}).

As mentioned previously, a shift of the LSPR peaks towards the longer wavelength (red shift) was observed when the irradiation fluence increased to 1.4×10^{17} cm^{-2}. This is because of the peculiar topology of the core–satellite nanostructures formed in the ion irradiated samples by producing a red shift of the LSPR absorption band [17]. As noticed in high–resolution TEM micrograph in Fig. 4.16c, a halo of satellite clusters around the core nanospheroid formed in the embedded substrate. The formation of the satellite nanoclusters can be understood in terms of ballistic processes induced by the collisional cascades [27]. The Au and Ag atoms are ejected from the original alloy clusters following a ballistic process, and then diffuse into the SiO_2 matrix due to the radiation enhanced diffusion, starting the nucleation and growth where their concentration overcomes their solubility limit. Therefore, a strong coupling between the

core spheroid and the satellite nanoclusters appeared, which strongly affects the local field near the core surface [17]. The generalized multisphere Mie (GMM) theory has been used to model the optical response of these strongly interacting spherical satellites with the core sphere. P. Mazzoldi's group have studied the optical property of such core–satellite nanostructures, in which red shifts of 20 nm and 60 nm were obtained for the Ne^{+} and Kr^{++} irradiated $Ag_{0.4}Au_{0.6}$ alloyed nanoplanets in silica, respectively [17].

4.4.2 Generalized Multi-sphere Mie Theory

Up to this point we always considered ensembles of isolated nanoparticles, where the particles spacing were so large that the direct interactions could be neglected. When several particles are brought close to one another, electromagnetic coupling effects set in, and the LSP resonances are determined by the collective behaviour of the system, so that the overall optical response can be significantly modified with respect to the isolated case. Usually, two different interactions regimes are distinguished, depending on the interparticle distance d: for closely spaced particles, $d \ll \lambda$, near-field interactions proportional to d^{-3} dominate and the particles can be described as an array of interacting point dipoles; due to the rapid scaling of the interaction strength with distance, this regime holds for particle separations below ≈ 150 nm. For larger separations, the near field can be neglected and the dipolar coupling is mainly through far field of the scattered light, which scales as d^{-1}.

When nanoparticles are more or less strongly pinned to each other, the scattering and absorption by this particle aggregate must differ from that of the primary particles which form the aggregate [17, 28, 29]. When the interparticle distance is reduced to such an extent that NPs can no longer be considered as independent, each of them feels not only the external incoming field but also the sum of the fields scattered by all the others. In this case, to properly model the optical response of strongly interacting spherical NPs, the generalized multiparticle Mie (GMM) theory has to be used [28, 29] for the case of N spherical particles with N > 2. The extension of Yu-Lin Xu's GMM Fortran program by Moritz Ringer in his PhD thesis (GMM-Filed) allows computing the near field. Also, Giovanni Pellegrini did a similar extension of the GMM program.

Ion Induced Core-Satellite Structures

Ion implantation can be used to obtain nanostructures that exhibit a dimer-like interaction. Such structures have been called nanoplanets and are composed by a large central NP (5–30 nm in diameter) whose surface is surrounded by a halo of smaller (1–5 nm) NPs (the satellites) extending up to 10–20 nm from the central NP. These are obtained for instance by irradiating Au_xAg_{1-x} alloy NPs with 190 keV Ne^+ ions. The main advantage of ion irradiation is that the nanoplanet topology can be tailored by tuning the irradiation parameters (fluence, energy, ions, flux), as discussed in [17, 27]. The irradiation effect is shown for Au_xAg_{1-x} alloy NPs (x=0.6) in Fig. 4.10b in comparison with the unirradiated reference, Fig. 4.10a. Their size and density can be increased by increasing the nuclear fraction (S_n) of the energy loss by using different ions, like He, Ne, Ar or Kr ions, at different fluence and energy (to deposit the same energy and power density on the sample).

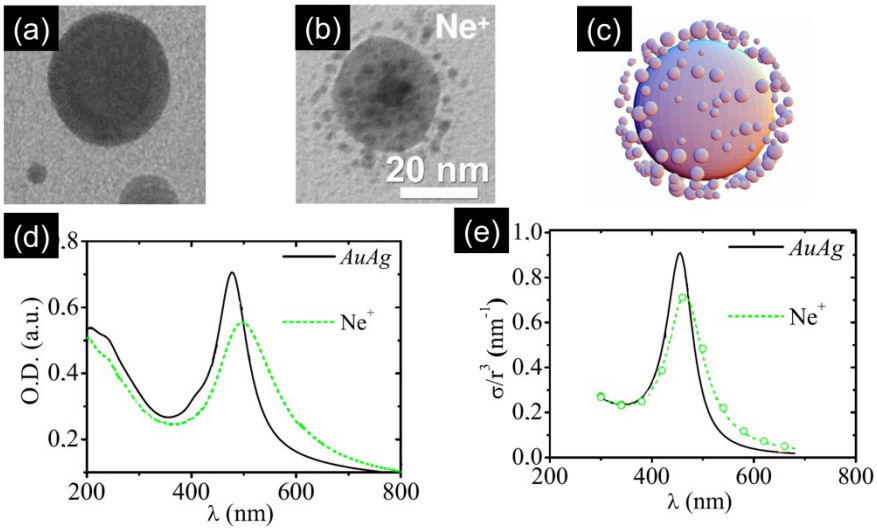

Fig. 4.10: Bright-field TEM cross-sectional micrographs of Au_xAg_{1-x} alloy NPs (x=0.6, annealed in air at 800 C for 1 h) before (a) and after (b) irradiation at room temperature with 190-keV Ne^+, at a

current density 5.2×10^{16} ions cm^{-2} and fuence of 0.84 μA cm^{-2}. (b) The experimental core-satellite nanostructure obtained upon Ne irradiation on a AuAg NP, (c) its corresponding model, (d) the measured optical absorption spectra as a function of wavelength after Ne^{+} irradiation, and (e) the computed optical absorption spectra as a function of wavelength. (Adopted from Ref. [17])

The local-field properties of the nanoplanet configuration are interesting also for the presence of hot spots. In Fig. 4.10c, a GMM calculation of the field distribution around the central NP due to the coupling with its satellites was obtained.

20 nm Au film's optical response with irradiation fluence

Surface plasmon resonance response under different ion fluence was also tested with the 20 nm Au films on SiO_2 glass substrates. A similar tendency of surface plasmon resonance response to irradiation fluence was obtained. As the irradiation fluence increased, a shift of the LSPR peak positions toward the shorter wavelength was observed up to an irradiation fluence of 7.5×10^{17} cm^{-2}, and then shifted towards the longer wavelength with further irradiation (Figure 4.11). Therefore, we expect that for the 100 keV Ar ion irradiation of 20 nm Ag–Au bimetallic film on SiO_2 glass substrate, the enhanced photoabsorption peak would be also shifted toward the shorter wavelength with the increase of irradiation fluence, and then shifted toward the longer wavelength with further irradiation.

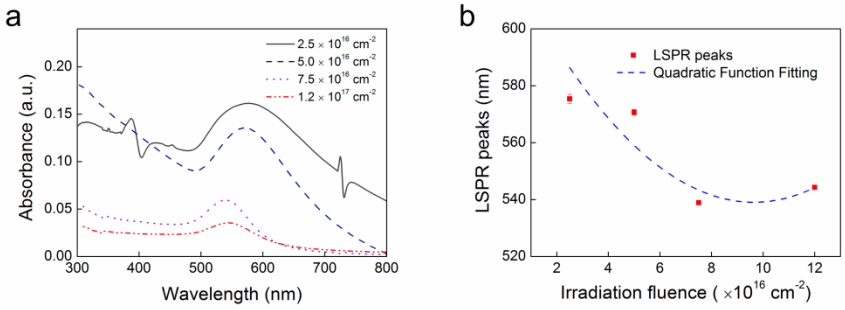

Fig. 4.11 (a) photoabsorbance spectra of the samples after 100 keV Ar ion irradiation at fluences ranging from 2.5×10^{16} cm^{-2} to 1.2×10^{17} cm^{-2}; and (b) experimentally measured maximum absorption wavelength positions plotted against irradiation fluence.

Optical properties' dependence on Chemical component

For the $Ag_{(X\%)}$–$Au_{(100-X\%)}$ bimetallic nanospheroids with a comparable size, the peak positions for the LSPR spectra were estimated to be shifted approximately linearly from 440.4 to 517.0 nm with the increase of Au concentrations (Fig. 4.6c), which fits the tendency of the experimental data well. Also, this result is consistent with previous works [14, 20, 30], in which the Ag–Au alloy nanoparticles were synthesized through chemical methods. However, the calculation underestimates the shift observed in the experimental data. The most relevant factors controlling the position of the SPR absorption band are the size, shape, compositions of the nanospheroids, the refractive index of the matrix, and the interactions among the nanospheroids, as the extensions of the Gans theory have demonstrated. As the $Ag_{(X\%)}$–$Au_{(100-X\%)}$ bimetallic nanospheroids have a comparable size distribution and aspect ratio distribution (Fig. 4.6a), some other factors should be take into consideration. The local refractive index was increased because of the metal atoms dispersed in the dielectric matrix due to the irradiation induced forward recoiling contributes by producing a red shift of the SPR absorption band. Also, the peculiar topology of the core–satellite nanostructures formed in the ion irradiated samples has a contribution of the red shift of the SPR absorption band, as discussed previously.

4.5 Conclusions

In this paper, Ar–ion irradiation induced surface nanostructuring of Ag–Au bimetallic films on SiO_2 substrates and their optical properties were investigated. The surface morphology was examined using a SEM equipped with an EDS, and the microstructure of the fabricated Ag–Au nanospheroids were examined using a TEM. The following conclusions were obtained;

1. As the irradiation fluence increases from 4.0×10^{16} cm^{-2} to 1.4×10^{17} cm^{-2}, the $Ag_{(50\%)}$–$Au_{(50\%)}$ bimetallic nanospheroids on the SiO_2 substrate were formed. The mean size of the nanospheroids decreases and the aspect ratio approaches unity with an increase in the irradiation fluence. This results in a shift of the LSPR peaks towards the shorter wavelength up to an irradiation fluence of 1.0×10^{17} cm^{-2}, which is in good agreement with the Gans calculation. The peak was then shifted towards the longer wavelength because of the strong coupling between the core spheroid and the satellite nanoclusters via ballistic processes.

2. Tuning of the LSPR frequency over a wider range has been achieved by modifying the Ag–Au molar ratios, and a remarkable LSPR peaks shifted approximately linearly towards the longer wavelength with the increase of the Au concentration has been obtained, with a tendency in good agreement with the Gans calculation. However, the calculation underestimates the shift observed in the experimental data because of the increase of the local refractive index and the peculiar topology of the core–satellite nanospheroids, both have contributions by producing a red shift of the LSPR absorption band.

In summary, ion irradiation and post–annealing can be considered as effective

approaches in surface nanostructuring and therefore in the fabrication of photosensitive bimetallic–silica nanocomposites. Moreover, irradiation enhanced diffusion effectively burrows the nanospheroids with functionalization surfaces into the dielectric platform, and potential application use in solid–state devices is expected.

5 Ion Beam Surface Nanostructuring of Ag–Au Bimetallic Films on Sapphire

5.1 Introduction

The effect of substrate must be taken into consideration. The effective medium approximation was studied. In this method, the effective dielectric constant of the medium surrounding the nanoparticles was defined as the weighted average of the dielectric constants of the substrate and of the air above the substrate, with the weight determined by the relative areas of the nanoparticle exposed to the substrate and to air.

In the previous two chapters, we have synthesized single–layer gold nanoparticles partially embedded in SiO_2 glass. Also, Ag–Au bimetallic nanoparticles were synthesized and partially embedded in SiO_2 glass. In this study, 100 keV Ar–ion irradiation was adopted for the synthesis of gold–silver bimetallic nanoparticles on single crystal Al_2O_3 substrates to have a investigation of the substrate structure's effects on ion irradiation induced surface nanostructure's formation and also on their optical properties behavior.

5.2 Experimental Details

Ion irradiation induced surface nanostructuring of Ag–Au bimetallic films with various molar ratios deposited on Al_2O_3 substrates was performed, and the tunable plasmon resonance frequency was observed. The Ag–Au bimetallic thin films were thermally evaporated on mirror polished Al_2O_3 single crystal (viz. sapphire) substrates at ambient temperature by electrically heating the Ag and Au source under a 6.0×10^{-5} Torr vacuum. The film thickness was verified to be 30 nm using a cross–sectional transmission electron microscope (TEM; JEOL JEM–2010F). After deposition, the surface morphology was analyzed using a field–emission scanning electron microscope (SEM; JEOL JSM–7001FA).

For the $Ag_{(40\%)}$–$Au_{(60\%)}$ mixture deposited on the Al_2O_3 substrates, irradiations with 100 keV Ar ions at ambient temperature with fluences of 5.0×10^{15} cm^{-2}, 1.0×10^{16} cm^{-2}, 3.8×10^{16} cm^{-2}, 4.5×10^{16} cm^{-2}, 5.2×10^{16} cm^{-2}, and 6.3×10^{16} cm^{-2} were performed to study the fluence dependence. Energies of the ions were chosen such that the range is wider than the thickness of the bimetallic layer, as calculated using the SRIM 2011 code [1]. Ar–ion irradiation on the specimen was performed using the 400 keV ion accelerator at the HVEM laboratory, Hokkaido University. A low pressure of 10^{-3} Pa was maintained inside the irradiation chamber by a turbo–molecular pump. To ensure uniform irradiation, Ar–ion beam was scanned and the current was maintained at approximately 1.5 μA cm^{-2}. To investigate the chemical component dependence, Ar–ion irradiations of Ag–Au bimetallic films with molar ratios of 0.0:1.0, 0.2:0.8, 0.4:0.6, 0.8:0.2, and 1.0:0.0 on Al_2O_3 substrates were also performed to a fluence of 6.3×10^{16} cm^{-2}. After the ion irradiation, bimetallic nanostructures with Au:Ag molar ratios of

0.0:1.0, 0.37:0.63, 0.49:0.51, 0.65:0.35, and 1.0:0.0 were synthesized due to the preferential sputtering effects under Ar ion irradiation. Optical absorption spectra were recorded over a wavelength range of 300–800 nm on a spectrophotometer (JASCO V–630) with a spectral bandwidth of 1.5 nm, and SEM observations were conducted to examine the surface modifications. The surface elemental concentration was evaluated using the SEM coupled with an energy–dispersive spectrometer (EDS). For the specimen irradiated to a fluence of 1.0×10^{16} cm^{-2}, nanoscale mapping of the surface chemical concentration was obtained using SEM equipped with EDS, which was operated at 6.0 keV. Thermal annealing was subsequently performed under high vacuum (4.25×10^{-5} Pa) at 1073 K for 2 hours, and SEM observation and photoabsorption spectra were collected to examine the surface morphology and optical properties of the samples. Moreover, microstructural characterization was performed using TEM operated at 200 keV. Cross–sectional TEM specimens were prepared using a precision ion polishing system (PIPS; JEOL AT–12310).

5.3 Results and Discussions

5.3.1 Surface nanostructuring after Ar–ion irradiation

Effects of the ion induced surface nanostructuring were studied using 100 keV Ar–ion irradiation of 30 nm Ag–Au bimetallic films deposited on Al_2O_3 substrates with the irradiation fluence increased from 5.0×10^{15} cm^{-2} to 6.3×10^{16} cm^{-2}. The ion beam induced surface nanostructures before and after irradiation were observed using SEM. For the specimen irradiated to a fluence of 1.0×10^{16} cm^{-2}, chemical concentration maps were obtained (Fig. 5.1). Figures 5.1b–d show the EDS maps for alumina, silver, and gold on the sample's surface; the maps indicate that the silver and gold concentration patterns correspond to the bright network–like pattern shown in Fig. 5.1a. The bright contrast in the SEM images represents the retained bimetallic films on the Al_2O_3 substrates. Moreover, the surface concentration patterns of silver and gold are consistent with each other, which illustrate the nanoscale atomic mixing of Ag and Au.

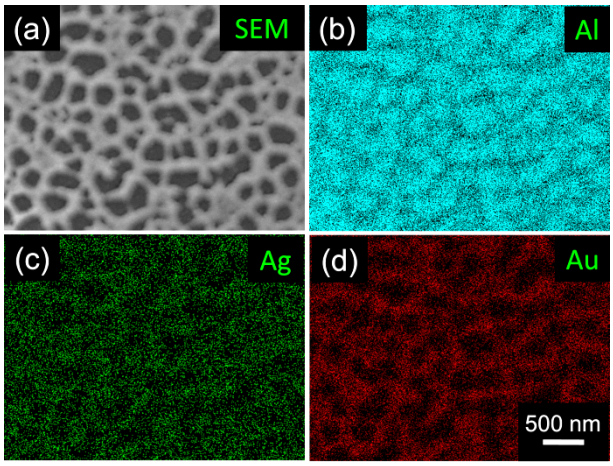

Fig. 5.1: Surface chemical concentration of $Ag_{(40\%)}$–$Au_{(60\%)}$ deposited on Al_2O_3 irradiated to a fluence of 1.0×10^{16} cm^{-2}: (a) SEM image of the sample, (b–d) EDS maps of aluminum, silver, and gold, respectively.

With increase in the irradiation fluence, the process of bimetallic film dewetting under Ar–ion irradiation was clearly distinguished, and the formation of isolated nanostructures was finally observed. The surface of the as–deposited Al_2O_3 substrate is smooth with fine particles in a scale down to a few nanometers (inset 1 in Fig.5.2a), whereas the surface roughness increased and holes formed after irradiation to a fluence of 5.0×10^{15} cm^{-2} (inset 2 in Fig. 5.2a); furthermore, the holes grew larger as the irradiation fluence increased. When the irradiation fluence increased to 3.8×10^{16} cm^{-2}, partially connected nanoscale islands formed (inset 3 in Fig. 5.2a). Finally, isolated nanoscale islands formed on the surface when the irradiation fluence reached 6.3×10^{16} cm^{-2} (inset 4 in Fig. 5.2a). The nanoscale islands were formed because of lateral transport of Ag and Au atoms, which is enhanced by the irradiation induced diffusion, taking into the sputtering effects [2-6]. Similar features of ion induced dewetting have been reported for 800keV Kr–ion irradiation of thin Pt films on SiO_2 substrates [3], 150 keV Ar–ion irradiation of thin Au films on carbonaceous substrates [4] and 100 keV Ar–ion irradiation of thin Au films on SiO_2 substrates [6]. Areal coverage of the bimetallic films was estimated for each irradiation fluence; the areal coverage decreased linearly with increasing irradiation fluence until 4.5×10^{16} cm^{-2}, and deviated from the linear tendency thereafter, as shown in Fig. 5.2a. The reason for this slowed decrease was the small fraction of the surface area covered by bimetallic film with increasing irradiation fluence. In addition, a chemical concentration change of $Ag_{40\%}$–$Au_{60\%}$ bimetallic films under Ar–ion irradiation was obtained by SEM–EDS analysis, which was induced by the preferential sputtering effects. With the increase of the irradiation fluence, the concentration of silver increases from 39.7% (as–deposited film) to 50.5% (with the irradiation fluence of 3.8×10^{16} cm^{-2}), and then reaches the stable value around

50% (Fig. 5.2b).

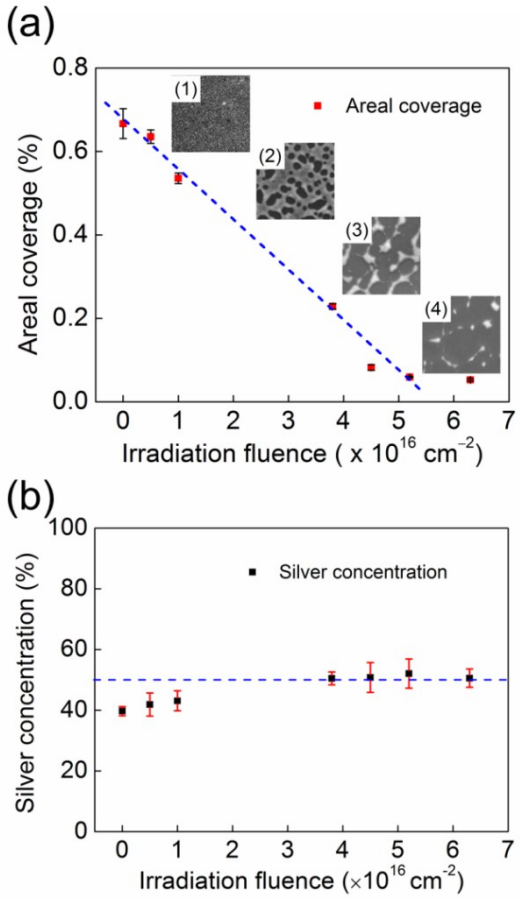

Fig. 5.2: (a) Dependence of the Ag–Au bimetallic film areal coverage on the irradiation fluence; the insets are SEM images (1.0×1.0 μm^2) for (1) $Ag_{(40\%)}$–$Au_{(60\%)}$ as–deposited samples and the samples irradiated at fluences of (2) 5.0 × 10^{15} cm^{-2}, (3) 3.8 × 10^{16} cm^{-2}, and (4) 6.3 × 10^{16} cm^{-2}. (b) Dependence of the silver concentration in Ag–Au bimetallic film on the irradiation fluence.

5.3.2 Effects of annealing on the nanostructures

The morphologies of the samples undergo notable variations upon thermal annealing, as revealed in the SEM images in Fig. 5.3. In particular, some major differences were detected after thermal annealing. As–deposited Ag–Au films on Al_2O_3 substrate after

thermal annealing is quite different from the ion irradiated sample; relatively large nanoscale pitches with a Heywood diameter greater than 200 nm were observed (Fig. 5.3a). For the sample irradiated to a fluence of 5.0×10^{15} cm^{-2}, network–like bimetallic layers aggregated to form larger nanoballs with a small portion retained, (Fig. 5.3b). When the fluence exceeded 3.8×10^{16} cm^{-2}, partially connected nanoscale islands transformed into spherical nanoballs (Fig. 5.3c and d). For each thermal annealed sample, mean diameter of these nanoballs was reproduced using a Gaussian fitting. The mean diameter was deduced as the position of the Gaussian peak, and the error was evaluated as the standard deviation of the Gaussian fitting. Figure 5.3 illustrates the mean diameter as a function of irradiation fluence, which shows an exponential decrease with the irradiation fluence.

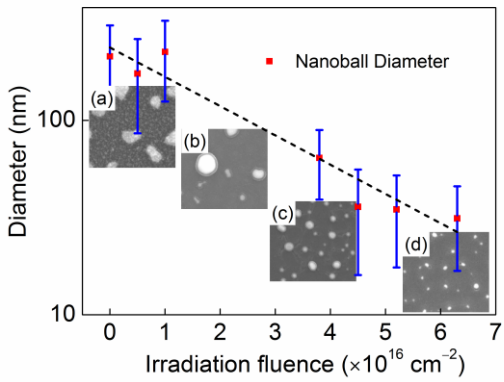

Fig. 5.3: Dependence of the nanoball diameter on the irradiation fluence after thermal annealing; the insets are SEM images (1.0×1.0 μm^2) for (a) $Ag_{(40\%)}$–$Au_{(60\%)}$ as–deposited samples and the samples irradiated at fluences of (b) 5.0×10^{15} cm^{-2}, (c) 3.8×10^{16} cm^{-2}, and (d) 6.3×10^{16} cm^{-2}.

A detailed investigation of these nanoballs was performed using a TEM, showing the spherical nanoballs were partially embedded in the substrate (Fig. 5.4a). The bimetallic nanoballs embedment in the Al_2O_3 substrate can be interpreted as thermodynamic

driving forces resulting from different surface energies of the particle and its substrate in relation to their particle–substrate interface energy, which can lead to a burrowing of the particles if the ion bombardment can induce effective ion–induced viscosity of the substrate [7]. The crystalline sapphire has such a low ion–induced viscosity that the burrowing effect can be neglected. However, the near surface of the sapphire became amorphous after the extensive Ar–ion irradiation (approximately above 3.8×10^{16} cm^{-2} in our study), which can be verified by the selected area diffraction pattern in the TEM observation. A weak diffuse ring with the faded crystalline spots were observed after the irradiation at a fluence of 4.5×10^{16} cm^{-2} (Fig. 5.4b) indicating the formation of the amorphous layer. Therefore, ion irradiation induced viscosity of the amorphous Al_2O_3 layer was sufficient enough to accomplish this burrowing process. Moreover, diffraction pattern was obtained for a particular Ag–Au nanoball (Fig. 5.4c), showing the nanoball exhibited a FCC structure.

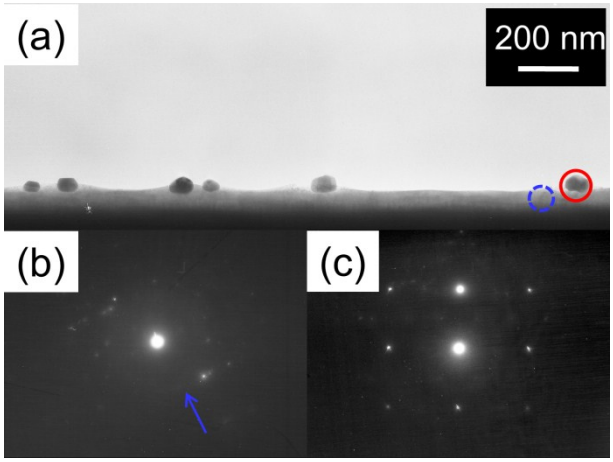

Fig. 5.4: (a) Bright field cross sectional TEM image of $Ag_{(40\%)}$–$Au_{(60\%)}$ deposited on Al_2O_3 irradiated with 100 keV Ar–ions at a fluence of 4.5×10^{16} cm^{-2} and thermally annealed thereafter; (b) diffraction pattern for the Al_2O_3 substrate circled in dashed line in (a); (c) diffraction pattern for the Ag–Au alloy nanoball circled in solid line in (a).

The above mentioned changes in the microstructure of the nanoballs on annealing, both from compositional and morphological points of view, strongly influence optical response. Figure 5.5 shows the photoabsorption spectra after thermal annealing of the samples irradiated from 3.8 × 10^{16} cm^{-2} to 6.3 × 10^{16} cm^{-2}. The absorbance band located at approximately 580 nm corresponds to the localized surface plasmon resonance (LSPR) peak exhibited by Ag–Au bimetallic nanoballs partially embedded in amorphous sapphire substrate [8, 9], and the LSPR bands show a progressive blue–shift.

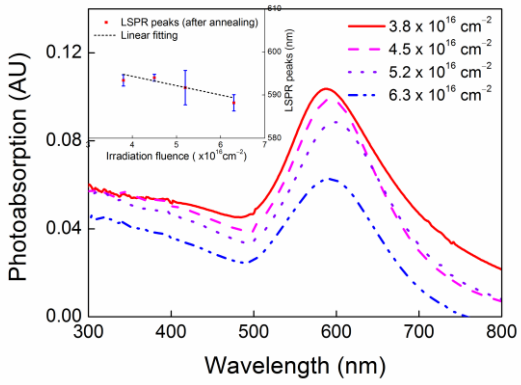

Fig. 5.5: Photoabsorption spectra of the samples irradiated at fluences from 3.8 × 10^{16} cm^{-2} to 6.3 × 10^{16} cm^{-2} and thermally annealed thereafter. The inset shows the LSPR positions with their standard deviations as a function of the irradiation fluence.

In general, the positions of the SPR peaks are closely related to the shape, size, and chemical composition of the nanoballs. As the irradiation fluence increased from 3.8 × 10^{16} cm^{-2} to 6.3 × 10^{16} cm^{-2}, the size of the Au nanoballs decreased, which is consistent with the blue shift of the LSPR peaks (inset in Fig. 5.5). For each sample, the spectra were measured for five times. The LSPR positions shown in the inset of Fig. 5.5 were choice as averaged values with their standard deviations.

5.3.3 Ag–Au nanoballs with a tunable surface plasmon resonance frequency

Photosensitive bimetallic nanoballs with various Au:Ag molar ratios (0.0:1.0, 0.37:0.63, 0.49:0.51, 0.65:0.35, and 1.0:0.0) were synthesized using pre–determined molar ratios of mixtures of Au and Ag deposited on Al_2O_3 substrates. These samples were therefore irradiated with 100 keV Ar–ions to a fluence of 6.3×10^{16} cm^{-2}, and the surface morphology of the samples were examined using SEM.

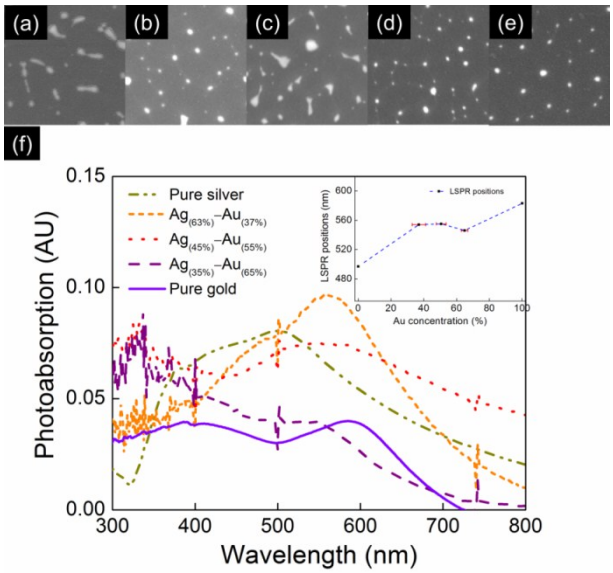

Fig. 5.6: SEM images (1.0×1.0 μm^2) of 100 keV Ar–ion irradiation of the samples with (a) pure silver, (b) $Ag_{(80\%)}$–$Au_{(20\%)}$, (c) $Ag_{(40\%)}$–$Au_{(60\%)}$, (d) $Ag_{(20\%)}$–$Au_{(80\%)}$, (e) pure gold deposited on Al_2O_3 at a fluence of 6.3×10^{16} cm^{-2}. (f) Photoabsorption spectra of these samples after Ar–ion irradiation; the inset shows the LSPR positions as a function of the Au concentration.

Figures 5.6 a–e showed the formation of nanoballs for all five sets of the investigated samples, and Fig. 5.6f shows the tunable characteristics of the LSPR frequency of Ag–Au bimetallic nanoballs. The surface plasmon absorption band was observed, and the wavelengths of maximum absorption were found to be red–shifted from

approximately 497 nm (Ag nanoballs) to 583 nm (Au nanoballs) with increase in Au molar fraction. In addition, interband transitions induced absorption can be clearly recognized, especially for the wavelength less than 400 nm, and they are clearly separated from the resonance position of the surface plasmon peaks. However, for the pure silver and $Ag_{(63\%)}$–$Au_{(37\%)}$ samples, a superposition of two absorption bands were observed above 400 nm. The appearance of these bands can be clarified by the multipole excitation [10]. As the isolated nanostructures with larger size and irregular shapes appeared in their surface, multipole resonances were excited, resulting in more than one plasmon resonances peaks. The inset in Fig. 5.6f presents the maximum absorption peak plotted as a function of Au concentration. Even though broad absorption bands were observed for certain Ag–Au molar ratios, the maximum absorption peaks shifted toward longer wavelengths with increase in Au concentration. Therefore, the LSPR depended on the chemical concentration of the nanoballs on Al_2O_3 substrate, and the LSPR peaks tended to red–shift with increasing Au concentration. However, this tendency deviated from the theoretical calculation [11] because various parameters such as nanoballs size and shape influence the LSPR peaks. Therefore, further investigation is needed to resolve this matter.

5.4 Conclusions

In this study, the process of ion irradiation induced surface nanostructuring of Ag–Au bimetallic films on Al_2O_3 substrates was studied. The process of the dewetting of the Ag–Au films with the increase of irradiation fluence was examined by SEM. After they were thermally annealed, the nanostructures transformed into spherical nanoballs, and a blue–shift of the LSPR peaks was observed with the increase of the irradiation fluence. Dependence of the LSPR on the chemical concentration was also observed, and the LSPR peaks exhibited a tendency of red–shift with the increasing Au concentration. In summary, ion irradiation is an effective approach in surface nanostructuring and in controlling the LSPR properties of the metallic films on Al_2O_3 substrates. The application of these nanocomposites in optical devices is expected.

6 Conclusions

In this study, 100 keV Ar-ion irradiation on thin metallic film deposited dielectric substrates was employed. Ion-beam induced surface nanostructruring were investigated by atomic force microscopy (AFM) and scanning electron microscopy (SEM). Further irradiation effectively initiate the burrowing of the nanostructures into dielectric matrix, as the ion-induced viscous flow is sufficient enough to accomplish this burrowing process. This was verified by cross sectional microstructure observation and chemical characterization obtained by transmission electron microscopy (TEM) equipped with an energy-dispersive spectrometer (EDS). Finally, their optical responses were evaluated by photo absorption spectra, obtained by a double beam spectrophotometer, and the characteristic LSPR band was observed for the metallic nanoparticles. In addition, the synergistic control of various parameters sensitive to the LSPR band includes both particle size and shape, which was realized by modifies the ion beam current, energy, fluence, and also the metallic film thickness. Further control of LSPR frequency over a wider range has been achieved by synthesizing bimetallic nanoparticles fabricated in the form of alloys of two metals.

The dependence of mean size of the Ag-Au bimetallic nanospheroids on the SiO_2 substrate and the aspect ratio on optical response were studied. A remarkable LSPR peaks shifted approximately linearly towards the longer wavelength with the increase of the Au concentration has been obtained. Gans theory has been used to model the optical response of these metallic nanospheroids on SiO_2 substrates. Gans theory accounts for the main effects associated with the major parameters affecting the LSPs resonances. However, comparing experimental results with the Gans predictions some discrepancies

remain. Two corrections should be taken into consideration: firstly, the recoiled mixing of metallic atoms into dielectric substrate induces the increase of the dielectric function of the SiO_2 matrix; secondly, nanoparticles under ion irradiation undergo break up into nanospheroids structures and therefore results in the strong coupling between the core nanoparticle and the satellite fragments.

Finally, morphologies and the optical properties of the nanoparticles on the SiO_2 glass under Ar ion irradiation were examined using SEM and spectrometer. The ion enhanced sputtering effects of Au nanoparticles was discussed, and the resulting optical absorption band shift was interpreted. In summary, ion irradiation is an effective approach in surface nanostructuring and in controlling the LSPR properties of the metallic films on dielectric substrates, such as SiO_2 and Al_2O_3. The application of these nanocomposites in optical devices is expected.

Acknowledgements

The first grateful words are for my supervisors: Professor Shibayama, Professor Watanabe, Professor Sasaki, and Professor Furusaka, who professionally and sympathetically help and support me. I am also appreciating all the other co-supervisors: Prof. Itagaki, Prof. Asakura, Prof. Ohnuma, Prof. Kozaki, Prof. Kurokawa, Prof. Koshizaki, Prof. Kamiyama, and Prof. Kaneko. I am very thankful for Dr. Werawan's contribution to the e^3 English program. I am very appreciating my e^3 evaluation committee members: Prof. T. Hino and Prof. T. Sumiyoshi, who give me important advices and courages.

I sincerely acknowledge Prof. Shibayama for his helpful tutorials in performing Ar Ion irradiation. I would like to say that I cannot accomplish my study without his role. He provides me with professional guidance, raises me up from my depression, connects me with nice people, and spiritually makes me feel happy and safe. I also would like to thank Prof. Sakaguchi for his support on FE-TEM oprations. I also would like to say thanks to Dr. Yang for her TEM tutorials and Mr. Yu for their support.

Prof. Watanabe's Quantum Energy and Conversion Material Laborotory is a comfortable working environment for me, with youthful and friendly members (Dr. Yang, Dr. Yoshida, Dr. Ishioka, Mr. Rafiq, Mr. Yu, Mr. Takayanagi, Mr. Hosogawa, Mr. Jinno, Mr. Takano, Mr. Akamatsu, and Mr. Melbert). Mr. Ohkubo, with his technique assistant always makes my research work more enjoyable. I also thank Mrs. Yamamoto and Mr. Tanioka, and Mr. Oota for their nice help and collaboration with me in the cross sectional TEM specimen preparation.

I also would like to thank Prof. Wang from School of Nuclear Science and Technology, Lanzhou University, who provided me the opportunity to study abroad. I acknowledge Prof. Peng and Dr. Fang's help in application of the CSC scholarship. The funding for my study is offered by Chinese

Scholarship Council (CSC). Also, this study was supported partly by the Japan Society for the Promotion of Science (JSPS). I'm highly grateful to these sponsors who allow me to pursue the PhD program. Finally, the great spiritual mainstay for me is the constant support and care by my parents and my sisters who always look forward to my mature and success. I also would like to mention the support and encouragement by my friends. I also thank Miss. Cai for her kind–hearted supports in my life in Sapporo.

References

Chapter 1

1. P. M. Ajayan and L. D. Marks, Evidence for sinking of small particles into substrates and implications for heterogeneous catalysis, Nature (London) **338**(1989) 139–141.
2. M. Valden, X. Lai, and D. W. Goodman, Onset of catalytic activity of gold clusters on titania with the appearance of nonmetallic properties, Science **281**(1998) 1647–1650.
3. H. A. Atwater, The promise of plasmonics, Scientific American (2007) **4:**56–63.
4. Q. Zhao, J. Zhou, F. Zhang, and D. Lippens, Mie resonance-based dielectric metamaterials, Materails Today **12**(2009) 60–69.
5. M. I. Stockman, Nanoplasmonics: the physics behind the applications, Physics Today (2011)2: 39–44.
6. H. A. Atwater and A. Polman, Plasmonics for improved photovoltaic devices, Nature Materials, **9**(2010) 205–213.
7. S. Eustis and M. A. El-Sayed, Why gold nanoparticles are more precious than pretty gold: Noble metal surface plasmon resonance and its enhancement of the radiative and nonradiative properties of nanocrystals of different shapes, Chem. Soc. Rev., **35**(2006) 209–217.
8. M. A. Garcia, Surface plasmons in metallic nanoparticles: fundamentals and applicaitions, J. Phys. D: Appl. Phys. **44**(2011) 283001.
9. J. Zhang, L. Zhang and W. Xu, Surface plasmon polaritons: physics and applications, J. Phys. D: Appl. Phys. **45**(2012) 113001.
10. C.-H. Zhao, B.-P. Zhang, S.-J. Wang, P.-P. Shang, S. Li, L.-P. Yan, Microstructure and optical absorption property of the Cu/SiO_2 nano-films, Materials and Design **32**(2011) 947–950.
11. P. G. Etchegoin and E. C. Le Ru, *Basic Electromagnetic Theory of SERS* in *Surface Enhanced Raman Spectroscopy: Analytical, Biophysical and Life Science Applications* (Edited by Sebastian Schl¨ucker) (Wiley-VCH Verlag, Weinheim, 2011).
12. B. Sharma, R. R. Frontiera, A. –I. Henry, E. Ringe, and R. P. Van Duyne, SERS: Materials, applications, and the future, Materials Today, **15**(2012) 16–25.
13. J. Kneipp, H. Kneipp and K. Kneipp, SERS–a single–molecule and nanoscale tool for bioanalytics, Chem. Soc. Rev., **37**(2008) 1052–1060.
14. J. Zhao, X. Zhang, C. R. Yonzon, A. J. Haes and R. P. Van Duyne, Localized surface plasmon resonance biosensors, Nanomedicine **1**(2006) 219–228.
15. A. J. Haes, W. P. Hall, L. Chang, W. L. Klein, and R. P. Van Duyne, A Localized Surface Plasmon Resonance Biosensor: First Steps toward an Assay for Alzheimer's Disease, Nano Letters **4**(2004) 1029–1034.

16. K. A. Willets and R. P. Van Duyne, Localized Surface Plasmon Resonance Spectroscopy and Sensing, Annu. Rev. Phys. Chem., **58**(2007) 267–297.
17. K. M. Mayer and J. H. Hafner, Localized Surface Plasmon Resonance Sensors, Chem. Rev., **111**(2011) 3828–3857.
18. D. Inoue, A. Miura, T. Nomura, H. Fujikawa, K. Sato, N. Ikeda, D. Tsuya, Y. Sugimoto, and Y. Koide, Polarization independent visible color filter comprising an aluminum film with surface–plasmon enhanced transmission through a subwavelength array of holes, Appl. Phys. Lett. **98**(2011) 093113.
19. P. Raveendran, J. Fu and S. L. Wallen, A simple and "green" method for the synthesis of Au, Ag, and Au–Ag alloy nanoparticles, Green Chem., **8**(2006) 34–38.
20. N. Nath and A. Chilkoti, A colorimetric gold nanoparticle sensor to interrogate biomolecular interactions in real time on a surface, Anal. Chem. **74**(2002) 504–509.
21. C. J. Murphy, Nanocubes and Nanoboxes, Science **298** (2002) 2139.
22. M. P. Mallin and C. J. Murphy, Solution-Phase Synthesis of Sub–10 nm Au–Ag Alloy Nanoparticles, Nano Lett., **2**(2002) 1235–1237.
23. J. C. Hulteen and R. P. Van Duyne, Nanosphere lithography: A materials general fabrication process for periodic particle array surfaces, J. Vac. Sci. Tech. A, **13**(1995) 1553.
24. C. M. M¨uller, F. C. F. Mornaghini and R. Spolenak, Ordered arrays of faceted gold nanoparticles obtained by dewetting and nanosphere lithography, Nanotechnology, **19**(2008) 485306.
25. C. Favazza, J. Trice, R. Kalyanaraman, and R. Sureshkumar, Self–organized metal nanostructures through laser–interference driven thermocapillary convection, Appl. Phys. Lett., **91**(2007) 043105.
26. Y. Kojima and T. Kato, Nanoparticle formation in Au thin films by electron–beam–induced dewetting, Nanotechnology **19**(2008) 255605.
27. M. Nastasi and J.W. Mayer, Ion beam mixing in metallic and semiconductor materials, Materials Science and Engineering, **R12**(1994) 1–52.
28. Stepanova M, Dew SK, Ion beam sputtering nanopatterning of thin metal films: the synergism of kinetic self–organization and coarsening, J. Phys.: Condens. Matter **21**(2009) 224014.
29. J. F. Ziegler, J. P. Biersack, and U. Littmark, *SRIM - The Stopping and Range of Ions in Solids* (Pergamon Press, New York, 1985 (new edition in 2009)).
30. P. Sigmund, Theory of Sputtering. I. Sputtering Yield of Amorphous and Polycrystalline Targets, Phys. Rev., **184**(1969) 383.
31. H. L. Zhu, R. S. Averback, M. Nastasi, Molecular dynamics simulations of a 10keV cascade in β-NiAl, Philos. Mag. A **71**(1995) 735.
32. J. Nord, K. Nordlund, and J. Keinonen, Amorphization mechanism and defect structures in

ion-beam-amorphized Si, Ge, and GaAs, Phys. Rev. B, **65**(2002) 165329

33. R. Nagel, A.G. Balogh, Atomic transport in metal/ceramic interfaces under heavy ion irradiation, Nuclear Instruments and Methods in Physics Research B **156**(1999) 135–142.
34. J. Ghatak, B. Sundaravel, K. G. Nair and P. V. Satyam, Ion–beam–induced enhanced diffusion from gold thin films in silicon, J. Phys.: Condens. Matter **20**(2008) 485008.
35. M. Ghaly and R. S. Averback, Effect of Viscous Flow on ion Damage near Solid Surfaces, Phys. Rev. Lett., **72**(1994) 364–367.
36. X. Hu, D. G. Cahill, and R. S. Averback, Dewetting and nanopattern formation of thin Pt films on SiO_2 induced by ion beam irradiation, J. Appl. Phys. **89**(2001) 7777–7783.
37. X. Hu, D. G. Cahill, R. S. Averback, and R. C. Birtcher, *In–situ* transmission electron microscopy study of irradiation induced dewetting of ultrathin Pt films, J. Appl. Phys. **93**(2003) 165–169.
38. P. Gangopadhyay, S. K. Srivastava, P. Magudapathy, T. N. Sairam, K. G. M. Nair, and B. K. Panigrahi, Ion-beam sputtering and nanostructures of noble metals, Vacuum, **84**(2010) 1411–1414.
39. B. Y. Tsaur, J. W. Mayer Metastable Au–Si alloy formation induced by ion–beam interface mixing, Philos. Mag. A **43**(1981) 345–361.
40. R. C. Birtcher and S. E. Donnelly, Plastic Flow Induced by Single Ion Impacts on Gold, Phys. Rev. Lett., **77**(1996) 4374–4377.
41. X. Hu, D. G. Cahill, and R. S. Averback, Burrowing of Pt Nanoparticles into SiO_2 during Ion–beam Irradiation, J. Appl. Phys. **92**(2002) 3995–4000.
42. A. Klimmer, P. Ziemann, J. Biskupek, U. Kaise, and M. Flesch, Size–dependent effect of ion bombardment on Au nanoparticles on top of various substrates: Thermodynamically dominated capillary forces versus sputtering, Phys. Rev. B **79**(2009) 155427.
43. M. Quinten, Optical Properties of Nanoparticle Systems: Mie and Beyond (Wiley–VCH, Weinheim, 2011).
44. G. Mattei, V. Bello, P. Mazzoldi, G. Pellegrini, C. Sada, C. Maurizio, and G. Battaglin, Modification of composition and structure of bimetallic nanocluster in silica by ion beam irradiation, Nucl. Instrum. Methods Phys. Res., Sect. B **240**(2005) 128–132.
45. G. Pellegrini, V. Bello, G. Mattei, and P. Mazzoldi, Local-field enhancement and plasmon tuning in bimetallic nanoplanets, Optics Express **15**(2007) 10097–10102.

Chapter 2

1. T. Karakouz, A. B. Tesler, T. A. Bendikov, A. Vaskevich, and I. Rubinstein, Highly Stable Localized Plasmon Transducers Obtained by Thermal Embedding of Gold Island Films on Glass, Adv. Mater., **20**(2008) 3893–3899.
2. A. B. Tesler, L. Chuntonov, T. Karakouz, T. A. Bendikov, G. Haran, A. Vaskevich, and I. Rubinstein, Tunable Localized Plasmon Transducers Prepared by Thermal Dewetting of Percolated Evaporated Gold Films, J. Phys. Chem. C, **115**(2011) 24642–24652.
3. J. F. Ziegler, J. P. Biersack, and U. Littmark, *SRIM - The Stopping and Range of Ions in Solids* (Pergamon Press, New York, 1985 (new edition in 2009)).
4. N. Sakaguchi, H. Kinoshita, S. Watanabe, Y. Sueishi, N. Akasaka, and H. Takahashi, Microstructural development in a model austenitic alloy following electron and ion irradiation, Journal of Nuclear Materials, **382** (2008) 197–202.
5. K–S. Lee and M. A. El–Sayed, Dependence of the Enhanced Optical Scattering Efficiency Relative to That of Absorption for Gold Metal Nanorods on Aspect Ratio, Size, End–Cap Shape, and Medium Refractive Index, J. Phys. Chem. B **109**(2005) 20331–20338.
6. M. Quinten, Optical Properties of Nanoparticle Systems: Mie and Beyond (Wiley–VCH, Weinheim, 2011).
7. C. V. Thompson, Solid–State Dewetting of Thin Films, Annu. Rev. Mater. Res. **42**(2012) 399–434.
8. C. D. Marshall, J.A. Speth, and S. A. Payne, Induced optical absorption in gamma, neutron and ultraviolet irradiated fused quartz and silica, Journal of Non–Crystalline Solids **212**(1997) 59–73.

Chapter 3

1. J. F. Ziegler, J. P. Biersack, and U. Littmark, *SRIM - The Stopping and Range of Ions in Solids* (Pergamon Press, New York, 1985 (new edition in 2009)).
2. X. Hu, D. G. Cahill, and R. S. Averback, Dewetting and nanopattern formation of thin Pt films on SiO_2 induced by ion beam irradiation, J. Appl. Phys. **89**(2001) 7777–7783.
3. X. Hu, D. G. Cahill, R. S. Averback, and R. C. Birtcher, *In–situ* transmission electron microscopy study of irradiation induced dewetting of ultrathin Pt films, J. Appl. Phys. **93**(2003) 165–169.
4. K. Zhao, R. S. Averback, and David G. Cahill, Patterning of metal nanowires by directed ion-induced dewetting, Appl. Phys. Lett. **89**(2006) 053103.
5. J. Prakash, A. Tripathi, V. Rigato, J. C. Pivin, J, Tripathi, K. H. Chae, S. Gautam, P. Kumar, K. Asokan, and D. K. Avasthi, Synthesis of Au nanoparticles at the surface and embedded in carbonaceous matrix by 150 keV Ar ion irradiation, J. Phys. D: Appl. Phys. **44**(2011) 125302.
6. K. Neubeck, C. –E. Lefaucheur, H. Hahn, A. G. Balogh, H. Baumann, K. Bethge, and D. M. Rück, Ion beam mixing and radiation enhanced diffusion in metal/ceramic interfaces, Nucl. Instrum. Methods Phys. Res., Sect. B **106**(1995) 589–596.
7. R. Nagel, A.G. Balogh, Atomic transport in metal/ceramic interfaces under heavy ion irradiation, Nuclear Instruments and Methods in Physics Research B **156**(1999) 135-142.
8. W. F. McClune, (1988) Powder Diffraction File: Alphabetical Index, Inorganic Phases, JCPDS–International Centre for Diffraction Data, Swarthmore, PA., Au: Card No. 4–0784.
9. P. D. Townsend, P. J. Chandler, L. Zhang L (2006) Optical Effects of Ion Implantation, 3rd ed., Cambridge Univ. Press, Cambridge.
10. B. Y. Tsaur, J. W. Mayer, Metastable Au–Si alloy formation induced by ion–beam interface mixing, Philos. Mag. A **43**(1981) 345–361.
11. B.Satpati, P. V. Satyam, T. Som, and B. N. Dev, Nanoscale ion–beam mixing in Au–Si and Ag–Si eutectic system, Appl. Phys. A **79**(2004) 447–451.
12. X. Hu, D. G. Cahill, and R. S. Averback, Burrowing of Pt Nanoparticles into SiO_2 during Ion–beam Irradiation, J. Appl. Phys. **92**(2002) 3995–4000.
13. A. Klimmer, P. Ziemann, J. Biskupek, U. Kaise, and M. Flesch, Size–dependent effect of ion bombardment on Au nanoparticles on top of various substrates: Thermodynamically dominated capillary forces versus sputtering, Phys. Rev. B **79**(2009) 155427.
14. Y. Takeda, O. A. Plaksin, H. Wang, K. Kono, N. Umeda, and N. Kishimoto, Surface plasmon resonance of Au nanoparticles fabricated by negative ion implantation and grid structure toward plasmonic applications, Optical Review **13**(2006) 231–234.

15. P. K. Jain, K. S, Lee, I. H. EI-Sayed, and M. A. EI-Sayed, Calculated absorption and scattering properties of gold nanoparticles of different size, shape, and composition: applications in biological imaging and biomedicine. J. Phys. Chem. B **110**(2006) 7238–7248.
16. M. Ghaly and R. S. Averback, Effect of Viscous Flow on ion Damage near Solid Surfaces, Phys. Rev. Lett., **72**(1994) 364–367.
17. R. C. Birtcher and S. E. Donnelly, Plastic Flow Induced by Single Ion Impacts on Gold, Phys. Rev. Lett., **77**(1996) 4374–4377.
18. B. K. Russell, J. G. Mantovani, V. E. Anderson, R. J. Warmack, and T. L. Ferrell, Experimental test of the Mie theory for microlithographically produced silver spheres, Phys. Rev. B **35**(1984) 2151–2154.
19. M. Quinten, Optical Properties of Nanoparticle Systems: Mie and Beyond (Wiley–VCH, Weinheim, 2011).
20. P. Laven, Simulation of Rainbows, Coronas, and Glories by use of Mie Theory, Applied Optics, **42**(2003), 436–444.

Chapter 4

1. M. Hillenkamp, G. D. Domenicantonio, O. Eugster and C. Félix, Instability of Ag nanoparticles in SiO_2 at ambient conditions, Nanotechnology **18**(2007) 015702.
2. G. Valverde–Aguilar, J. A. García–Macedo, V. M. Rentería–Tapia, R. W. Gómez, M. Quintana–García, Modelling of optical absorption of silver NP's produced by UV radiation embedded in mesostructured silica films, J. Nanopart. Res. **13**(2011) 4613–4622.
3. N. Alissawi, V. Zaporojtchenko, T. Strunskus, I. Kocabas, V. S. K. Chakravadhanula, L. Kienle, D. Garbe–Schönberg, F. Faupel, Effect of gold alloying on stability of silver nanoparticles and control of silver ion release from vapor–deposited Ag–Au/polytetrafluoroethylene nano–composites, Gold Bull **46**(2013) 3–11.
4. S. Besner and M. Meunier, Femtosecond Laser Synthesis of AuAg Nanoalloys: Photoinduced Oxidation and Ions Release, J. Phys. Chem. C **114**(2010) 10403–10409.
5. J. F. Ziegler, J. P. Biersack, and U. Littmark, *SRIM - The Stopping and Range of Ions in Solids* (Pergamon Press, New York, 1985 (new edition in 2009)).
6. C. D. Marshall, J.A. Speth, and S. A. Payne, Induced optical absorption in gamma, neutron and ultraviolet irradiated fused quartz and silica, Journal of Non–Crystalline Solids **212**(1997) 59–73.
7. Y. Kojima and T. Kato, Nanoparticle formation in Au thin films by electron–beam–induced dewetting, Nanotechnology **19**(2008) 255605.
8. C. V. Thompson, Solid–State Dewetting of Thin Films, Annu. Rev. Mater. Res. **42**(2012) 399–434.
9. L. Repetto, B. Š. Batič, G. Firpo, E. Piano, and U. Valbusa, Ion induced spinodal dewetting of thin solid films, Appl. Phys. Lett. **100**(2012) 223113.
10. X. Hu, D. G. Cahill, and R. S. Averback, Burrowing of Pt Nanoparticles into SiO_2 during Ion–beam Irradiation, J. Appl. Phys. **92**(2002) 3995–4000.
11. A. Klimmer, P. Ziemann, J. Biskupek, U. Kaiser, and M. Flesch, Size–dependent effect of ion bombardment on Au nanoparticles on top of various substrates: Thermodynamically dominated capillary forces versus sputtering, Phys. Rev. B **79**(2009) 155427.
12. D. Barreca, A. Gasparotto, C. Maragno, E. Tondello, and S. Gialanella, Structure and Optical Properties of Sillica–Supported Ag–Au nanoparticles, Journal of nanoscience and nanotechnology **7**(2007) 2480–2486.
13. R. Kuladeep, L. Jyothi, K. Shadak Alee, K. L. N. Deepak, and D. Narayana Rao, Laser–assisted synthesis of Au–Ag alloy nanoparticles with tunable surface plasmon resonance frequency, Optical Materials Express **2**(2012) 161–172.

14. M. A. Garcia, Surface plasmons in metallic nanoparticles: fundamentals and applicaitions, J. Phys. D: Appl. Phys. **44**(2011) 283001.
15. M. Quinten, Optical Properties of Nanoparticle Systems: Mie and Beyond (Wiley–VCH, Weinheim, 2011).
16. K. M. Mayer and J. H. Hafner, Localized Surface Plasmon Resonance Sensors, Chem. Rev., **111**(2011) 3828–3857.
17. G. Pellegrini, V. Bello, G. Mattei, and P. Mazzoldi, Local–field enhancement and plasmon tuning in bimetallic nanoplanets, Optics Express **15**(2007) 10097–10102.
18. B. T. Draine and P. J. Flatau, Discrete–dipole approximation for scattering calculations, J. Opt. Soc. Am. A **11**(1994) 1491–1499.
19. M. Futamata, Y. Maruyama, and M. Ishikawa, Local Electric Field and Scattering Cross Section of Ag Nanoparticles under Surface Plasmon Resonance by Finite Difference Time Domain Method, J. Phys. Chem. B **107**, 7607–7617 (2003).
20. S. Link, Z. L. Wang, and M. A. El–Sayed, Alloy Formation of Gold–Silver Nanoparticles and the Dependence of the Plasmon Absorption on Their Composition, J. Phys. Chem. B **103**(1999) 3529–3533.
21. V. I. Belotelov, G. Carotenuto, L. Nicolais, A. Longo, G. P. Pepe, P. Perlo, and A. K. Zvezdin, Online monitoring of alloyed bimetallic nanoparticle formation by optical spectroscopy, J. Appl. Phys. **99**(2006) 044304.
22. M. Quinten, Optical constants of gold and silver clusters in the spectral range between 1.5 eV and 4.5 eV, Z. Phys. B **101**(1996) 211–217.
23. H. Sun, M. Yu, G. Wang, X. Sun, and J. Lian, Temperature–dependent Morphology Evolution and surface plasmon absorption of ultrathin gold island films, J. Phys. Chem. C, **116**(2012) 9000–9008.
24. W. Chen, K. P. Chen, M. D. Thoreson, A. V. Kildishev, and V. M. Shalaev, Ultrathin, ultrasmooth, and low–loss silver films via wetting and annealing, Appl. Phys. Lett. **97**(2010) 211107.
25. K. L. Kelly, E. Coronado, L. L. Zhao, and G. C. Schatz, The Optical Properties of Metal Nanoparticles: The Influence of Size, Shape, and Dielectric Environment, J. Phys. Chem. B **107**(2003) 668–677.
26. G. H. Chan, J. Zhao, G. C. Schatz, and R. P. Van Duyne, Localized Surface Plasmon Resonance Spectroscopy of Triangular Aluminum Nanoparticles, J. Phys. Chem. C **112**(2008) 13958–13963.
27. G. Mattei, V. Bello, P. Mazzoldi, G. Pellegrini, C. Sada, C. Maurizio, and G. Battaglin, Modification of composition and structure of bimetallic nanocluster in silica by ion beam irradiation, Nucl. Instrum. Methods Phys. Res., Sect. B **240**(2005) 128–132.

28. Yu–lin Xu, Appl. Opt. Electromagnetic scattering by an aggregate of spheres: far field, **36**(1997) 9496–9508.
29. Yu–lin Xu, Bo A .S. Gustafson, A generalized multiparticle Mie-solution: further experimental verification, Journal of Quantitative Spectroscopy and Radiative Transfer **70**(2001) 395–419.
30. L. M. Liz–Marzan, Tailoring surface plasmons through the morphology and assembly of metal nanoparticles, Langmuir, **22**(2006) 32–41.

Chapter 5

1. J. F. Ziegler, J. P. Biersack and U. Littmark, The Stopping and Range of Ions in Solids, Vol.1, (Pergamon, New York, 1985 (new edition in 1996)).
2. K. Neubeck, C. –E. Lefaucheur, H. Hahn, A. G. Balogh, H. Baumann, K. Bethge, and D. M. Rück, Ion beam mixing and radiation enhanced diffusion in metal/ceramic interfaces, Nucl. Instrum. Methods Phys. Res., Sect. B **106**(1995) 589–596.
3. X. Hu, D. G. Cahill, and R. S. Averback, Dewetting and nanopattern formation of thin Pt films on SiO_2 induced by ion beam irradiation, J. Appl. Phys. **89**(2001) 7777–7783.
4. J. Prakash, A. Tripathi, V. Rigato, J. C. Pivin, J, Tripathi, K. H. Chae, S. Gautam, P. Kumar, K. Asokan, and D. K. Avasthi, Synthesis of Au nanoparticles at the surface and embedded in carbonaceous matrix by 150 keV Ar ion irradiation, J. Phys. D: Appl. Phys. **44**(2011) 125302.
5. L. Repetto, B. Š. Batič, G. Firpo, E. Piano, U. Valbusa, Ion induced spinodal dewetting of thin solid films, Appl. Phys. Lett. **100**(2012) 223113.
6. X. Meng, T. Shibayama, R. Yu, S. Takayanagi and S. Watanabe, Microstructure analysis of ion beam–induced surface nanostructuring of thin Au film deposited on SiO_2 glass, J. Mater. Sci., **48**(2013) 920–928.
7. A. Klimmer, P. Ziemann, J. Biskupek, U. Kaiser, and M. Flesch, Size–dependent effect of ion bombardment on Au nanoparticles on top of various substrates: Thermodynamically dominated capillary forces versus sputtering, Phys. Rev. B **79**(2009) 155427.
8. D. Barreca, A. Gasparotto, C. Maragno, E. Tondello, and S. Gialanella, Structure and Optical Properties of Sillica–Supported Ag–Au nanoparticles, Journal of nanoscience and nanotechnology **7**(2007) 2480–2486.
9. L. Xu, L. S. Tan, and M. H. Hong, Tuning of localized surface plasmon resonance of well-ordered Ag/Au bimetallic nanodot arrays by laser interference lithography and thermal annealing, Applied optics **50**(2011) G74–G79.
10. M. Quinten, Optical Properties of Nanoparticle Systems: Mie and Beyond (Wiley–VCH, Weinheim, 2011), p.127–132.
11. J. Zhu, Theoretical study of the optical absorption properties of Au-Ag bimetallic nanospheres, Physica E **27**(2005) 296–301.

Appendix：

A.1 Liquid Film Dewetting

Capillary Energies

Dewetting is a process induced by the caplillary force. It is most often observed in a liquid film because of low viscocity. Dewetting occurs when a non-wetting film is not in equilibrium with the substrate. Consider a liquid droplet on the surface of a non-deformation substrate. The liquid drop has to employ a specific shape when is it thermodynamically stable. The contact angle θ, which is the angle between the tangent line of the liquid front and the substrate (Fig.A1.1), has to satisfy the Young's equition:

$$\gamma_s = \gamma_i + \gamma_f \cos\theta, \tag{A1.1}$$

where γ_f is the surface energy of the droplet, γ_s is the surface energy of the substrate, and γ_i is the energy of the droplet-substrate interface. At the equilibrium contact angle θ, the forces at the contact line (the line where the vapor, the liquid and the substrate meet) are balanced. If the contact angle is zero, the liquid droplet spread out and form a film on the substrate, this is the liquid wets the substrate.

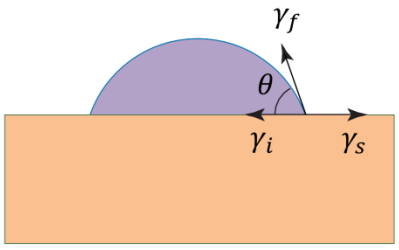

Fig. A1.1: The equilibrium shape of an island with an isotropic surface energy on a rigid substrate is that of a spherical cap with contact angle θ. (Adapted from Ref. A1)

If $\gamma_s > \gamma_i + \gamma_f$, a film is stable and will not dewet. On the other hand, when $0<\theta<180^0$, the wetting is partial. The non-wetting liquid droplet on the substrate must have the shape of a spherical cap (if no other forces exist in it) in order to achive a uniform pressure inside the liquid. The existence of external force field modifies the shape of the liquid droplet. Generally, gravity acting on the droplet, which becames unneglectable when the size is large, tends to flatten the top of the liquid surface.

When a liquid droplet on a substrate is not in equilibrium, the liquid front will either spread (wetting) or recede in order to reach the equilibrium state. The latter process is called dewetting. Also, this happens for a continous non-wetting liquid film on the substrate other than a droplet. The dewetting starts with the nucleation of the dry patches (holes of the continous film). The dry patches then start growing, until the neighbored dry patches meet each other.

A.2 Rayleigh Instability

The zero dimensional liquid droplet and two dimensional non-wetting liquid films were discussed in the above when they are not in equilibrium with the substrates. For one dimensional non-wetting liquid lines, a special phenomenon called Rayleigh instability occurs.

Rayleigh instability is a phenomenon that is observed in continuous one dimensional liquid, such as a waterfall. It is also a capillary force induced process. In this process, the continuous liquid line breaks and becomes a series of droplets. It can only happen when the liquid line is longer than a critical length so that it is unstable. The small perturbations such as those from blowing air will grow spontaneously. A wavelike structure will develop along the liquid line and its wavelength determines the spacing between the droplets thatare eventually formed (Ref. [A2, A3]). For the case of a free standing liquid line, the mechanism is also adoptable (Fig. A2.1 a-d).

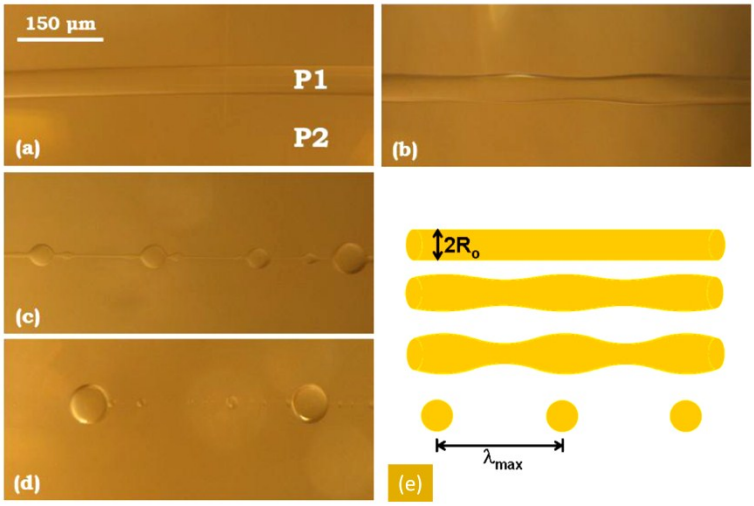

Fig. A2.1: Pleteau Rayleigh Instability induced in an all-polymer fiber: core (P1) is cyclic olefin copolymer (COC) and the cladding (P2) is polycarbonate (PC). Panels (a) to (d) correspond to

progression in time while the fiber is heated. (a) The initially intactcore. (b) Spontaneous initiation of well-defined sinusoidal modulation at the interface between the core and cladding. (c) Deeper modulation and droplet formation. (d) Droplet pinch off and satellite formation. (Adapted from Ref. A2) (e) A schematic view of a cylingrical free standing liquid line under the Pleteau Rayleigh Instability (Ref. [A3]).

Rayleigh found out that a cylingrical free standing liquid line the random perturbation could only grow if their wavelength λ_{min} satisfies the following condition:

$$\lambda_{min} \geq 2\pi r, \tag{A3.1}$$

where r is the radius of the liquid line (Fig. A2.1e). This critical wavelength determines the minimum length of a liquid line to show Rayleigh instability.

A.3 Dewetting of Thin Metal Films on Dielectric Substrate

Dewetting is a process induced by the caplillary force. It is most often observed in a liquid film because of low viscocity. The physics of liquid dewetting is summarized here and many of the same knowledge can be applied to the dewetting of solid films. Dewetting occurs when a non-wetting film is not in equilibrium with the substrate. Dewetting of solid films generally progresses through at least three distinct stages: hole formation, hole growth and impingement, and ligament breakup (Ref. A1).

Hole Formation

Solid cylinders are inherently unstable, and a range of perturbations will lead to sphere formation through a process in which the free energy continuously decreases. Although cylinders are unstable, planar surfaces with isotropic surface energies are stable with respect to all perturbations. As a consequence, an infinite defect−free zero−stress film with isotropic surface energies is stable with respect to perturbations with amplitudes less than the film thickness. This is true even if the equilibrium shape of the film is an island. Such a film is in a metastable shape. Given that flat surfaces, as described above, are stable with respect to small perturbations, a process that leads to hole formation in a film is a necessary precursor to dewetting.

Effects of grain structures of polycrystalline films

In polycrystalline films, grain boundaries and grain boundary triple junctions can play important roles in hole formation. In Figure A3.1, the idealized 2D grain structure schematically illustrated. In this 2D model, the film has no depth into the page. An equivalent 3D model would be one in which the grains are sections of cylinders that

meet at grain boundaries with neighboring grains. The grain boundaries have energies γ_{gb}, and the grain size is defined as D=2R. For isotropic γ_f, a force balance at the point at which the grain boundary and surface meet will lead to the shape illustrated in Figure A3.1. When this condition is satisfied, a groove forms at the boundary, with a depth δ below the original planar film surface.

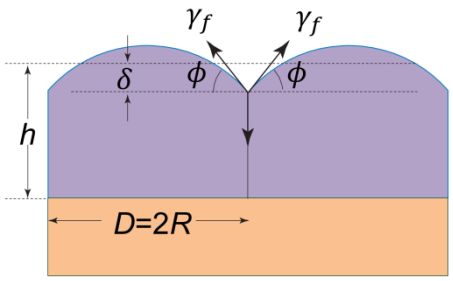

Fig. A3.1: Schematic cross-sectional view of a 2D polycrystalline film with in-plane grain diameter D and radius R on a rigid substrate. In its equilibrium shape, the film's surface will develop grooves with root angles ϕ given by the energies of the surfaces that meet at a grain boundary (here taken to be γ_f for both grains) and the energy of the grain boundary γ_{gb}. The equilibrium depth of the groove δ, can be characterized relative to the position the surface would have if it were flat. In the case shown here, the groove depths are less than the film thickness so that holes in the film do not form. (Adapted from Ref. A1)

If δ is greater than the film thickness h, the groove will contact the substrate and will be subject to growth as a hole to initiate dewetting. In the 2D case, this hole will always grow. Given that grain boundaries have varying energies, in any given case not all grain boundaries will form holes. Hole formation will be most likely at high-energy grain boundaries. The number of holes will also increase when h and γ_f are small and γ_{gb} and R are large.

The case of dewetting of 3D films was also treated. It is showed that the depth of holes

at grain boundary triple junctions will generally be greater than the depth of grooves at the boundaries between two grains. Grain boundary triple junctions are defined by the points at which three grain boundaries meet each other and the film's surface. A deep groove of roughly conical shape forms at a triple junction. Given that grooves would be deepest at triple junctions, it is said that triple junctions would provide the locations at which holes would be most likely to form first.

Hole Growth

Once a hole of critical size has formed, capillary energies will drive retraction of its edge and the hole will grow. The rate of hole growth is therefore governed by the rate at which the edge retracts and on how the shape of the edge evolves.

Edge retraction

If we consider a hole edge with a sharp corner, as schematically illustrated by the dashed line in Fig. A3.2, material will be transported from the corner to reduce its curvature. However, the curvature of the edge of the film will always be higher than that of the flat surface of the film surrounding the hole. There will therefore be a continuing net flux of material from the triple line (at which the film, ambient, and substrate meet), over the rim of the hole, and out into the flat area surrounding the hole. This flux leads to retraction of the edge and to corresponding hole growth. The mass transport occurring during hole growth can, in principle, occur through *surface self-diffusion* of the film material.

As the edge of the hole retracts, material accumulates to form an elevated rim with a height greater than the surrounding film thickness, as shown in Fig. A3.2. The flux from

the triple line and over the rim is driven by the high local curvature relative to the low curvature of the surrounding film surface. However, the flux away from the rim is driven by a reducing curvature so that a flux divergence occurs and mass accumulates at the edge to form a rim. The rim height increases as the edge continues to retract. As a consequence, the curvature at the edge is reduced, the driving force for mass transport is reduced, and the edge retraction rate is reduced.

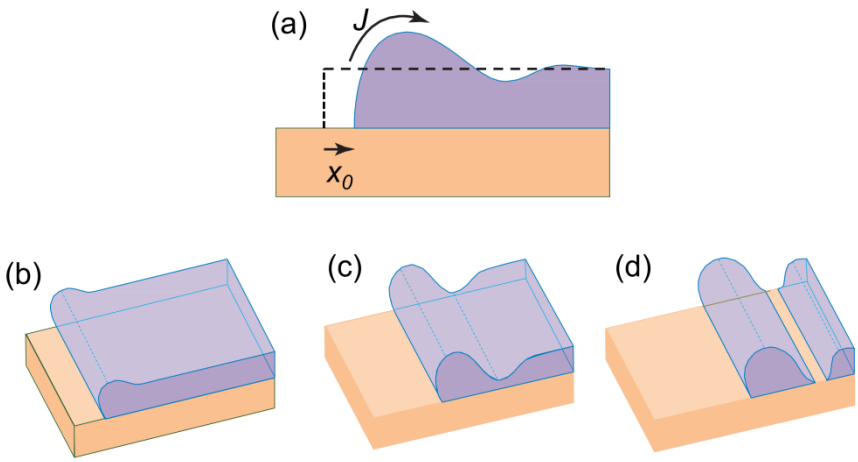

Fig. A3.2: (a) Cross-sectional view of a retracting edge of a film, after retraction over a distance x_0 from the position of the initial edge with a sharp corner. Retraction proceeds by surface self-diffusion with a flux *J* from the triple line to the flat area ahead of the edge. Mass accumulation at the edge of the film leads to the development of a rim, and a flux divergence ahead of the rim causes the formation of a valley. (b–d) As an edge retracts, the rim thickens, and the valley ahead of the rim deepens. In some cases the valley makes contact with the substrate, leading to the creation of two new triple lines and a wire or strand formed from the now-isolated rim. The new edge continues to retract. This process, called pinch-off, can repeat. (Adapted from Ref. A1)

Rim pinch-off

It is noted that an oscillation in the film's thickness develops ahead of the rim and that the amplitude of this oscillation rapidly diminishes with distance from the rim. The primary consequence of formation of the oscillation is that a relatively deep valley forms immediately ahead of the rim. Also, the depth of this valley increases as the edge retracts, until it contacts the substrate surface. This leads to pinch-off of the rim to form an island (or a wire in three dimensions) (Fig. A3.2c and d). The new edge then continues to retract and develop a new rim, and the process repeats. The overall retraction rate therefore varies cyclically as this repeated pinch-off occurs. Srolovitz & Safran analyzed the initial rate of edge displacement prior to pinch-off and concluded that the approximate scaling relationship for the edge retraction.

Although the exact functional dependencies described above vary, all these analyses indicate that the rate of hole growth, and therefore the rate of dewetting, should increase with decreasing h and increasing D_s, and therefore with increasing T. In addition, in all cases the cross-sectional area of the wire left behind after pinch-off scales with the film thickness.

Late stages of dewetting

As discussed above, hole growth leads to the development of rims that can break down into wire-like strands through pinch-off (Figures A3.2). In both cases, these strands have radii, r_{strand}, that scale with the film thickness. Strands are subject to the Rayleigh-Plateau-like instability. Free standing cylinders of radius r_R are unstable with respect to radial perturbations of wavelength greater than $2\pi r_R$ and tend to break up into spheres at spacings of $2\sqrt{2}\pi r_R$. The radii of the resulting particles scale with r_R.

Strands of solids that partially wet a substrate do not directly obey the Rayleigh-Plateau

analysis for cylinders. Both surface energy anisotropy and the presence of a contact line contribute to differences in the analysis. However, the particle size that results from the instability of polycrystalline strands is still expected to scale with the square root of the cross-sectional are, and the final island size should scale as $r_{island} \propto r_{strand}$. Grain boundary grooving can also contribute to the break-up or to the stability of strands.

References for Appendix:

A1. C. V. Thompson, Solid–State Dewetting of Thin Films, Annu. Rev. Mater. Res. **42**(2012) 399–434.

A2. J. J. Kaufman, G. Tao, S. Shabahang, E. -H. Banaei, D. S. Deng, X. Liang, S. G. Johnson, Y.Fink, and A. F. Abouraddy, Structured spheres generated by an in-fibre fluid instability, Nature, **487**(2012) 463–467.

A3. S Karim, M E Toimil-Molares, A G Balogh, W Ensinger, T W Cornelius, E U Khan and R Neumann, Morphological evolution of Au nanowires controlled by Rayleigh instability, Nanotechnology **17**(2006) 5954–5959.